

Optimizing Design of 2D Sub-wavelength Gratings for Antireflection Coatings of Multi-junction III-V Concentrator Cells

A Thesis Presented to
the Faculty of the Department of Physics
University of Houston

In Partial Fulfillment
of the Requirements for the Degree
Master of Science

By
Wei Wang
December 2012

**Optimizing Design of 2D Sub-wavelength Grating for
Antireflection Coating of Multi-junction III-V
Concentrator Cells**

APPROVED:

Wei Wang

Prof. Alex Freundlich, Chairman

Prof. Kwong Lau

Prof. Paul Ruchhoeft

Prof. Lowell Wood

Dean, College of Nature Science and Mathematics

Acknowledgments

I wish to thank all those who helped me. Without them, I could not have completed this project. I have to thank all the members in our group. Thanks to my supervisor Alex Freundlich for his wise and broad view guide; who not only served as my supervisor but also encouraged and challenged me throughout my academic program. Thanks to Akhil Mehrotra for patient explanation and detailed instruction; who urged me to speed up my progress. Thanks to Andenet Alemu for checking my beginning calculation results with his. Thanks to Gopi Krishna V for his glowing example of independent thinking and solving problems. Thanks to Manori Gunasekera for a shining model to set a neat lab and her sister-like regard. Thanks to Camden Kirkland for nice reviews of my papers. Thanks to Rabi Ebrahim for systematic technology for equipment. Last but most important, I thank all my committee members, who spent much effort in reading my manuscript and giving me valuable suggestions.

**Optimizing Design of 2D Sub-wavelength Gratings for
Antireflection Coatings of Multi-junction III-V
Concentrator Cells**

An Abstract of Thesis
Presented to
the Faculty of the Department of Physics
University of Houston

In Partial Fulfillment
of the Requirements for the Degree
Master of Science

By
Wei Wang
December 2012

Abstract

In III-V concentrator applications sunlight is focused onto the surface of cell and consequently light arrives with a wide angular distribution that limits the effectiveness of conventional thin-film antireflective coatings (ARC). Furthermore, the transmission properties are generally degraded non-uniformly over the electromagnetic spectrum, which in the case of multi-junction solar cells, leads to additional subcell current matching-related losses. Here, and in an attempt to identify a better alternative to the conventional dual layer ARCs, we have undertaken a systematic analysis of design parameters and angular dependent antireflective properties of dielectric grating formed through the implementation of sub-wavelength arrays of 2D pyramidal and hemispherical textures. The study includes evaluation of these properties for several common dielectrics *i.e.* SiO₂, Si₃N₄, SiC, TiO₂, and ZnS, through a careful selection of dielectric material and design. These structures can significantly surpass the performance of planar double-layer ARCs (*i.e.* MgF₂/ZnS), and the total number of reflected photons over 380-2000 nm wavelength range can be reduced to less than 2%, by use of single material textured dielectric. It is also shown that the implementation of these structures for a typical concentrated 3 or 4 junction solar cell with acceptance angles ranging from 0-60 degrees, reduces total losses of reflected photons for each subcell to less than 4%, hence reduces current degradation.

Contents

Acknowledgments.....	iii
Abstract.....	v
Contents.....	vi
List of figures and tables.....	viii
Glossary.....	xii
Chapter 1 Introduction.....	1
Chapter 2 Introduction to the Physics of Simulation Solar Cells.....	4
2.1 Sunlight Spectrum Properties.....	5
2.1.1 Sun spectrum in space outside earth atmosphere.....	6
2.1.2 Black body approximation of sunlight spectrum.....	8
2.1.3 Sunlight and atmosphere effect.....	10
2.1.4 Air Mass.....	12
2.2 Principle of Solar Cell Operation.....	14
2.3 Ideal Solar Cell Efficiency Limit for Solar Cells.....	15
2.3.1 Detailed balance energy limit.....	16
2.3.2 Theoretical efficiency limit for tandem and multi-junction solar cell.....	22
2.4 Practical Devices with Finite Absorption Coefficient.....	27
2.4.1 Absorption coefficient.....	29
2.4.2 Drift diffusion model.....	31
2.4.3 Design limitations for crystalline III-V multi-junctions: description of a few solar cell designs.....	33
2.5 Minimizing Front Surface Reflection Losses in Solar Cells.....	35
2.5.1 Single-layer ARC.....	36
2.5.2 Double-layer ARC—most widely used.....	37
2.5.3 Current matching in multi-junction solar cells.....	39
Chapter 3 Antireflective Coating (ARC).....	41
3.1 Traditional Single / Multi-layer Planar ARCs.....	42
3.1.1 Optical design of multi-layers – choice of refractive indices.....	42
3.1.2 Optical design of multi-layers – thickness optimization.....	45
3.2 Experimental Approaches for Planar ARC.....	48
3.3 Experimental Approaches to Textured Surface.....	49
3.3.1 Si anisotropic etching.....	53
3.3.2 RIE moth eye on Si substrate.....	54
3.4 State-of-the-Art.....	55
3.5 Classical Light Propagation in Thin Film with Finite Dimensionality.....	57
3.5.1 Light propagation at the boundary from Fresnel Equation.....	60
3.5.2 Light propagation in the medium expressed in matrix form.....	61
3.5.3 Diffraction and reflection explanation from rigorous coupled-wave analysis (RCWA).....	65
3.5.4 Pros and cons for traditional methods.....	65
3.6 Application of Transfer Matrix Method for Multi-layer ARC and Comparison with Experimental Data.....	69

3.7 Conclusion	74
Chapter 4 Simulating Dielectric Material of Sub-wavelength Periodic Antireflection Texture	76
4.1 1D Binary with Rectangular Cross Section	78
4.2 1D Binary with Triangular Cross Section	83
4.3 2D Hemisphere Grating	88
4.4 2D Pyramid Grating	92
4.5 2D Pyramid Texture for Multi-junction Cells	96
Conclusion	99
Chapter 5 Results and Conclusion	100
Appendix A: Equations in Drift Diffusion Model	105
Appendix B: Solar Cell Techniques to Appease Lattice Mismatch	107
B.1 Buffer layer between subcells	107
B.2 Inverted metamorphic multi-junction (IMM)	108
Appendix C: Fresnel Equation Derivation	109
C.1 S mode	112
C.2 P mode	112
Appendix D: Transfer Matrix Method Derivation	114
D.1 Light propagation in a homogeneous dielectric film	119
D.2 The reflectivity and transmission coefficients from transfer matrix method	120
Appendix E: An Example of RCWA Application Structure	123
Appendix F: Recipe of Textured Surface	130
F.1 Sputter deposition	130
F.2 Si KOH wet etching	131
Appendix G: Solar Cell Patterning	132
G.1 Back etching	132
Indium mounted samples	132
Non Indium mounted samples	132
G.2 Degreasing	133
Front contact patterning by photolithography	134
Gold Evaporation	136
Gold Electroplating	140
G.3 Contact layer etching	141
G.4 Mesa Etching	141
Reference	143

List of figures and tables

Figures

Fig 2.1.1 Schematic of sun-earth rotation and variation of declination angle	7
Fig 2.1.2 Schematic of variable angles effect power density and light path	7
Fig 2.1.3 Variation of light intensity based on black body radiation with respect to wavelength and temperature	9
Fig 2.1.4 Atmospheric effects of light passing through the atmosphere	11
Fig 2.1.5 Definition of air mass	12
Fig 2.1.6 Comparison of black body radiation, AM0, AM 1.5G, and AM 1.5D	13
Fig 2.2.1 Schematic of solar cell operating principle	15
Fig 2.3.1 Physical parameters relevant to single-junction efficiency limit	17
Fig 2.3.2 Converted, transmitted, thermalized, and emitted photon efficiency as function of bandgap	19
Fig 2.3.3 I-V characteristic of single-junction solar cell with bandgap $E_g = 1.35$ eV	20
Fig 2.3.4 Ideal single-junction efficiency versus bandgap under AM 1.5G for different sun concentration	21
Fig 2.3.5 Schematic of tandem solar cell showing different parameters used	23
Fig 2.3.6 Bandgap optimization and efficiency calculation of tandem under AM 1.5G spectrum with 1 sun and 500 sun concentration	24
Fig 2.3.7 An example of LM multi-junction device operated under concentrator and an example of concentrated photovoltaic (CPV) system	26
Fig 2.4.1 Comparison of confirmed practical solar cell efficiency with theoretical efficiency. Experimental data extracted from solar cell efficiency tables (version 40)	28
Fig 2.4.2 Absorption coefficient of commonly used semiconductor materials	29
Fig 2.4.3 Bandgap energy and lattice constant of various III-V semiconductors at room temperature	33
Fig 2.5.1 Reflectivity of Si and AlGaAs bare substrates under normal light	36
Fig 2.5.2 Integrated photon loss of single-layer SiN thickness dependence on crystal Si	

(100) substrate under normal light over the spectrum 380~1200 nm	37
Fig 2.5.3 Reflectivity of AlGaAs substrate with/without ARC under normal light and with double-layer ARC for off-normal light	38
Fig 2.5.4 Number of photon-loss for optimized ZnS pyramid grating (colors indicate photon loss in different subcells)	39
Fig 3.1.1 Reflection coefficient (<i>i.e.</i> percentage of light reflected), angle- and wavelength-averaged, as a function of the number of layers for optimized ARCs on silicon solar cells	46
Fig 3.3.1 SEM of crystalline Si (100) anisotropic etching in KOH (a) side view, (b) zoom in structure	50
Fig 3.3.2 (b) Tilted (20°) SEM image showing templating silica array and underneath silicon nipples etched by SF ₆ RIE for 9 min. (d) Silicon nipples after 9 min HF etch. (ref [67] by C.H. Sun <i>et al.</i>)	50
Fig 3.3.3 Al(Ga)InP sub-wavelength structure profile etched through the optimized recipe, but different time (a) t = 3 min; (b) t = 5 min. (ref [1] by R. Y. Zhang <i>et al.</i>)	51
Fig 3.3.4 (b) cross-sectional SEM images of the syringe-like ZnO NRAs. (c)The high-magnification image showing the ultrasmall tips on the ZnO NRAs. (ref [2] by L.K. Yeh <i>et al.</i>)	51
Fig 3.4.1 The measured and simulated reflection spectra comparison for Al(Ga)InP SWS as shown in Fig. 3.3.3(b); (a) incident angle is 8°, (b) incident angle is 45°.	55
Fig 3.5.1 Notification of angles	59
Fig 3.6.1 (a) Dispersion relation of MgF ₂ , (b) Dispersion relation of MgF ₂ refractive index versus wavelength	69
Fig 3.6.2 Dispersion relation of C-Silicon (100), refractive index (both the real part and imagine part) versus wavelength	70
Fig 3.6.3 Normal incident light, where MgF ₂ -ZnS are coated on C-Si (100) substrate, using Black body radiation at 5800 K. (a) at a larger thickness scale (20 nm to 1000 nm), (b) at a smaller thickness scale (20 nm to 200 nm)	71
Fig 3.6.4 Angular dependence of incident angle for MgF ₂ -ZnS double-layer on c-Si(100) at AM 1 optimized thickness [100 nm, 54 nm]	72
Fig 3.6.5 Calculated reflectivity of optimized MgF ₂ (115 nm) ZnS (66 nm) dual AR on GaAs for spectrum 300 nm ~1500 nm for various incidence angles	73
Fig 3.6.6 Measured (solid line) and simulated (dash line) reflectance spectra of GaAs substrate with MgF ₂ -ZnS double-layer	73

Fig 4.1 An example of textured surface that refractive index varies from air to antireflection material	77
Fig 4.2 Schematic of light propagation among a stack of thin homogeneous films	77
Fig 4.3 Concentrated III-V solar cell structure with ARC, and conventional ARC's angular tolerance property (i) micro scale textured surface, (ii) sub-wavelength scale dielectric gratings, (iii) reflectivity of MgF ₂ -ZnS dual AR	78
Fig 4.1.1 Binary rectangular-groove grating used for ARC with parameter notation	79
Fig 4.1.2 the reflection coefficient versus thickness comparison for double and single layer	80
Fig 4.1.3 Variation of reflectivity with various optimized parameters for ZnS binary grating structure.	82
Fig 4.2.1 Schematic of 1D grating with triangular cross section	84
Fig 4.2.2 The reflectivity of 1D grating with triangle cross section versus the height of ridge	85
Fig 4.2.3 The angular and wavelength dependence for reflectivity at H = 6000 nm	86
Fig 4.2.4 The reflection of 1D grating with triangle cross section	87
Fig 4.3.1 Structure and parameter notation for 2D hemisphere grating	88
Fig 4.3.2 Reflectivity simulation of hemisphere grating from the literature: (a) loose-packed structure, (b) close-packed structure	90
Fig 4.3.3 Angular dependent photon losses for 2D hemisphere grating made with various materials for an AM1.5G incident spectrum over the 0.38-2 micron range	91
Fig 4.4.1 Reflectivity simulation of pyramid grating from the literature: (a) loose-packed structure, (b) close-packed structure	93
Fig 4.4.2 Structure of 2D pyramid grating with parameter notation	94
Fig 4.4.3 Optimization of ZnS 2D pyramid grating from 380 nm to 2000 nm (incident AM1.5G)	95
Fig 4.4.4 Photon loss comparison for proposed structures with conventional double-layer ARC	96
Fig 4.5.1 AR grating causing photon loss in each junction for a GaInP/GaAs/Ge multi-junction solar cell under AM1.5G illumination	97
Fig 4.5.2 Notations of concentrator's light cone	97

Fig 4.5.3 Comparison of current loss as a function of angle of focusing cone for various multi-junction devices between duo layer (crayon) and 2D pyramid grating (solid color) on multi-junction devices	98
Fig B.1 Buffer layer	107
Fig B.2 Cell fabrication by inverted layers transfer process.....	108
Fig C.1 Explanation of S mode and P mode (a) S mode, (b) P mode	111
Fig E.1 Geometry for planar-grating diffraction	123
Fig E.2 Geometry for binary rectangular-groove grating	127
Fig F.1 Schematic of sputtering deposition technique.....	130
Fig G.1 Pouring level for beakers in degreasing process.....	134
Fig G.2 Schematic diagram of evaporation system	137
Fig G.3 Cross section of photoresist after patterning	138
Fig G.4 The theory of electroplating.....	141
Fig G.5 The view of samples after mesa etching.....	142

Tables

Table 2.3.1 Optimized bandgap and efficiency limit for single/double/triple junction under various concentration factors	25
Table 3.1.1 Refractive indices of optional AR materials, characters o and e in bracket refer to ordinary and extraordinary wave respectively	43
Table 3.1.2 Optimal refractive indices and corresponding materials for ARCs with 1-6 layers on MJ solar cells with AlInP in air	44
Table 3.1.3 Bandgaps of commonly used AR materials	44
Table 3.1.4 Thickness optimization of 1-4 layers AR design on AlInP substrate over 300-1800 nm under AM 1.5D spectrum {references [32]}	45
Table 3.1.5 Three sets of double-layer designs for AlInP and Si substrate solar cells with solar cell working spectrum 300 nm-1800 nm and 400 nm-1200 nm respectively	47
Table 4.3.1 2D hemisphere textured surface reflectivity versus wavelength	89
Table 4.4.1 2D pyramid textured surface reflectivity versus wavelength with angular dependence.....	92

Glossary

In this thesis, there are some terms that need to be defined, in case in other references or papers they have different meanings.

Absorber – it refers to materials with certain bandgaps that have photovoltaic property to absorb photons above their bandgaps, and converts them into electron-hole pairs. In solar cell devices, it's usually a p-n junction, which provides a driving force to separate electrons and holes to the two sides of junction individually.

ARC – antireflection coating.

Concentration (factor/coefficient) – due to the application of concentrator on solar cell devices, the intensity of sun light arriving at devices is amplified. The value of amplified sunlight intensity over direct sunlight intensity is the concentration (coefficient). *e.g.* if the value is 500, the concentrated light is also called as 500 sun.

Photon loss -- the percentage of number of photon loss due to surface reflection, usually refers to a value at single wavelength (different as reflectivity, which describes energy loss).

RCWA – rigorous couple wave analysis

Recombination – because of Coulomb force between electrons and holes, they will not exist forever. Hence they would meet and recombine, and this process is called recombination.

Reflection -- at the interface of two media, the property of light wave that is propagating backward into the first medium.

Reflectivity -- the energy ratio of reflected electric-magnetic field over incident electric-magnetic field at the boundary of two media; usually referring to a value at single wavelength and normal incident angle.

Integrated / total photon loss -- normalized the integrated photon loss over certain wavelength region on AM 1.5G spectrum. Mathematically, it equals to the integral over wavelength of photon loss multiplied by AM 1.5G intensity over the integral of AM 1.5G intensity over wavelength. This word is also used for concentrated solar cell devices, which has one more integral over incident angle from zero to concentrators' half open angle.

Integrated / total reflectivity -- normalized the integrated reflectivity over certain wavelength region on AM 1.5G spectrum. Mathematically, it equals to the integral over wavelength of reflectivity multiplied by AM 1.5G intensity over the integral of AM 1.5G intensity over wavelength.

Transmission – at the interface of two media, the property of light wave that is propagating forward into the second medium.

Thermalization loss – when photons' energy is larger than absorber's bandgap, electron-hole pairs can be generated. But due to lattice vibration, electrons would lose their energy and go to conduction band, and holes would go to valence band. The lost energy resulting from lattice vibration is thermalization loss.

Transparency loss -- when photons' energy is smaller than absorber's bandgap, they would generate any electron-hole pairs, passing through absorbers as if the absorber is transparent. So these photons' energy loss is transparency loss.

Chapter 1 Introduction

Most solar cells are made with absorber materials exhibiting high refraction indices compared to air ($n_{abs} \gg n_{air} = 1$). Consequently, in the absence of light coupling strategies, a large number of sunlight photons can be reflected by the front surface of devices. *e.g.* for a typical solar cell made of silicon absorber ($n_{abs} \sim 4$), nearly 36% of photons impinging the surface of the devices will be reflected. The conventional approach in overcoming such reflection losses is the incorporation of single or multiple layers of lower index materials. Hence, the goal of this work was to minimize energy/photon loss at interfaces between air and solar cells, for both single-junction and multi-junction photovoltaic devices. Photovoltaic devices' working process contains four main procedures, such as coupling light, absorbing photons, generating electron - hole pairs, and collecting current. This work was concentrated on the first procedure, light coupling. The more precise objective of this study was to evaluate antireflection (AR) texturing that presented both AR and angular tolerant (AT) properties for direct bandgap solar cell materials, especially III-V semiconductors. Multi-junction design surpasses the initial Si solar cell, due to use of wide spectrum, which ranges from 380 *nm* to 1800 *nm*. For a more general wide spectrum, the working region was extended to 2000 *nm*. Due to the series connection between subcells, multi-junction solar cells raise a current matching issue, requiring the maximum current loss among all the subcells to be minimized.

Among various material candidates and texturing, this study is going to figure out what morphology will perform best, with which material for specific operating solar cell designs, including both single-junction and multi-junction background.

Chapter 2 of this thesis describes the basis of sunlight spectrum properties and its black body approximation, whose distribution is significant for optimizing antireflection (AR) design, ideal efficiency limit (detailed balance energy limit) of solar cell, and practical factors to affect efficiency. Finally, it states the necessity of reducing front surface reflection loss, especially for cells under concentrators with large light cone open angle, and current-matching issues in multi-junction devices.

Chapter 3 gives a clear picture of why dual-layers, which are used as a reference for later AR grating characteristic, are widely applied in industry and lab for antireflection purpose, and experimentally what has been done in the recent work of antireflection texturing techniques. It also states that textured surface improves antireflection properties and angular tolerant desire. It consequently illustrates the rules of light propagation in thin films with finite dimensions. Also, it compared three simulation approaches, which are Fresnel Equations, thin film model based on transfer matrix method, and advanced RCWA (rigorous coupled wave analysis). The result is the thin film model fits this work best. Lastly, it validates that the thin film model agrees with experimental results on finite dimension ARC.

Chapter 4 gives details about simulation work strategies and results of various sub-wavelength textures. It demonstrates the characterization of several simplified geometric patterns abstracted from current fabrication techniques, like 1D and 2D texturing on single-junction cells. It concludes that 2D pyramid grating surpasses other morphologies in both antireflection and angular tolerant properties.

Chapter 5 concludes this thesis by summarizing all the work done and the results

obtained.

The appendix completes this thesis by showing drift diffusion modeling formulas, explaining two solar cell techniques to reduce lattice mismatch caused recombination, derivation of Fresnel Equation, transfer matrix method, and RCWA, textured surface recipe, and solar cell processing steps after growth.

Chapter 2 Introduction to the Physics of Simulation Solar Cells

A solar cell is a device that directly converts the energy from sunlight into electrical energy through the photovoltaic process. In its simplest form, the photovoltaic solar cell comprises an absorber material, which has a forbidden energy gap between the highest occupied electronic states (the valence band), and the conduction band of the material, referred to as the bandgap. The absorption of each sunlight photon with photon energy larger than the bandgap generates electron-hole (e-h) pairs. Photons with energy smaller than the bandgap do not participate in the carrier generation process and are lost by transparency. Naturally, in the absence of an external driving force photon-generated electrons in the conduction band can recombine with holes in the valence band, by emitting photons with energy equal to or smaller than the bandgap. Thus collecting carriers prior to these recombinations is an important parameter in the design of photovoltaic devices. The collection of the photon-generated electrons and hole into an external circuit establishes a current, at a different circuit potential whose amplitude is directly correlated to the absorber material's bandgap. For a solar cell made with a single bandgap absorber, there is a tradeoff on the selection of material bandgap. As devices made with larger bandgap absorbers in principle absorb smaller number of photons, hence deliver smaller current output yet at a higher voltage; whereas devices, made with a narrower bandgap absorbers, deliver higher currents at smaller voltages. While the selection of the absorber bandgap and efficient collection of photo-generated carriers are key to high performance devices, another important ingredient is the efficiency of light coupling. In particular, most solar cells are made with absorber materials exhibiting large refraction indices compared to air ($n_{abs} > n_{air} = 1$). Consequently, in the absence of light

coupling strategies, a large number of sunlight photons can be reflected by the front surface of the device. *i.e.* for a typical solar cell made with an absorber made of silicon ($n_{abs} \sim 4$), nearly 36% of photons impinging the surface of the devices will be reflected ($R = (n-1)^2 / (n+1)^2 \sim 9/25 \sim 0.36$). As stated in the introduction, the main objective of this work is to identify advanced strategies to minimize such losses in multi-junction devices made with monolithically integrated multiple absorber materials. In this chapter we will first discuss the properties of sunlight, the black body-like distribution of its spectral composition, and the effect of atmospheric attenuations. The sunlight spectral characteristics will be then used to establish within the framework of detail energy balance consideration the ideal efficiency limits for single and multi-bandgap solar cells^[3]. Then, within the framework of semiconductor p-n junction approach, we will discuss practical material and design consideration for modeling and fabrication of modern solar cell devices. The chapter will then discuss the common thin film antireflective approaches toward minimizing reflection losses in common single and multi-junction semiconductor solar cells, and their limitations for flat panel and concentrator applications. The discussion will stress the criticality of sunlight incident angular tolerance, and discuss the pros and cons of various existing light management strategies.

2.1 Sunlight Spectrum Properties

In this section we will show the notion of sun light spectrum, black body approximation to sun radiation, atmosphere effect to sunlight, air mass, etendue, declination, and zenith angle.

2.1.1 Sun spectrum in space outside earth atmosphere

Due to nuclear fusion reactions, which convert hydrogen into helium, the sun is a hot gas sphere with internal temperatures over 20 million degrees kelvin. The radiation from the inner core is not visible since it is strongly absorbed by a layer of hydrogen atoms closer to the sun's surface. Heat is transferred through this layer by convection. The surface of the sun, the photosphere, is at a temperature of about 6000 K and can be closely approximated as a black body. The 6000 K spectrum is commonly used for black body approximation, but $5762 \pm 50 \text{ K}^{[4]}$ and $5730 \pm 90 \text{ K}^{[5]}$ have also been proposed as a more accurate fit to the sun's spectrum.

The sun has been radiating energy at the rate of $3.9 * 10^{26} \text{ W}$ (watts) for billions of years. There is a parameter that describe the amount of sun light (energy) caught by earth, defined by the solid angle of view of sun from earth, named as “etendue” (This definition must be applied for infinitesimally small "elements" of area and solid angle, which fits sun-earth system, as the distance between sun and earth L is much larger than the radius of both sun R_{sun} and earth R_{earth}). In Shockley Queisser’s paper (*ref. [1]*), it is defined as $\pi * n^2 * R_{sun}^2 / (L - R_{earth})^2 \sim \pi * n^2 * R_{sun}^2 / L^2$, around $6.75 * 10^{-5}$, where n is the refractive index of transportation medium.

The power density reaching the earth’s atmosphere changes with the Sun-Earth distance as the Earth rotates in elliptical orbit around the sun, around 3.4% variation. The largest irradiance happens in January (with shortest sun-earth distance R_s) and smallest irradiance happens in July (with longest sun-earth distance R_l). The variation rule of power density throughout a year can be explained in equation (2.1.1), where N refers to

the day of the year, (i.e. $n = 1$ for January 1st), and $H_{const} = 1.353\text{kw/m}^2$, refers to the standard value, commonly referred to as air mass zero's power density, which will be explained more in section 2.1.4.

$$\frac{H}{H_{const}} = 1 + 0.033\cos\left(\frac{360(n-2)}{365}\right) \quad (2.1.1)$$

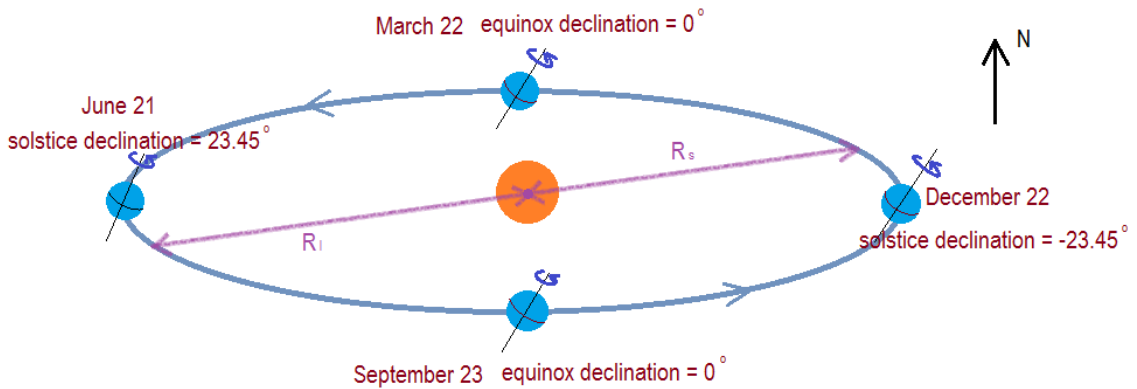


Fig 2.1.1 Schematic of the sun-earth rotation and variation of declination angle

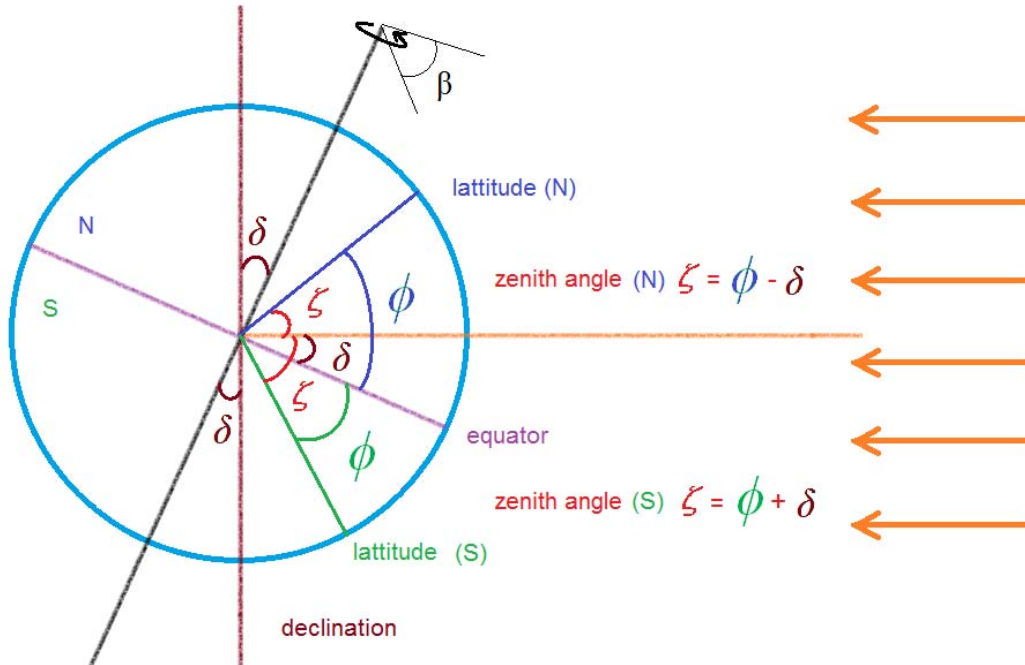


Fig 2.1.2 Schematic of variable angles effect power density and light path

As shown in Fig 2.1.1 and Fig 2.1.2, the power density at specific place varies with the time of the year (changing sun earth distance), the time of the day (changing tilt angle β) and the latitude (changing ϕ). As the light path varies, the sunlight spectrum received on earth differs, because of absorption effect.

2.1.2 Black body approximation of sunlight spectrum

Frequently commonly encountered light sources, including the sun and incandescent light bulbs, are closely modeled as "black body" emitters, which absorb all radiation incidents on their surface and emit radiation based on their temperature. In solar cell efficiency modeling, incident sunlight and its spectral distribution is approximated by the emission of a 5800 K black body. (A black body derives its name from the fact that, if it does not emit radiation in the visible range, it appears black.) The black body sources which are of interest to photovoltaics emit light spanning from UV (ultra violet) all the way to IR (infra-red) region, with peak in the visible region. The spectral irradiance from a black body is given by the radiation law^[6], shown in the following equation:

$$I(\lambda, T) = \frac{2\pi hc^2}{\lambda^5 \left(\exp\left(\frac{hc}{k\lambda T}\right) - 1 \right)} \quad (2.1.2)$$

where, λ is the wavelength of light;

T is the temperature of the black body (K);

I is the spectral irradiance in $Wm^{-2}m^{-1}$;

h , c and k are Plank constant, speed of light and Boltzmann constant respectively.

Obtaining proper results requires attention to the SI units, so that c is in m/s, h is in $J\cdot s$, T is in K , k is in J/K , λ is in meters and spectral irradiance in Wm^{-3} . Dividing by 10^9 gives the conventional units of spectral irradiance in $Wm^{-2}nm^{-1}$. The notation of $I(\lambda, T)$ denotes that the spectral irradiance changes with wavelength and temperature. Intensity variations with respect to wavelength or frequency are derived from the above equation (2.1.2)) and the response is illustrated in Fig 2.1.3. Here, what we are interested in is the intensity's relative contribution from each wavelength, e.g. within 1 J of incoming energy, what fraction is contributed by 300 nm or 500 nm wavelength.

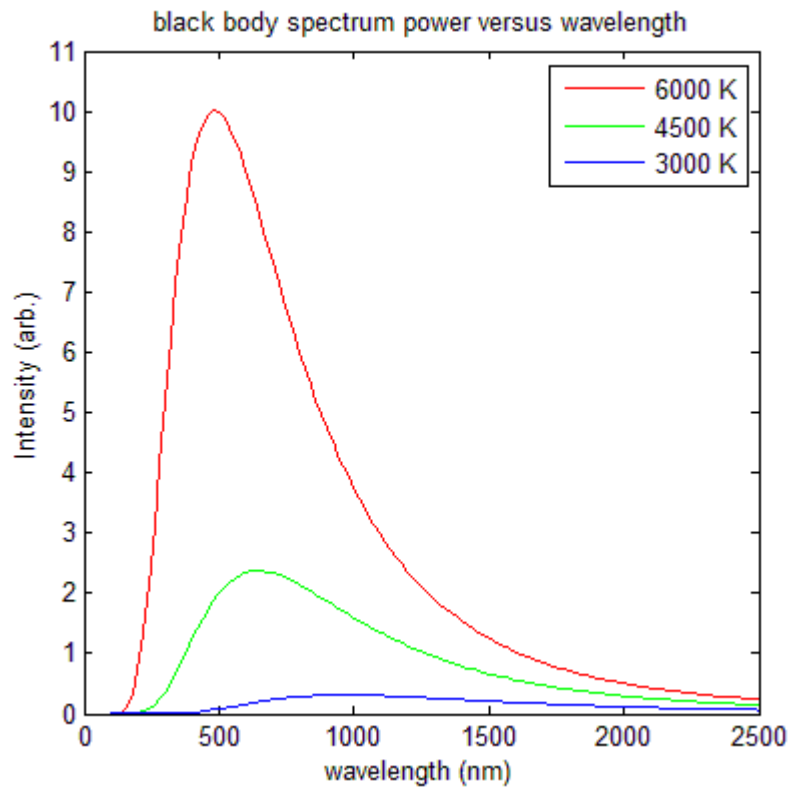


Fig 2.1.3 Variation of light intensity based on black body radiation with respect to wavelength and temperature

It should be noted that important parameter of a black body source is the wavelength at which the spectral irradiance is the highest. As the temperature decreases, the peak of the

black body radiation curve moves to longer wavelengths.

The peak wavelength of the spectral irradiance is determined by differentiating the spectral irradiance with respect to wavelength. The result is known as Wien's displacement law and is given by:

$$\lambda_p (\mu m) = \frac{2900}{T} \quad (2.1.3)$$

where, λ_p is the wavelength where the peak spectral irradiance is emitted and

T is the temperature of the black body (K).

The total power radiated by black body per unit area can be calculated by an integration of equation (2.1.2) over wavelength, which is known as Stefan-Boltzmann Law

$$P = \sigma T^4 \quad (2.1.4)$$

where, P is the power of energy per unit area of radiated object,

T is the absolute temperature,

$\sigma = 5.67 \cdot 10^{-8} \text{ W}/(\text{m}^2 \text{K}^4)$ is the Stefan-Boltzmann constant.

The total power emitted by the sun is a multiplication of the power per unit area by the surface area of the sun, which is equal to $\sigma T^4 * 4\pi R_{sun}^2 = 3.90 \cdot 10^{26} \text{ W}$.

2.1.3 Sunlight and atmosphere effect

Although the solar radiation incident on the earth's atmosphere is relatively stable, the radiation at the earth's surface varies widely due to several factors, like atmospheric effects, latitude, time of the year and time of day. These factors alter the overall power received, and the spectral content of the. These effects are summarized in the Fig 2.1.4.

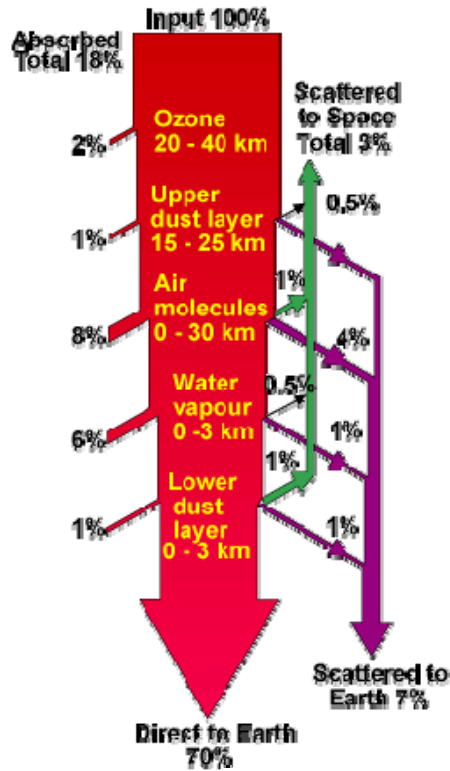


Fig 2.1.4 Atmospheric effects of light passing through the atmosphere

As solar radiation passes through the atmosphere, gasses, dust and aerosols absorb the incident photons. Specific gasses, notably ozone (O_3), carbon dioxide (CO_2), and water vapor (H_2O), have very high absorption of photons that have energies close to the bond energies of these atmospheric gases. This absorption yields deep troughs in the spectral radiation curve. For example, much of the far infrared light above $2 \mu m$ is absorbed by water vapor and carbon dioxide. Similarly, most of the ultraviolet light below $0.3 \mu m$ is absorbed by ozone.

While the absorption by specific gasses in the atmosphere changes the spectral content of the terrestrial solar radiation, they have a relatively minor impact on the overall power. Instead, the major factor reducing the power from solar radiation is the absorption and

scattering of light due to air molecules and dust. This absorption process does not produce the deep troughs in the spectrum, but rather causes a power reduction which is dependent on the path length through the atmosphere. When the sun is overhead, the absorption due to these atmospheric elements causes a relatively uniform reduction across the visible spectrum, hence incident light appears white. However, for longer path lengths, higher energy (shorter wavelength) light is more effectively absorbed and scattered. Hence in the morning and evening the sun appears more reddish and has a lower intensity than in the middle of the day.

2.1.4 Air Mass

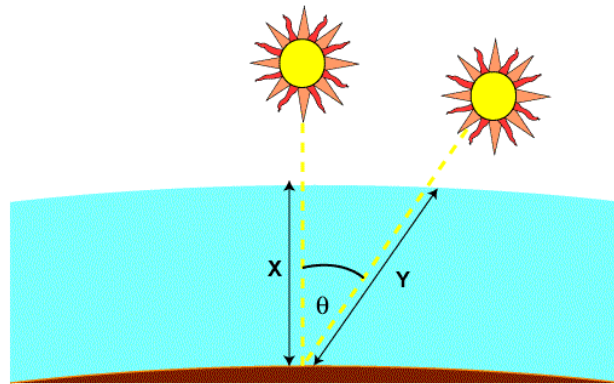


Fig 2.1.5 Definition of air mass

The spectrum we could use on earth is not an ideal black body radiation; first because the nuclear fusion which contributes to power the sun is not a black body heat source, second because a large number of troughs would show up after traveling through the atmosphere. Air Mass is the path length of light through the atmosphere normalized to the shortest possible path length (that is, when the sun is directly overhead). Air Mass quantifies the reduction in the power of light as it passes through the atmosphere and is absorbed by air

and dust. The Air Mass is defined as:

$$AM = \frac{1}{\cos \theta} \quad (2.1.5)$$

where, θ is the angle between the incident light and normal direction, called as zenith angle, as shown in Fig. 2.1.5.

AM 1.5G

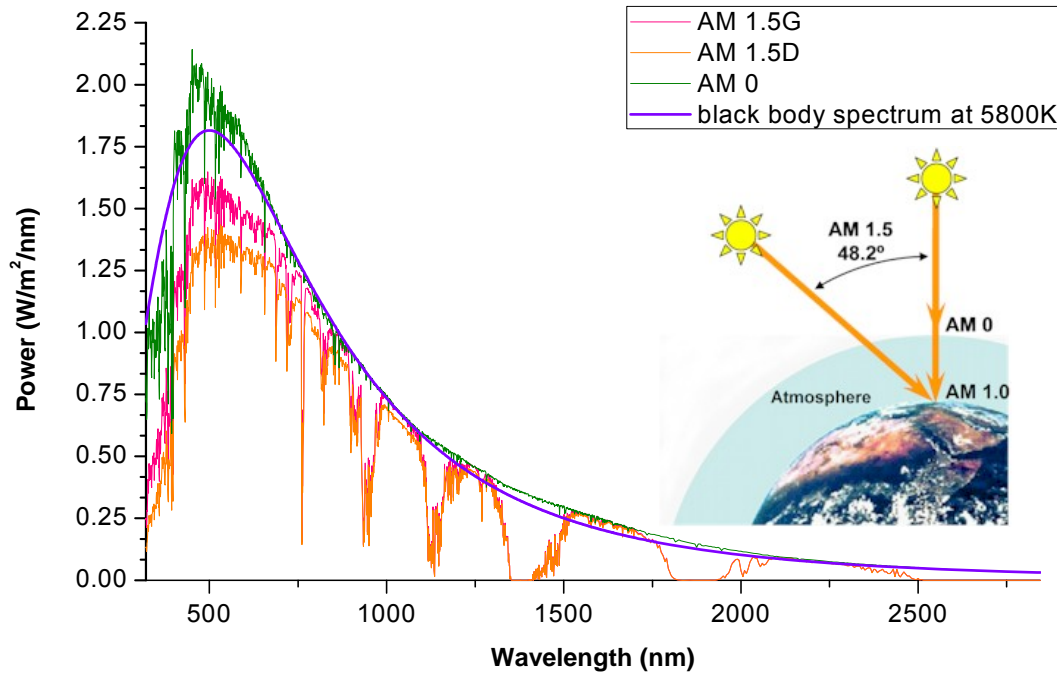


Fig 2.1.6 Comparison of black body radiation, AM0, AM 1.5G, and AM 1.5D

Generally, AM 1.5G, AM 1.5D, AM 0, 500 * AM 1.5D are used as standardized measure of sunlight spectrum. The number followed by AM has been defined earlier. AM0 is the radiant power density outside the Earth's atmosphere, having a value of 1353 W/m^2 . The number in front of AM (*i.e.* 500) refers to concentrated illumination of 500 times of the original spectrum. D refers to the light spectrum coming directly from the sun, while for

G besides the direct sun spectrum; the reflections from the surface are also taken into account (*i.e.* diffuse scattering due to clouds). The AM1.5 Direct (+circumsolar) spectrum is defined for solar concentrator. It includes the direct beam from the sun plus the circumsolar component in a disk of 2.5 degrees around the sun. The direct plus circumsolar spectrum has an integrated intensity of about 900 W/m^2 integrated power density.

Integrated power density in AM 1.5G is about 1000 W/m^2 . In this work, AM 1.5G spectrum is used for simulations. Fig 2.1.6 represents comparison of 5800 K black body radiation spectrum with three common radiation spectrums^[7]. It shows that at 5800 K, the black body spectrum gives a reasonable approximation for AM 0 over a wide wavelength band^[8].

2.2 Principle of Solar Cell Operation

Fig 2.2.1 represents solar cell with four steps of working; light coupling, carrier excitation, current collection, and dissipation of power in the load, more detailed explanation is given in later chapter 2.4: Practical Devices with Finite Absorption Coefficient. Photons with energy smaller than bandgap will pass through the material, without being absorbed; photons with energy equal to bandgap will generate electron-hole (e/h) pairs; photons with energy larger to bandgap will excite electron-hole pairs to higher energy states, and e/h pairs will relax to lowest energy state, with extra energy releasing as heat. When the external load is resistance, the solar cell is working as a power generator; when the external load is no resistance and (*i.e.* an ideal ampere meter), the amount of current flowing in the circuit is known as short circuit current J_{SC} ; when

the external load is infinite or no current is flowing (*i.e.* an ideal volt meter), the voltage drop between the two sides of solar cell is known as the open circuit voltage V_{OC} .

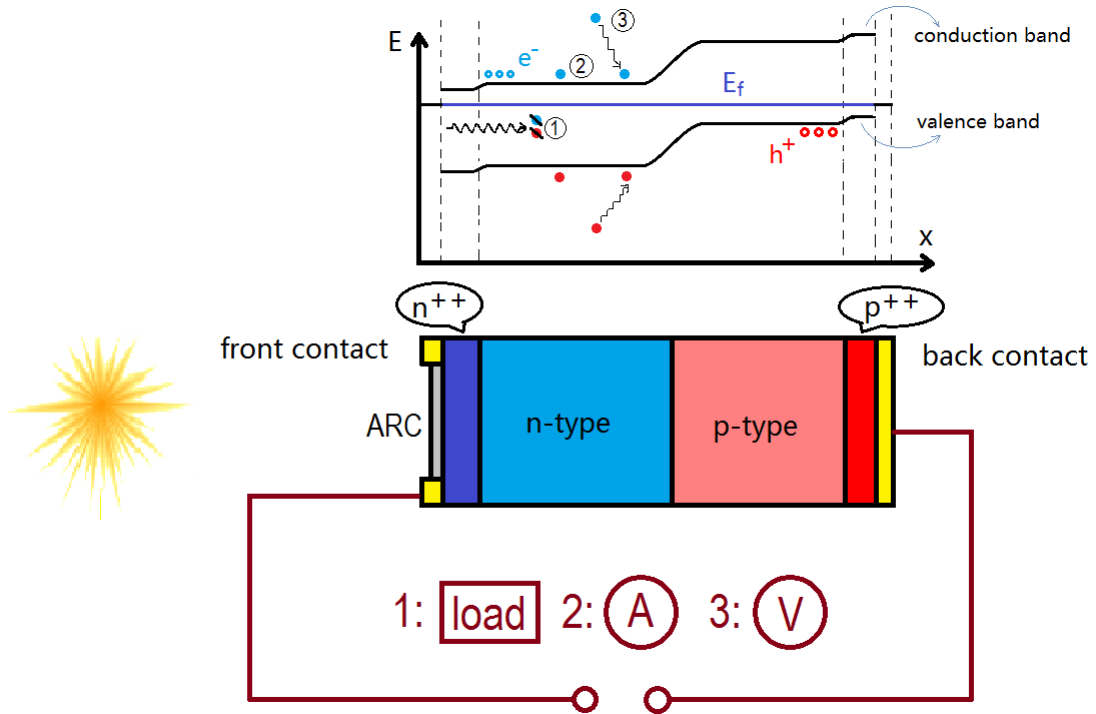


Fig 2.2.1 Schematic of solar cell operating principle

2.3 Ideal Solar Cell Efficiency Limit for Solar Cells

As discussed earlier, for a solar cell made with a single absorber material there is threshold energy, which is the bandgap E_g of the solar cell. Photons $E > E_{g1}$ will be absorbed by p-n junction, but photons $E < E_{g1}$ will go through the p-n junction, which loses part of the incident energy. Hence another material with bandgap $E_{g2} < E_{g1}$, can be used to harvest the photons whose energy $E_{g2} < E < E_{g1}$. This is the reason behind tandem or multi-junction solar cells.

2.3.1 Detailed balance energy limit

The detailed balance energy limit to model a single-junction solar cell, was introduced by Shockley and Queisser. It establishes an ideal efficiency limit as a function of the bandgap and cell operating temperature. This efficiency limit often referred as the Shockley-Queisser limit which is calculated by examining the amount of electrical energy that is extracted from incoming sunlight. It gives a prediction of an ideal single-junction solar cell for a given bandgap, which has several assumptions,

- The photon with energy below bandgap will not produce any electron-hole pair;
- The photon with energy above bandgap will produce one electron-hole pair; (Assume internal quantum efficiency equals 1. In reality, due to absorption and recombination issues, this is not the case.)
- Photons with energy E above bandgap E_g will convert energy equal to bandgap E_g , and thermalize the remaining energy $E-E_g$.
- Number of photons emitted (both for solar cell and light source) is predicted by Fermi Dirac distribution

From previous section 2.1 on sunlight spectrum properties, it is stated that any material above absolute zero temperature will emit radiation through black body radiation. Therefore, the solar cell receives N_r number of photons above bandgap (integrate photons from E_g to infinity) from the sun and emit photons N_e over the entire energy spectrum (integrate photons from zero to infinity) due to black body radiation. Assuming the temperature of the sun is T_s , the temperature of solar cell is T_c , and the bandgap for solar

cell is E_g , the net number of photons that solar cell can absorb is the difference between receiving and emitting $N_r(T_s, E_g, +\infty) - N_e(T_c, 0, +\infty)$ photons. Notations are labeled in Fig 2.3.1 (Detailed balance energy limit ignores reflection loss at the air-solar cell interface).

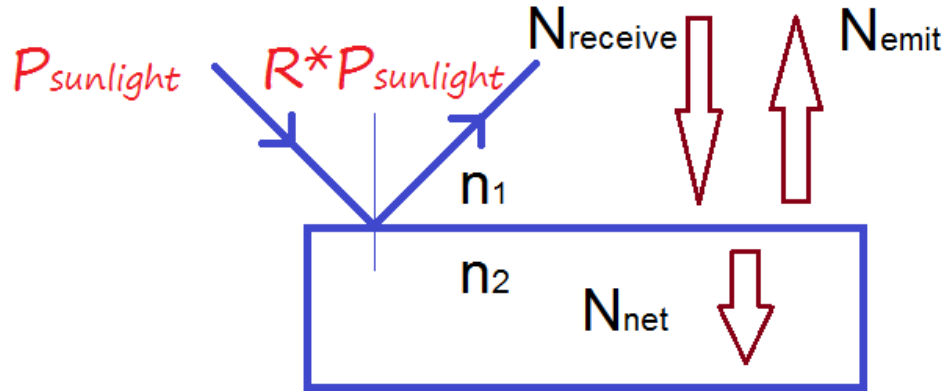


Fig 2.3.1 Physical parameters relevant to single-junction efficiency limit

Since solar cell is generally connected to an external load, which has potential difference on the two sides; the radiation term by solar cell should be modified^[9,10] by solar cell's chemical potential from energy $\hbar\omega$. The current generated by photons can be expressed by equation (2.3.4). Generated current $I(V)$ is electronic charge q multiplied by the net number of absorbed photons per second; *i.e.* $N_{\text{net}} = N_{\text{receive}} - N_{\text{emit}}$. The number of received photons needs to be multiplied by an etendue coefficient, because the sun's surface and earth's surface are at concentric spheres with different radii. Efficiency of the solar cell is the power produced over the power received from sun; which is expressed in equation (2.3.5). Set (a) in equation (2.3.3) refers to black body light source, while (b) is applicable for any spectrum source, like AM 0, AM 1.5G. (Since available spectrum database is commonly wavelength versus power intensity, the set (b) equations generally used)

$$N_{receive} = \frac{\pi \cdot C \cdot \sin^2 \theta \cdot n_1^2}{4\pi^3 \hbar^3 c_0^2} \int_{E_g}^{\infty} \frac{(\hbar\omega)^2}{e^{\frac{\hbar\omega}{kT_s}} - 1} d(\hbar\omega) \quad (2.3.1a)$$

$$N_{receive} = C \cdot n_1^2 \int_{E_g}^{\infty} \frac{Power(\lambda)}{hc_0 / \lambda} d\lambda \quad (2.3.1b)$$

$$N_{emit}(V) = \frac{\pi \cdot n_2^2}{4\pi^3 \hbar^3 c_0^2} \int_{E_g}^{\infty} \frac{(\hbar\omega)^2}{e^{\frac{(\hbar\omega - qV)}{kT_c}} - 1} d(\hbar\omega) \quad (2.3.2)$$

$$P_{sunlight} = \frac{\pi \cdot C \cdot \sin^2 \theta \cdot n_1^2}{4\pi^3 \hbar^3 c_0^2} \int_0^{\infty} \frac{(\hbar\omega)^3}{e^{\frac{\hbar\omega}{kT_s}} - 1} d(\hbar\omega) \quad (2.3.3a)$$

$$P_{sunlight} = C \cdot n_1^2 \int_0^{\infty} \frac{Power(\lambda)}{hc_0 / \lambda} d\lambda \quad (2.3.3b)$$

$$I(V) = q(N_{receive} - N_{emit}) \quad (2.3.4)$$

$$\eta = \frac{I \cdot V}{P_{sunlight}} \quad (2.3.5)$$

where, C is sun concentration, varying from 0 to 46500¹ (Without any concentrators, $C = 1$);

θ is half angle of radiation (the angle of the view of the sun) ;

k is the Boltzmann constant;

\hbar is the reduced Planck constant, or called the Dirac constant after Paul Dirac;

¹ As the definition of etendue, if there was a concentrator with concentration factor C in front of solar cell, the maximum concentrating effect is the same as putting solar cell, which means etendue equals to π , so the limit of C is given by $\pi / (6.75 \cdot 10^{-5}) = 46500$.

T_s is the temperature of sun;

T_c is the temperature of solar cell;

ω is circular frequency of incident photon;

c_0 is the velocity of photons in vacuum;

q is electron charge;

n_1, n_2 are the refractive index for the air and solar cell respectively.

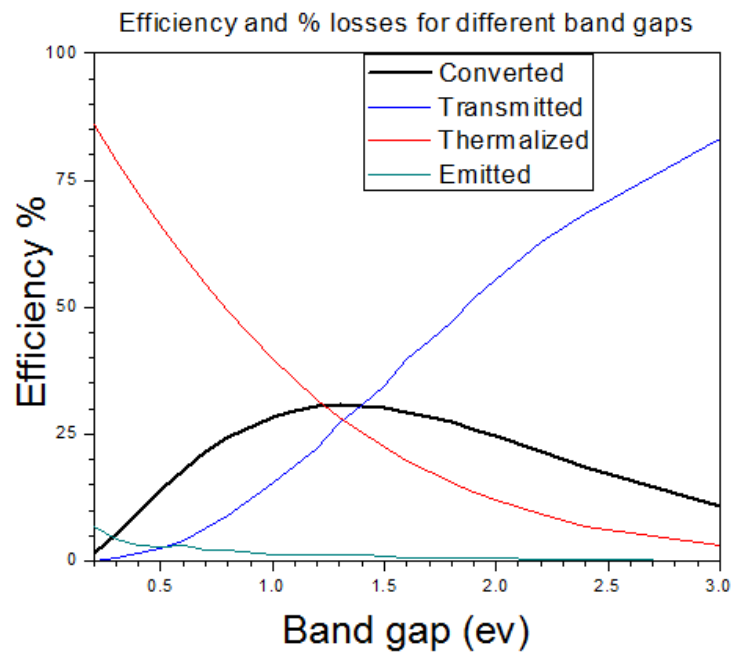


Fig 2.3.2 Converted, transmitted, thermalized, and emitted photon efficiency as a function of bandgap

The incoming photons with energy below bandgap will transmit through the solar cell, as shown by blue curve labeled transmitted in Fig 2.3.2. The incoming photons with energy above bandgap will be transformed into e-h pairs, and the extra energy $E-E_g$ will be lost in form of heat, as shown by red curve labeled thermalized. The solar cell operating at a

certain temperature will emit photons approximated by black body, as shown by green curve labeled emitted. The amount of converted photons, shown by black curve labeled converted, is the total number of photons incident minus the sum of emitted, transmitted and thermalized photons. Fig 2.3.2 shows efficiencies of different processes versus bandgap.

In case of a solar cell at ambient room temperature, 300 K, emitted energy is due to black body radiation. This energy cannot be captured by the cell, and represents about 7% of the total available incoming energy. The efficiency is the current I generated multiplied by the external potential V over the incoming power P . The proper design should have the biggest IV value.

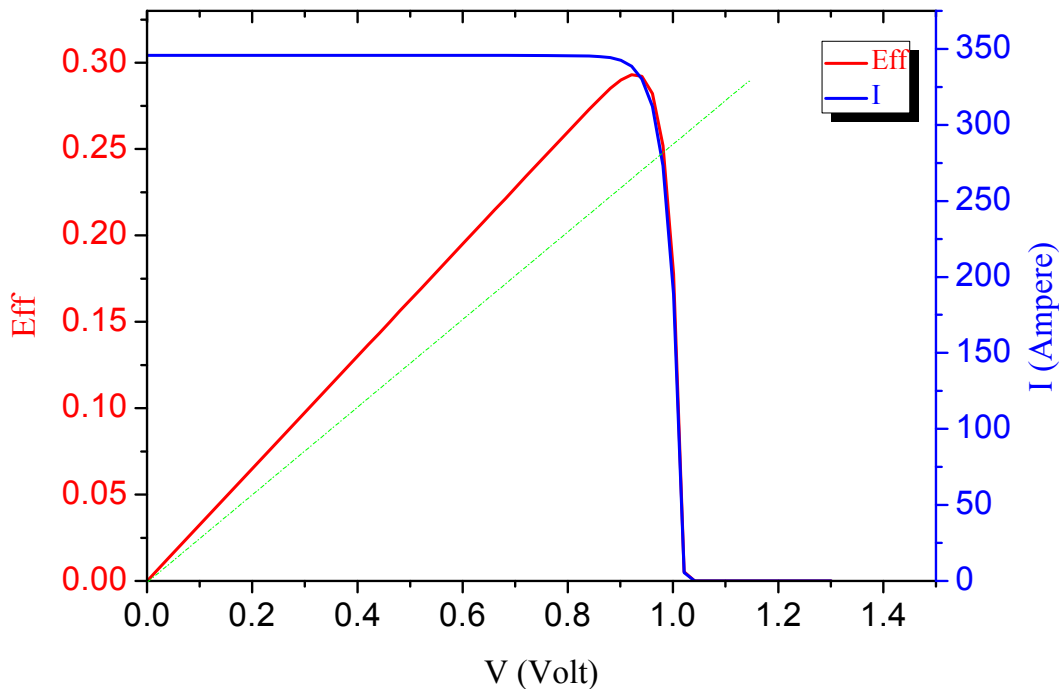


Fig 2.3.3 I-V characteristic of single-junction solar cell with bandgap $E_g = 1.35 \text{ eV}$

Fig 2.3.3 illustrates the external potential versus generating current relation for fixed bandgap material. It demonstrates that the maximum efficiency would be reached only at a specific point, corresponding to single set of current and external potential value (V_{max}, I_{max}). So the highest efficiency of solar cell requires the external load to have resistance equal to $R = V_{max}/I_{max}$.

For terrestrial applications the efficiency limit calculations use a standardized AM 1.5 G spectrums with realistic refractive indices, rather than ideal black body radiation with refractive index of 1. Fig 2.3.4 depicts such efficiency calculation with a refractive index of 3.3 (*i.e.* GaAs) illustrating that the maximum attainable efficiency increases with concentration. This indicates that concentration is a good approach to increase efficiency, and the optimal value of the bandgap decreases with increase in concentration

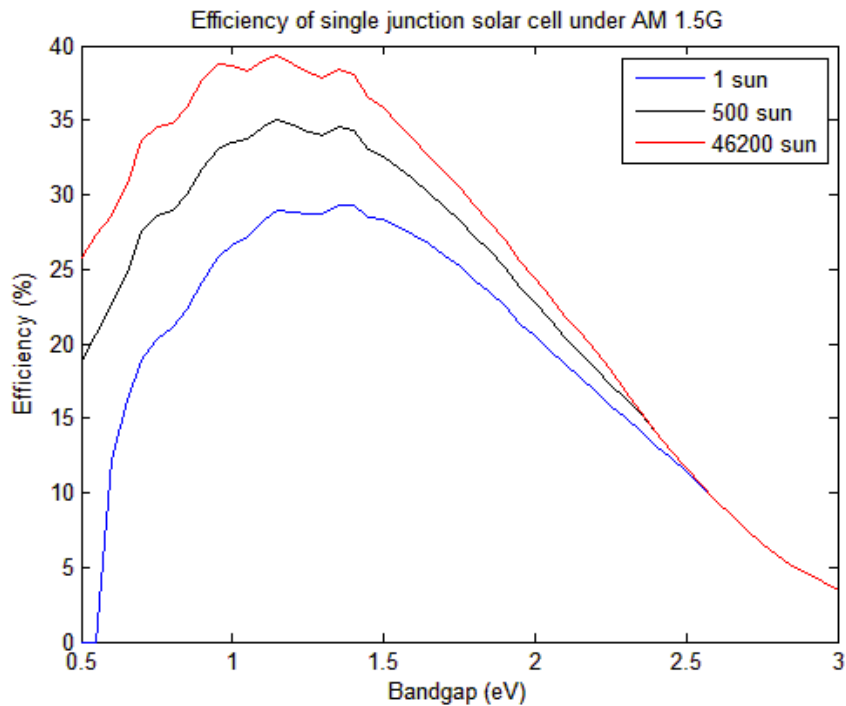


Fig 2.3.4 Ideal single-junction efficiency versus bandgap under AM 1.5G for different sun concentrations

2.3.2 Theoretical efficiency limit for tandem and multi-junction solar cell

In an attempt to achieve higher efficiency, two main approaches can be considered to increase photon absorption. One way is splitting spectrum source by parallel connecting cells with beam splitters which makes each cell work in narrow spectrum region, instead of full spectrum contributing to higher thermalized loss; and the other way is improving solar cell mechanism as shown in Fig 2.3.5, by reducing transmission and heat loss. Series connected absorbers are widely used to increase voltage; while sacrificing small amount of current. In a two-junction solar cell or tandem solar cell, transparency loss is reduced by adding another solar cell whose bandgap is below the first solar cell's bandgap. Efficiency of cell may be improved as the 2 bandgaps can be adjusted to get maximum efficiency. Multi-junction solar cells have 3 subcells which absorb wider spectrum of light radiation. Using three subcells the transparency loss is further reduced.

From the efficiency calculation in previous sub-chapter 2.3.1, a solar cell's efficiency is determined by choosing the bandgap and applying certain external potential. Hence, the efficiency for multi-junction solar cells is determined by bandgap of each subcell and external applied potential applied to them individually.

Multi-junction solar cells divide a spectrum into several regions, and each subcell absorbs energies in their working region. For a two-junction solar cell, whose bandgaps for top and bottom subcells are E_{g1} and E_{g2} respectively, the current of the device is the smaller one of the two subcells; and the voltage is the sum of two subcells. (In series, currents in both subcells are equal, where the larger current will be reduced by heat loss.) From the equation (2.3.1)-(2.3.5), we can find the current in each subcell, and the efficiency of

whole device is determined by equation (2.3.6)-(2.3.10). i in equation (2.3.9) refers to the index of subcells. (Here, equations are using light source as a black body, which can be replaced by any realistic sources using equations in chapter 2.3.1 set (b).)

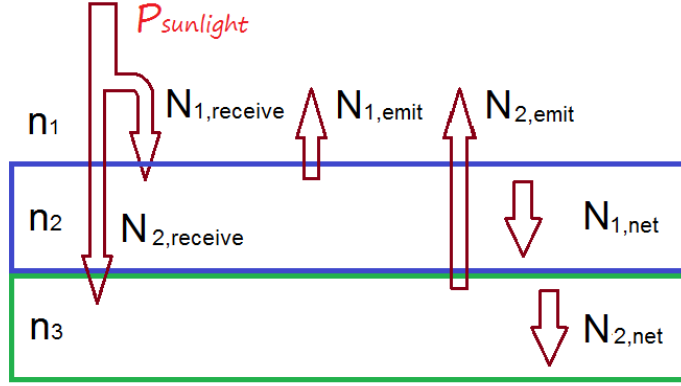


Fig 2.3.5 Schematic of tandem solar cell showing different parameters used

$$N_{1,receive} = \frac{\pi \cdot C \cdot \sin^2 \theta \cdot n_1^2}{4\pi^3 \hbar^3 c_0^2} \int_{E_{g1}}^{\infty} \frac{(\hbar\omega)^2}{e^{\frac{\hbar\omega}{kT_s}} - 1} d(\hbar\omega)$$

$$N_{2,receive} = \frac{\pi \cdot C \cdot \sin^2 \theta \cdot n_1^2}{4\pi^3 \hbar^3 c_0^2} \int_{E_{g2}}^{E_{g1}} \frac{(\hbar\omega)^2}{e^{\frac{\hbar\omega}{kT_s}} - 1} d(\hbar\omega) \quad (2.3.6)$$

$$N_{1,emit}(V_1) = \frac{\pi \cdot n_2^2}{4\pi^3 \hbar^3 c_0^2} \int_{E_{g1}}^{\infty} \frac{(\hbar\omega)^2}{e^{\frac{(\hbar\omega - qV_1)}{kT_c}} - 1} d(\hbar\omega)$$

$$N_{2,emit}(V_2) = \frac{\pi \cdot n_2^2}{4\pi^3 \hbar^3 c_0^2} \int_{E_{g2}}^{\infty} \frac{(\hbar\omega)^2}{e^{\frac{(\hbar\omega - qV_2)}{kT_c}} - 1} d(\hbar\omega) \quad (2.3.7)$$

$$P_{sunlight} = \frac{\pi \cdot C \cdot \sin^2 \theta \cdot n_1^2}{4\pi^3 \hbar^3 c_0^2} \int_0^{\infty} \frac{(\hbar\omega)^3}{e^{\frac{\hbar\omega}{kT_s}} - 1} d(\hbar\omega) \quad (2.3.8)$$

$$I_i(V) = q(N_{i,receive} - N_{i,emit}) \quad (2.3.9)$$

$$\eta = \frac{\min(I_1, I_2) \cdot (V_1 + V_2)}{P_{sunlight}} \quad (2.3.10)$$

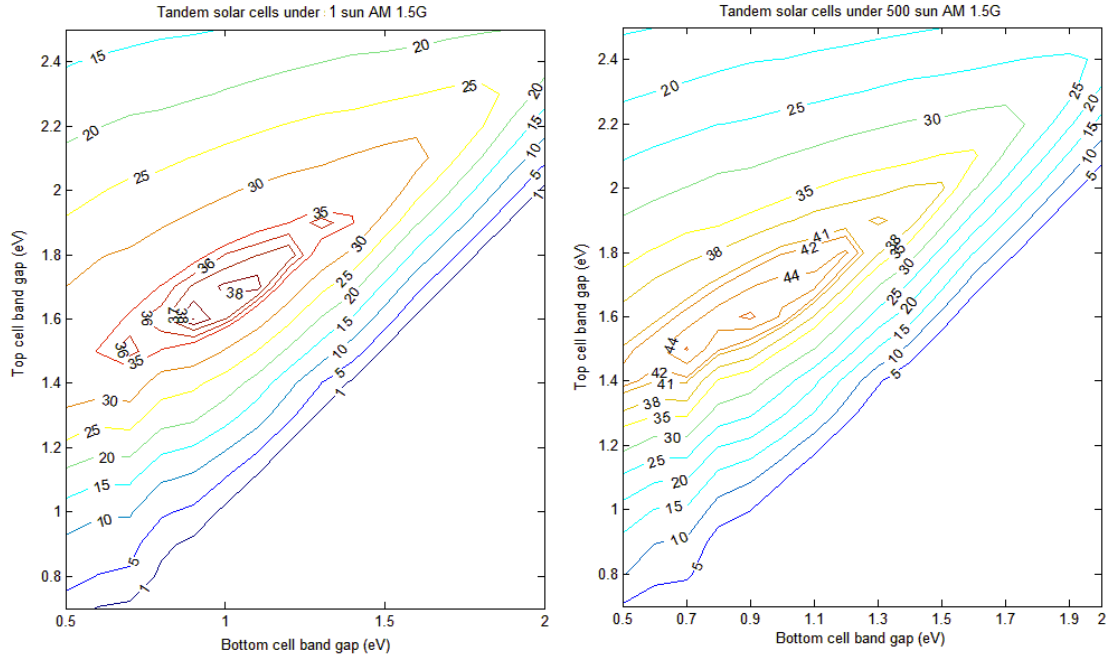


Fig 2.3.6 Bandgap optimization and efficiency calculation of tandem under AM 1.5G spectrum with 1 sun and 500 sun concentration

Fig 2.3.6 shows that for tandem, in case $E_{g1} < E_{g2}$, the efficiency (current) of the device is zero, because the bottom subcell cannot absorb any photon, which leads to zero current. Also, the external potential, which is the chemical potential (the difference between two quasi Fermi level of electrons' and holes), cannot be larger than corresponding bandgaps of the subcells.

In 3-junction or multi-junction cells, whose bandgaps are $E_{g1} > E_{g2} > E_{g3}$ from top to bottom, the top cell would utilize the photons with energy above E_{g1} , the middle cell would utilize the photons with energy between E_{g1} and E_{g2} , and the bottom cell would

utilize the photons with energy between E_{g2} and E_{g3} . Since subcells are connected in series, only the lowest current of the subcells would be considered as the limiting total current (while the extra current in the other cells would be lost in the form of heat), and voltage of subcells will be added. Optimization for each bandgap of different solar cell models, the efficiency limit, and devices' final current are presented in Table 2.3.1.

Concentration		Single-junction	Double junctions	Triple junction	Triple junctions Ge bottom cell
1 sun	Bandgap(eV)	1.35	1.6, 0.9	2.0,1.4,0.9	1.9, 1.2
	Efficiency (%)	29.3	39.0	44.75	39.7
	Current (mA/cm^2)	32.9	25.2	171.9	19.7
500 sun	Bandgap(eV)	1.15	1.6, 0.9	2.0,1.4,0.9	1.9, 1.2
	Efficiency (%)	35.1	46.4	52.1	48.1
	Current (mA/cm^2)	20761	12649	8649	9828
46200 sun	Bandgap(eV)	1.15	1.5, 0.7	2.0,1.4,0.9	1.9, 1.2
	Efficiency (%)	39.4	51.8	57.5	54.2
	Current (mA/cm^2)	$1.938*10^6$	$1.340*10^6$	$7.974*10^5$	$9.066*10^5$

Table 2.3.1 Optimized bandgap and efficiency limit for single/double/triple junction under various concentration factors

Hence the maximum efficiency for single-junction devices under one sun is 29.3% (1.35 eV); the maximum efficiency for double junctions devices, under one sun is 39.02% (1.6 eV , 0.9 eV); the maximum efficiency for triple junctions devices with Ge (0.67 eV) fixed for bottom subcell under one sun is 39.68% (1.9 eV , 1.2 eV , 0.67 eV). Consequently, the greater the number of junctions there are, the higher ideal maximum efficiency can be

achieved. Under 46200 sun as maximum concentration, the maximum efficiency for single-junction devices is 49.37% (1.15 eV); the maximum efficiency for double junctions devices is 51.81% (1.5 eV, 0.7 eV); the maximum efficiency for triple junctions devices with Ge (0.67 eV) bottom cell is 54.23% (1.9 eV, 1.2 eV, 0.67 eV). Consequently, the larger sun concentration there is, the higher maximum efficiency would be achieved. Hence concentrator is an effective approach to enhance solar cell's efficiency; however concentrator brings out wide range of incident angle coupling in the device as a challenge. Fig 2.3.7 gives an example of lattice matched (LM) multi-junction with traditional duo-layer antireflection coating working under concentration.

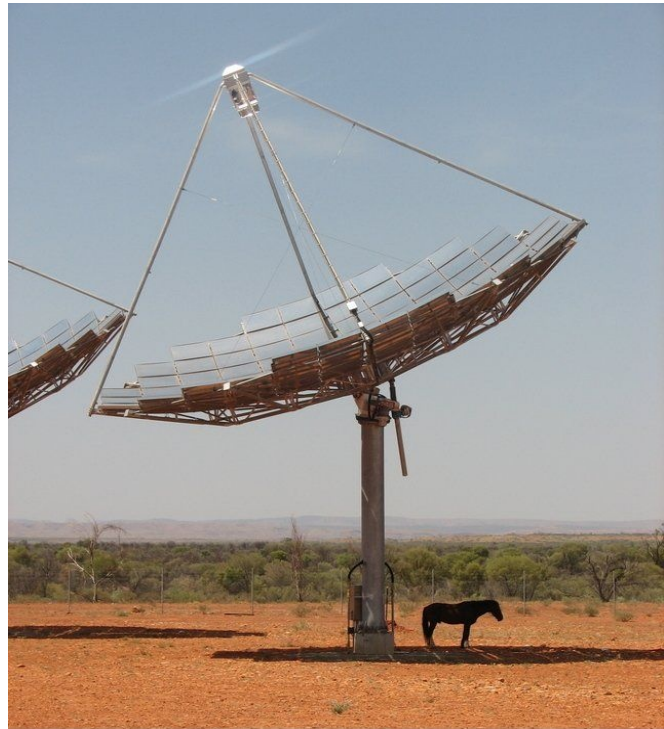
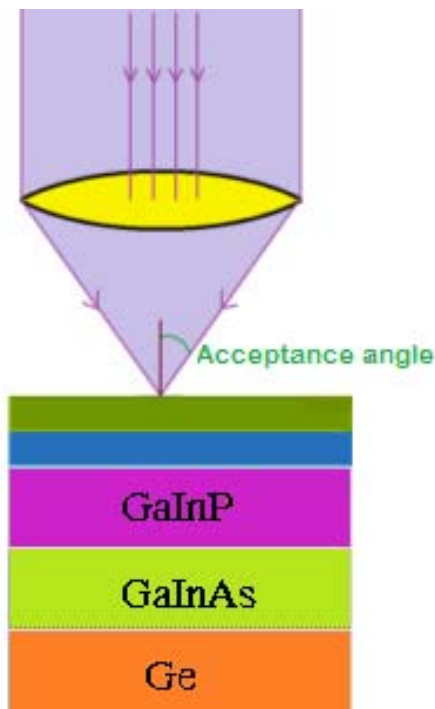


Fig 2.3.7 An example of LM multi-junction device operated under concentrator and an example of concentrated photovoltaic (CPV) system

2.4 Practical Devices with Finite Absorption Coefficient

It can be seen that the detailed balance limit is for ideal solar cells, absorbing all the energy above bandgap, complete transfer of photons to e-h pairs, with no energy loss inside the solar cell itself. A practical device would have finite absorption, limited minority carrier transport ability, surface recombination, surface reflection, shadow loss, and resistance loss (from electrodes). Finite absorption and carrier's transport in ability problems are usually solved by carefully designing the thickness and doping concentrations in the device; surface recombination is reduced by surface passivation techniques (*i.e.* inclusion of a highly doped thin window layer of a wider bandgap semiconductor); Front grid shadowing loss is reduced by proper design of front surface contact grid or/and use of transparent conductive electrodes ; resistive losses are reduced by using highly conductive electrode material (Au, Au-Ge); and reflection is reduced by incorporation of antireflection coatings or other light trapping schemes (texturing, plasmonics,..). Many of these loss mitigation approaches requires tradeoffs as often optimizing one parameter affects detrimentally another one. Issues pertaining to optimization of reflective losses and some more common approaches used in the literature will be discussed in detail in subsequent chapters. These losses originate between the detail balanced efficiency projections and practical realizations. Fig 2.4.1 illustrates best theoretical efficiency projections and some confirmed best experimental efficiencies for single-junction solar cells.

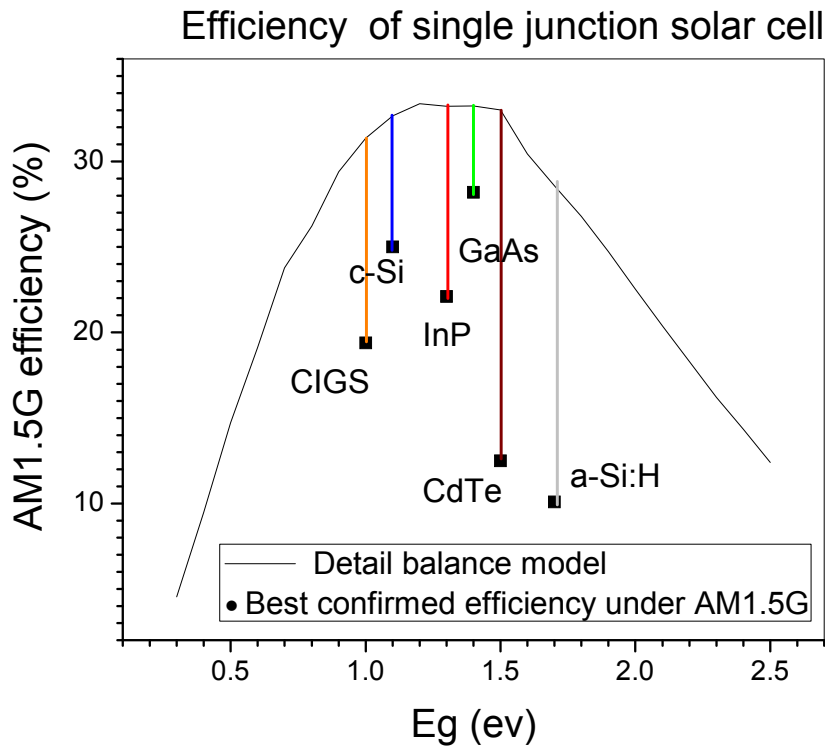


Fig 2.4.1 Comparison of confirmed practical solar cell efficiency with theoretical efficiency. Experimental data extracted from solar cell efficiency tables (version 40) ^[11]

Shockley and Queisser's work considered ideal devices; there are a number of other factors that further reduce the theoretical efficiency. These factors are finite probability for photons to generate e-h pairs, the fact that existing e-h pairs can recombine, finite absorption coefficients, and devices' thickness. The detail balance model is an ideal model that doesn't take into account the physical properties of the semiconductor. Shockley and Queisser's efficiency is far higher than that of any states-of-the-art solar cells experimentally produce. The huge gap between predicted and experimental efficiency comes from ignoring finite absorption coefficient, finite diffusion length, and reflected photon loss in the front surface of solar cells, which demands a better model which explains the efficiencies much more accurately.

2.4.1 Absorption coefficient

Absorption coefficient is described by how easy or hard it is for photons to be converted into e-h pairs. Fig 2.4.2 shows a few common solar cell materials' absorption coefficient. Indirect bandgap materials, like Si, have smaller absorption coefficient comparing with direct bandgap materials, like GaAs. The intensity of light after passing through certain material, whose absorption coefficient is α and thickness is l , is $\exp(-\alpha * l)$. This indicates that large absorption coefficient and/or long light path would generate more e-h pairs. However, the generated e-h pairs would recombine, due to finite minority carrier's diffusion length, which is the average length a carrier moves between generation and recombination. Hence, an optimized thickness is required to obtain maximum current, by doing a tradeoff between diffusion and absorption.

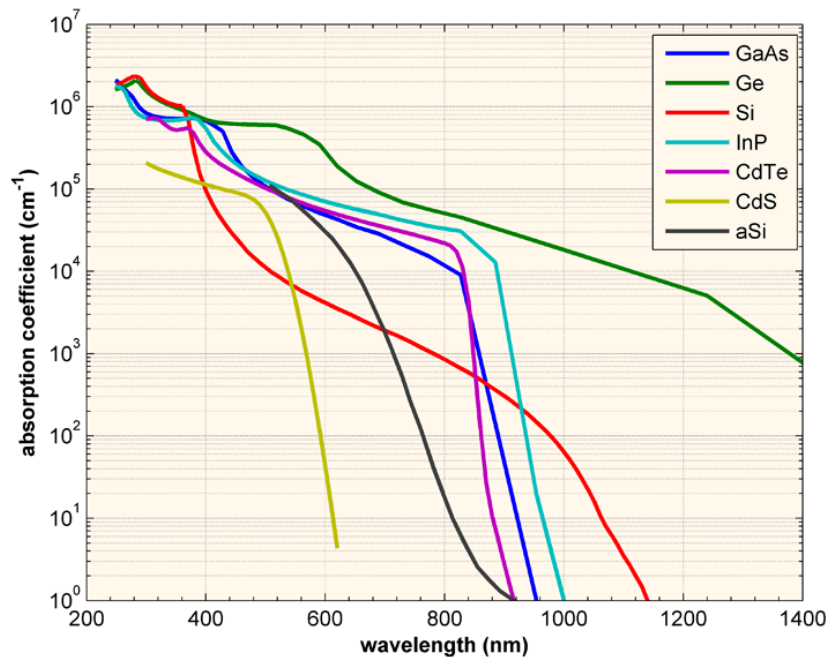


Fig 2.4.2 Absorption coefficient of commonly used semiconductor materials

For a direct bandgap material, the absorption coefficient follows equation ^[12] (2.4.1).

$$\alpha \approx A^* \sqrt{h\nu - E_g}, \text{ with } A^* = \frac{q^2 x_{vc}^2 (2m_r)^{3/2}}{\lambda_0 \epsilon_0 \hbar^3 n} \quad (2.4.1)$$

where, ν is light frequency

h is Planck's constant

E_g is the bandgap energy

m_r is the reduced mass, $m_r = \frac{m_h^* m_e^*}{m_h^* + m_e^*}$, where m_e^* and m_h^* are the effective mass of electron and hole respectively.

q is the elementary charge

n is the (real) index of refraction

ϵ_0 is the vacuum permittivity

x_{vc} is a matrix element, in electric field cross polarization matrix, with units of length and typical value the same order of magnitude as the lattice constant

For the indirect bandgap, the absorption coefficient can be approximated by ^[13]

$$\alpha \propto \frac{(h\nu - E_g + E_p)^2}{\exp\left(\frac{E_p}{kT}\right) - 1} - \frac{(h\nu - E_g - E_p)^2}{\exp\left(-\frac{E_p}{kT}\right) - 1} \quad (2.4.2)$$

where, E_p is the energy of the phonon that assists in the transition.

These two equations are valid only for photons' energy being larger (but not by too much) than the bandgap (more specifically, assuming that the bands are approximately parabolic), and ignoring all other sources of absorption other than the band-to-band absorption in

question, as well as the electrical attraction between the newly created electron and hole. They are also invalid in the case that the direct transition is forbidden, or in the case that many of states in the valence band are empty or states in conduction band are full.

2.4.2 Drift diffusion model

The drift diffusion model takes more details into account, such as recombination which includes minority carrier diffusion length, diffusion coefficient or minority carrier life time, surface recombination, and Shockley-Read-Hall (SRH) recombination² in depleted or i-region, doping for both acceptor and donor, sun spectrum (AM 1.5 G or AM 0 or ideal black body radiation), shadowing loss (caused by electrode coverage), reflection loss and absorption. The minority carrier diffusion length depends on doping, increase in doping causes diffusion length to reduce, hence e-h pairs will recombine in shorter distance for highly doped p-n junctions. However, for low doping, the built in potential would be small which would decrease the operating voltage of the solar cell.

Like detailed balance model, this model also takes into account the transmission losses below the bandgap. The photons whose energy E are less than bandgap E_g will just pass through semiconductor (so the extinction coefficient k and absorption coefficient follow

$\alpha = \frac{4\pi k}{\lambda_0}$, and absorption is zero when $E < E_g$, where λ_0 is the wavelength in vacuum).

² SRH recombination happens through defects, and not in pure, no-defect materials. This process contains two steps, which are 1) an electron (or hole) gets trapped in forbidden band's energy state, which is resulted from crystal defects, and 2) if a hole (or electron) moves to the same energy state before the previous electron (or hole) thermally re-emitted, the electron and hole would recombine.

Photons having energy E larger or equal to bandgap E_g will contribute to the generation of e-h pairs. The extra energy $E-E_g$ will be lost in the form of heat by lattice vibration (phonons). Since semiconductors' absorption represents how long the photons can travel through before being generated into e-h pairs, thicker semiconductor can confirm that most photons are in use; however semiconductors' minority carriers have a finite diffusion length and life time, and it is necessary to have finite thickness of p-n junction, generally smaller than diffusion length, so that maximum number of charge can be collected before recombination.

The surface of semiconductors contains interface traps which act as recombination centers and reduce the number of e-h pairs extracted out of the device. This surface recombination can be reduced by using a passivation layer, which will be discussed in the later part of this chapter.

By solving drift-diffusion equations for p-n junction, equations (2.4.3) can be used to predict I-V characteristics of solar cells^[14,15].

$$J = (J_{0p} + J_{0n}) \left(e^{\frac{qv}{kT}} - 1 \right) - J_{1p} - J_{1n} - J_{dep} + J_r \quad (2.4.3)$$

where, J_{0p} is recombination in p type region due to applied voltage;

J_{0n} is recombination in n type region due to applied voltage;

J_{1p} is generation of e-h pairs in p type region;

J_{1n} is generation of e-h pairs in n type region;

J_{dep} is the current generated by photons in depleted region;

J_r is the Shockley-Read-Hall recombination in depleted region present due to defect trap at mid bandgap.

The calculation formulae of all the current terms (J_{0p} , J_{0n} , J_{1p} , J_{1n} , J_{dep} , J_r) in each region can be found in Appendix A.

2.4.3 Design limitations for crystalline III-V multi-junctions: description of a few solar cell designs

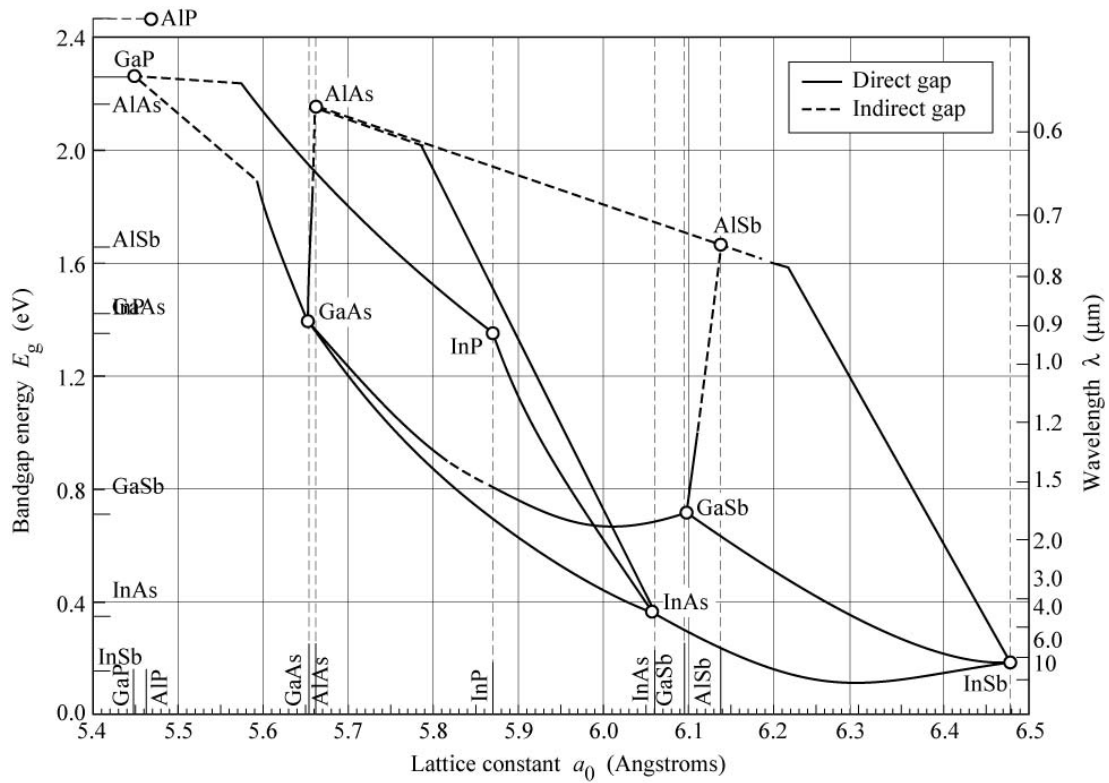


Fig 2.4.3 Bandgap energy and lattice constant of various III-V semiconductors at room temperature

In the fabrication of solar cells, lattice matching is one of the major considerations for growth, even with epitaxial techniques such as MBE and CBE. Lattice mismatching would contribute defects, which increases SRH recombination, reduces e-h pairs diffusion length and reduces subsequent current collection, reducing efficiency.

Consequently, the optional materials for each subcell should fit the optimized bandgap and best suit (lattice constant of) the other subcells' as shown in Fig 2.4.3^[16], or fabrication techniques that avoid defects have to be used. Two commonly used techniques, buffer layer and inverted metamorphic multi-junction, are explained as examples in appendix C.

Although the ideal 3-junction solar cells could be with the bandgap of 2.0 eV, 1.4 eV and 0.9 eV, getting 46.5% efficiency, the corresponding materials have a lattice mismatch, hence the material and the efficiency is constrained by lattice matching condition. Some techniques have been invited to address the lattice matching problem, such as growing buffer layers between two junctions to connect two different lattice constants, and inverted metamorphic multi-junction by controlling the junctions' growth order (general methods from bottom cells to top cells, IMM from top cells to bottom cells). (These two techniques would be demonstrated in appendix.) There are mainly three groups of solar cells in multi-junction devices, such as lattice matched (LM) multi-junction, metamorphic multi-junction (MM)^[17], and inverted metamorphic multi-junction (IMM)^[18] solar cells, each defined by their lattice matching issue and fabrication technique.

The only lattice matching 3-junction GaInP / GaAs / Ge solar cell would always have a current abundance in Ge subcell, and be current limited in GaAs subcell. One of the improvements in design is to reduce the thickness of GaInP subcell, and let part of the photons above its bandgap escape to GaAs subcell. Hence GaAs would use photons in both its own working spectrum and part of GaInP subcell's, increasing the minimum current among all the subcells.

2.5 Minimizing Front Surface Reflection Losses in Solar Cells

From the discussion of solar cell's mechanism and technologies, it is apparent that a broad band of working spectrum and a high concentration parameter are the crucial factors for high efficiency multi-junction solar cells. At the interface of two media with refractive indices n_1 and n_2 , there is $\left| \frac{n_1 - n_2}{n_1 + n_2} \right|^2$ energy loss at the boundary for normal incident light, from Fresnel Equation, shown in chapter 4 and derived in the Appendix. The commonly used semiconductors have a range of refractive indices 3.5~4, leading to 30%~40% energy loss for normal light from reflection directly, and even higher for off-normal light. This large loss due to reflection is not acceptable compared to all the other techniques and device designs aim to improve solar cell bandgap, thickness, buffer layer optimization and lattice matching. Hence there is an intense requirement to avoid or at least reduce the surface reflection. In accordance with the multi-junction and high concentration applications, the antireflection structure has to be effective in a wide band window and have angular tolerance. The conventional and most widely used dual layer of antireflection could work well at normal light, but as the incident angle increases, its antireflection property degrades. Consequently, a more complex structure is needed to solve the angular tolerance issue.

Fig 2.5.1 shows two examples of reflectivity, Si and AlGaAs. Si is the most commonly used solar cell material, and AlGaAs is widely used as a window layer for III-V solar cells for surface passivation due to its high bandgap. It is illustrated that Si has a higher reflectivity, due to its larger refractive index. Consequently, a large mismatch is the

crucial factor causing reflection, and the main idea to reduce reflection is to find some material whose index is between that of air and semiconductor, reducing the indices mismatch, which is the selection principle of ARC materials.

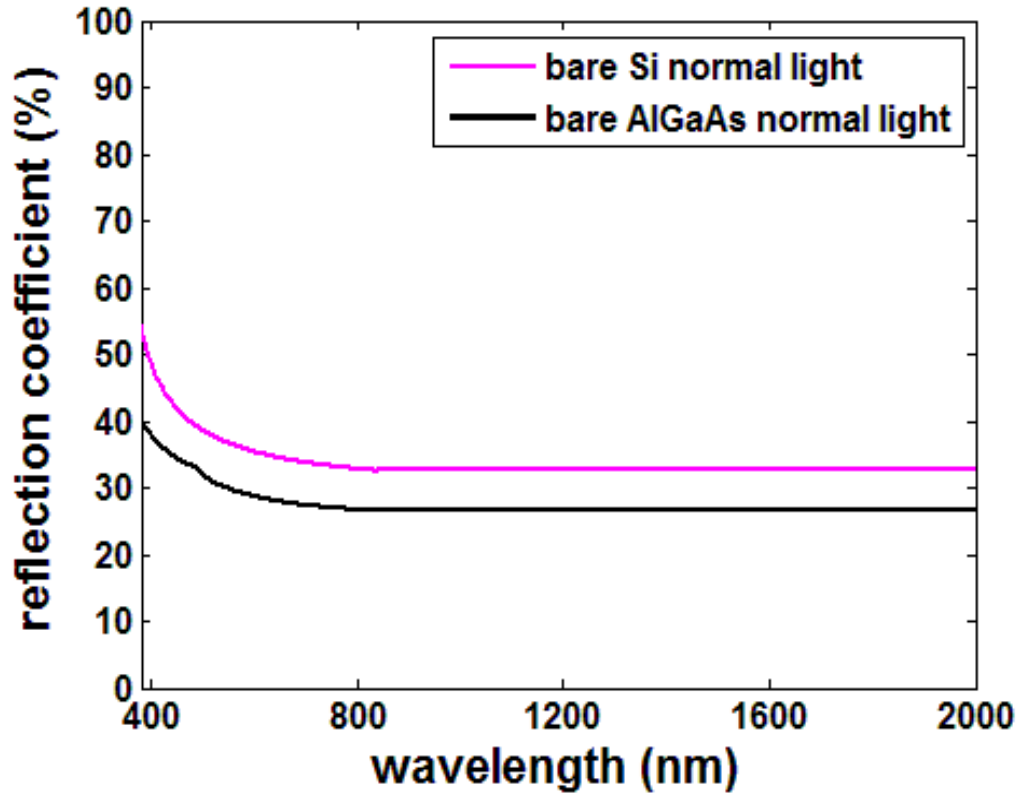


Fig 2.5.1 Reflectivity of Si and AlGaAs bare substrates under normal light

2.5.1 Single-layer ARC

The well-known single-layer ARC, with thickness equal to a quarter of wavelength in the media, and index equal to the square root of two materials' indices on the sides, can reach zero reflectivity for a single wavelength. However, the solar cells' working spectrum is a broad band region. For example, this band is from 380 nm to 1200 nm for Si solar cell.

Fig 2.5.2 illustrates that with AM1.5G spectrum over Si solar cell working spectrum,

9.2% photon would be lost at optimized 80 nm planar SiN single-layer. It can be predicted that there is a greater photon loss over a more extensive spectrum, such as a multi-junction solar cells' working band. So, more advanced ARC having property of wider low reflectivity is required for solar cells' application.

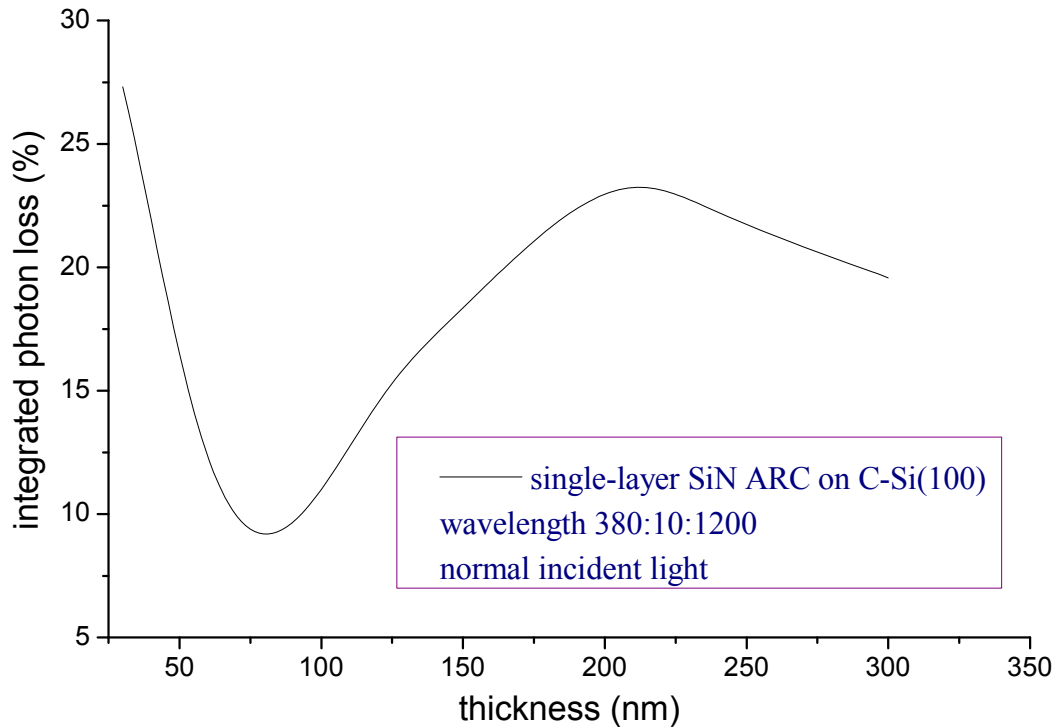


Fig 2.5.2 Integrated photon loss of single-layer SiN thickness dependence on crystal Si (100) substrate under normal light over the spectrum 380~1200 nm

2.5.2 Double-layer ARC—most widely used

As demonstrated in Fig 2.5.3, optimized double-layer ARC (for both, the selection of the materials and their coating thicknesses) can highly reduce reflectivity over a wide band. But as the incident angle increases, as much as 60° off-normal incidence, the antireflection property degrades. Chapter 3 is going to state why the double-layer ARC is more in favor among planar coating compared with other number of layers. For solar cell

panel exposure to natural sunshine, traditional SiN single-layer planar AR coating could achieve around 10% integrated reflectivity for normal light, and MgF₂-ZnS double-layer planar AR coating could achieve 5% integrated reflectivity for normal incident light. Trackers with intensity sensors can keep incident angle normal to the panel, in order to maintain minimum reflectivity, avoiding large zenith angle, such as the commercial Si solar panel often working with tracker, either one-direction or two-direction controlled. However, a typical multi-junction solar cell with higher efficiency is generally working with concentrators to further harvest light transmission, resulting in an integral of wide zenith angle that is not solvable by tracker, requiring a specific design of antireflection structure to reach angular tolerant property. And this specific design, sub-wavelength texture, is going to be introduced and simulated in the remaining chapters.

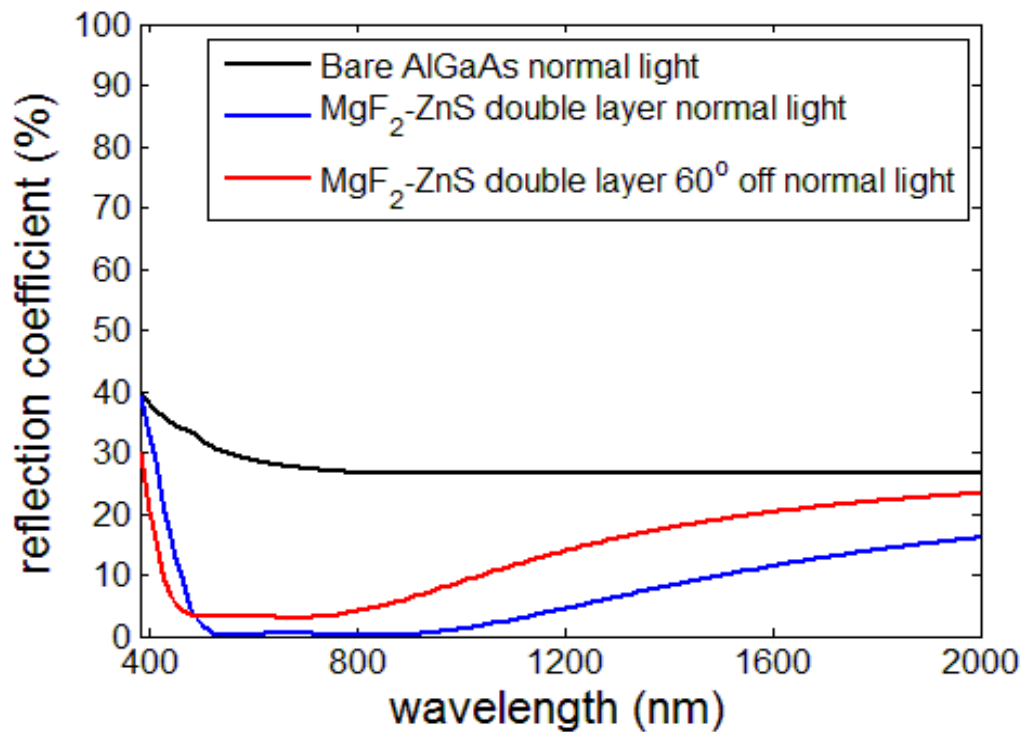


Fig 2.5.3 Reflectivity of AlGaAs substrate with/without ARC under normal light and with double-layer ARC for off-normal light

2.5.3 Current matching in multi-junction solar cells

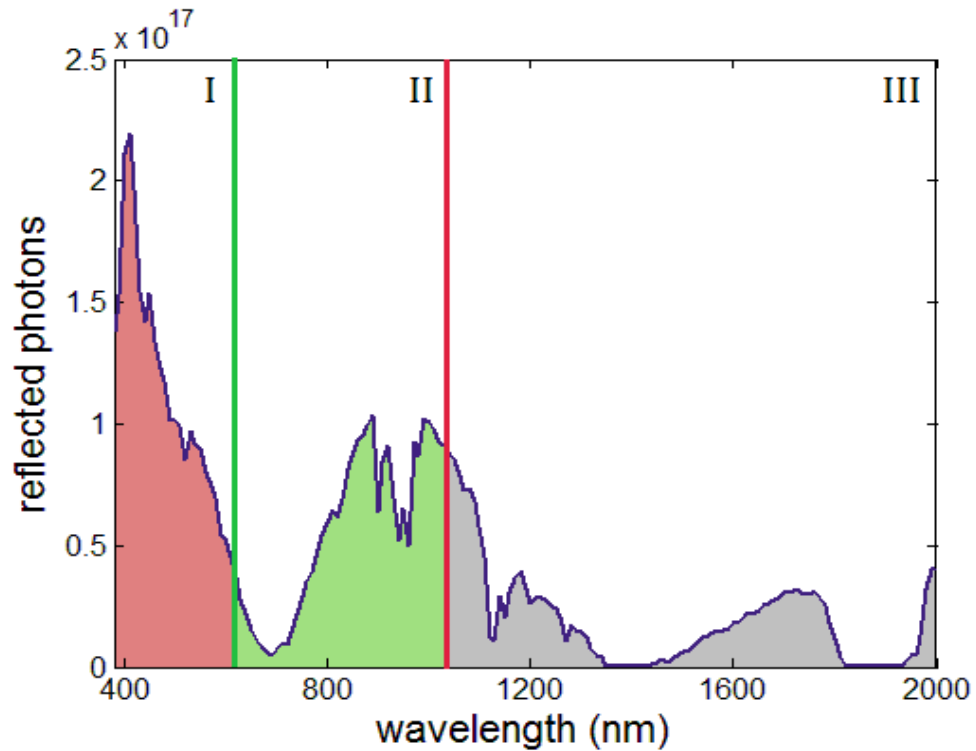


Fig 2.5.4 Number of photon-loss for optimized ZnS pyramid grating (colors indicate photon loss in different subcells)

Due to the solar cell mechanism, number of photons above the bandgap is more critical than amount of energy above the bandgap, so ARC design is to minimize photon loss in the spectrum of interest, such as integrated photon loss in Fig 2.5.2. In single-junction the photon-loss can be directly associated with the current loss. However, in multi-junction solar cell, all the subcells are connected in series, so current matching issue, limited by subcells with the largest photon loss, is a critical new problem compared with single-junction AR design. Under ideal conditions the total tandem current loss of a series connected device will roughly be set by subcells with the largest integrated photon-loss over responding working spectrum region. Fig. 2.5.4 illustrates an example of photon-

loss for a multi-junction, where the area of each subcell indicates the current loss, and the maximum area among all the subcells predicts the final current loss for the solar cell system. Current matching issue in each subcell requires that optimized AR structure could arrive at minimum photon loss among the maximum value of photon loss in various designs, which is the idea of texturing AR surface.

Based on current available experimental approaches to textured surface, which will be explained in chapter 3, and easy access to modeling, this work in chapter 5 is going to simulate and optimize periodic one-dimensional groove grating, two-dimensional hemisphere grating and two-dimensional pyramid grating. The design of AR texture depends on optimization of the materials, the surface morphology, and the geometric parameters could bring out minimum photon loss for specific multi-junction solar cell. In the literature, some approaches minimize the integrated photon loss multiplied by internal quantum efficiency (IQE) for a more accurate optimization. But the external quantum efficiency (EQE) is measured under zero external potential, which is not the real operating condition for solar cells. Here is no well-designed solar cell presenting stable IQE over the whole working spectrum without intense fluctuation ^[19], where IQE is derived from the relation $EQE(\lambda) = IQE(\lambda) * (1 - Reflectivity(\lambda)) * (1 - Shadow)$. Hence, this work did not take IQE into account for optimization. In the following chapters, chapter 3 will review what previous work has been done about AR in the literature, chapter 4 will introduce three main approaches to analyze light propagation rules, and chapter 5 will show the simulation results for various sub-wavelength antireflection gratings, based on a thin film model using the transfer matrix method.

Chapter 3 Antireflective Coating (ARC)

Generally the optimal index of refraction n for a single-layer ARC is given by the square root of the solar cell substrate and the medium through which light is propagating. The thickness of a single-layer ARC is determined by a quarter of the light's wavelength ($\lambda/4n$) in the ARC medium. Zero reflectivity can be achieved at this specific wavelength for normal incident light due to destructive interference. Since solar cells are working over a wide spectrum of wavelength, the optimized thickness would need careful design, which is usually done through simulation. But for obtaining a quick estimate, it can be roughly approximated by the quarter wavelength in the ARC medium where the spectrum presents the highest intensity. The wavelength at which the spectrum has the largest intensity is chosen as the point of zero reflectivity for choosing the right materials and thickness. For an AM 1.5G sunlight spectrum as shown in chapter 2, the center of maximum intensity is around 650 nm, which can be used as an optimization point. For example SiN, a common ARC material of silicon-based solar cells, has the average refractive index of 2; hence, the optimized SiN thickness would happen around 82 nm, which is consistent with an optimized thickness of 80 nm as shown in Fig 2.5.2.

Generally for a given material, the refractive index varies with the wavelength. This wavelength dependency is known as material dispersion relation, and is an intrinsic characteristic of the material. Thus for a given ARC thin film material system, a critical parameter to determine is the thickness of the individual layer, which can be predicted by minimizing the integrated energy or photon loss over a wide spectrum. In a black body spectrum or the realistic sunlight spectrum, the intensity ($\text{watt/m}^2/\text{nm}$) varies with the

wavelength; hence ‘light intensity weight’ (intensity per unit wavelength / total intensity) depends on the wavelength. The integrated energy loss is an integral of reflectivity and the light intensity weight over the whole working spectrum.

3.1 Traditional Single / Multi-layer Planar ARCs

The common single-layer ARC materials for Si solar cells are oxide or nitride materials, *e.g.* Si₃N₄, SiO₂, TiO₂, and Al₂O₃ [20,21,22]. Si₃N₄ is widely used in Si solar cells because, besides having a good AR property, it also acts as a good surface passivator, consequently increasing collection efficiency. SiO₂ is also used for Si solar cells, due to its passivation properties, but its lower refractive index makes it a marginal candidate for single-layer ARCs [23].

More complex ARC arrangements utilize two or more layers whose thickness optimization allows for lower reflectance losses than a single-layer ARC. Optimized single-layer AR coating reduce the reflectance loss for normal light to about 10%, whereas optimized double-layer AR coating can reduce reflectance to around 4% . Most commonly used material combinations for double-layer ARCs are MgF₂/ZnS [24,25], MgF₂/BN [26], MgF₂/ TiO₂ [27], and Al₂O₃/TiO₂ [28].

3.1.1 Optical design of multi-layer – choice of refractive indices

Generally, if the refractive index from the media where light propagates (air or cover glass) to the solar cell (semiconductor material), is increasing, then the reflection coefficient could be reduced. If refractive indices of the materials are at their optimal value, a larger number of layers in an ARC arrangement contributes to a lower average

reflectance ^[29]. For a single-layer antireflection coating, lowest reflection occurs when $n_{ARC} = (n_{sup}n_{sub})^{1/2}$, where n_{ARC} , n_{sup} , n_{sub} are referring to the refractive indices of the ARC layer, superstrate, and solar cell layer respectively. For a generalization to an M-layer coating, the refractive index of the m^{th} layer follows equation ^[30] (3.1.1)

$$n_m = n_{sup}^{\left(\frac{M+1-m}{M+1}\right)} n_{sub}^{\left(\frac{m}{M+1}\right)} \quad (3.1.1)$$

For multi-junction solar cells, to reduce the surface recombination velocity by surface passivation, n_{sub} would correspond to that of a high bandgap material, such as AlInP. Assuming the AlInP window layer to be the substrate medium, at a single wavelength of 650 nm, the optimized refractive indices and relative materials (from the refractive indices data of optional AR materials as shown in table 3.1.1) for various number of layers are shown in table 3.1.2^[30]. It should be noted that the practical use of these calculations is constrained by the dispersion properties of the materials over the wavelength range of interest; therefore the choice of material at a single wavelength provides only a starting point for investigating suitable material combinations for the ARC design.

MgF ₂	1.38(o) 1.39(e)	ZnS	2.55(o) 2.56(e)
Al ₂ O ₃	1.77	TiO ₂	2.49(o) 2.76(e)
SiO ₂	1.54(o) 1.55(e)	ZnO	1.98(o) 2.00(e)
MgO	1.73	Si ₃ N ₄	2.01
Ta ₂ O ₅	1.80	TeO ₂	2.25
CeO ₂	2.0	SiC	2.63(o) 2.67(e)

Table 3.1.1 Refractive indices of optional AR materials, characters ‘o’ and ‘e’ in parentheses refer to ordinary and extraordinary waves respectively

NO. of layers	Optimized refractive indices	Corresponding materials
1	1.775	Al ₂ O ₃
2	1.466, 2.149	SiO ₂ /Ta ₂ O ₅
3	1.332, 1.775, 2.364	MgF ₂ /Al ₂ O ₃ /ZnS
4	1.258, 1.582, 1.991, 2.504	MgF ₂ /C-SiO ₂ /Si ₃ N ₄ / TiO ₂
5	1.211, 1.466, 1.775, 2.149, 2.602	-----
6	1.178, 1.388, 1.635, 1.926, 2.270, 2.674	-----

Table 3.1.2 Optimal refractive indices and corresponding materials for ARCs with 1-6 layers on MJ solar cells with AlInP in air

In real materials, the polarization does not respond instantaneously to an applied field. This causes dielectric loss, which can be expressed by a permittivity that is both complex and frequency dependent. Real materials are not perfect insulators either, *i.e.*, they have a non-zero direct-current conductivity. Taking both aspects into consideration, a complex index of refraction can be defined: $N = n + i*k$. There are two terms. The real part ' n ' is a measure of the speed of light in that substance, that is expressed as a ratio of the speed of light in vacuum relative to that in the considered medium, and the imaginary part k , often referred to as the extinction coefficient, indicates the amount of absorption loss when the electromagnetic wave propagates through the material. The absorption coefficient $\alpha = 4\pi k / \lambda_0$ (the same as the physical parameter introduced in chapter 2.4.1, where the extinction coefficient k is derived from experimental data), can also be expressed in terms of basic physical properties^[13].

MgF ₂ ^[31]	10.8 eV	ZnS ^[32]	3.54 eV
Al ₂ O ₃	7~8 eV	TiO ₂ ^[33]	2.1~3 eV
SiO ₂	8.9 eV	ZnO	3.37 eV
MgO ^[34]	7.8 eV	Si ₃ N ₄ ^[35]	5.1 eV
Ta ₂ O ₅ ^[36]	4.5 eV	TeO ₂ ^[37]	3.4~3.7 eV
CeO ₂ ^[38]	3.6~4.1 eV	SiC	2.86 eV

Table 3.1.3 Bandgaps of commonly used AR materials

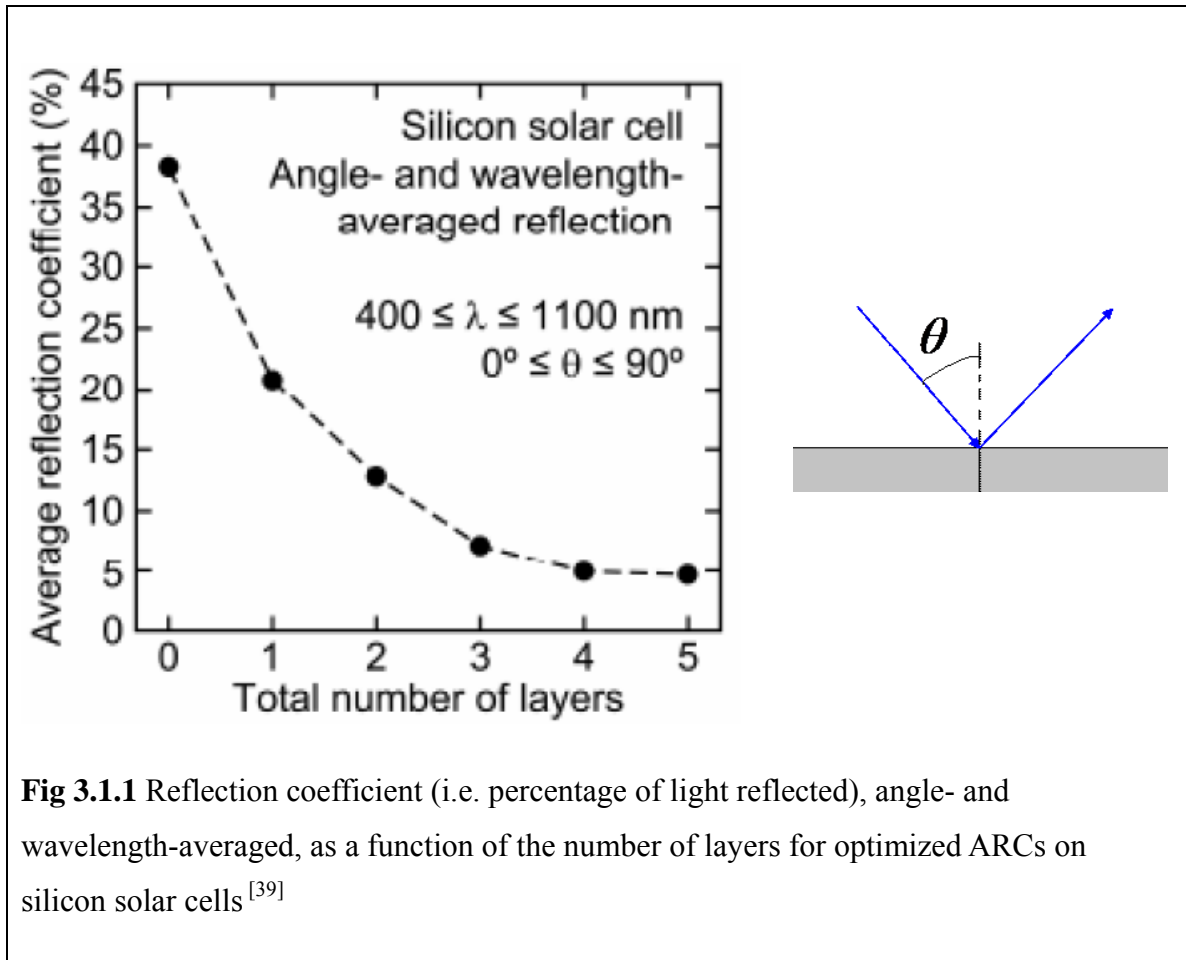
When taking into account the extinction coefficient into the expression for the refractive index, the absorption within the materials is naturally dealt with. Consequently, ideally the AR materials ought to be transparent to the whole working spectrum, possessing zero extinction/absorption coefficients in the solar cell working region. In other words, AR materials belong to high bandgap materials, transparent to the photons below the bandgap. The bandgaps of commonly used AR materials as mentioned in chapter 2 are presented in table 3.1.3

3.1.2 Optical design of multi-layers – thickness optimization

The optimization of minimizes integrated photon loss from 300-1800 *nm* under AM 1.5D for 3-junction lattice matched solar cell with AlInP top cell (substrate). There are several options to choose from, to achieve this optimization. Antireflection coatings of 1-4 layers were optimized using the materials recommended in Table 3.1.4.

Al_2O_3	70 <i>nm</i>
$\text{SiO}_2/\text{Ta}_2\text{O}_5$	55 <i>nm</i> / 41 <i>nm</i>
$\text{MgF}_2/\text{Al}_2\text{O}_3/\text{ZnS}$	70 <i>nm</i> / 17 <i>nm</i> / 38 <i>nm</i>
$\text{MgF}_2/\text{C-SiO}_2/\text{Si}_3\text{N}_4/\text{TiO}_2$	86 <i>nm</i> / 153 <i>nm</i> / 57 <i>nm</i> / 0 <i>nm</i>

Table 3.1.4 Thickness optimization of 1-4 layers AR design on AlInP substrate over 300-1800 *nm* under AM 1.5D spectrum {reference [32]}



For a multi-layer ARC of up to 5 or more layers, the selection of suitable materials becomes a challenge. In addition to being transmissive, chemically and mechanically stable, the layer must be able to be deposited in thin film form^[40]. Larger number of AR layers requires materials with lower refractive indices as front layers. Although some polymers can offer low refractive indices, they often degrade with UV exposure, or are damaged by high intensity light such as that used in concentrated photovoltaic (CPV) systems. MgF₂/Al₂O₃/ZnS coating is the best triple-layer design, slightly surpassing the best two-layer design using MgF₂/ZnS coating. However, at the same time, the slightly improved performance with additional layers does not offset for the added processing time and

complexity. As illustrated in Fig 3.1.1, the decrease in reflectance is usually minimal after two layers. Hence, given the reflectivity improvement due to an increase in the number of layers, and the challenge for practical fabrication, the double-layer is commonly implemented for ARC both in the laboratory and industry. Hence, this work compares textured ARC with conventional double-layer. Table 3.1.5 shows three sets of double-layer designs for AlInP and Si substrate solar cells^[11].

AlInP substrate for 300 <i>nm</i> – 1800 <i>nm</i>	Si substrate for 400 <i>nm</i> – 1200 <i>nm</i>
SiO ₂ /Ta ₂ O ₅ 55 <i>nm</i> / 42 <i>nm</i>	SiO ₂ /Ta ₂ O ₅ 78 <i>nm</i> / 64 <i>nm</i>
Al ₂ O ₃ /TiO ₂ 70 <i>nm</i> / 0 <i>nm</i>	Al ₂ O ₃ /TiO ₂ 88 <i>nm</i> / 44 <i>nm</i>
MgF ₂ /ZnS 82 <i>nm</i> / 44 <i>nm</i>	MgF ₂ /ZnS 115 <i>nm</i> / 67 <i>nm</i>

Table 3.1.5 Three sets of double-layer designs for AlInP and Si substrate solar cells with solar cell working spectrum 300 *nm*-1800 *nm* and 400 *nm*-1200 *nm* respectively

In Table 3.1.5, the optimization for Al₂O₃/TiO₂ shows zero thickness of TiO₂, because of the absorption of TiO₂ in UV regime. As a result, in a single-layer design is the only option, which gives worse AR performance than the other two layer designs. However, absorption character of TiO₂ is determined by its deposition, which retains it as an optional AR material candidate. Later grating designs also use TiO₂ as high index material. The remaining part of this chapter would mainly focus on experimental approaches to planar ARC and texturing AR designs. Simulation work and methods for high quality AR designs would be explained in chapter 4.

3.2 Experimental Approaches for Planar ARC

The antireflection (AR) coating used for solar cells to minimize optical reflection has been developed in three major types. The first group is the single-layer or multi-layer quarter-wavelength film stacks. Close to zero reflection over a certain spectral range over wide ranges of incident angles can be achieved by controlling the refractive index and the thickness of each individual layer in the multi-layer structure. The main challenges for this approach are the availability of materials with the right indices and good optical transparency, as well as the precise control of the film thickness. The second group is the graded index (GRIN) AR structures, where the refractive index of the structure changes gradually from the top to the bottom. The index profile can follow different mathematical functions, such as linear, cubic, or quintic. With a GRIN AR structure, extremely low reflection can be achieved over a broad spectral range for a wide range of incident angles, especially with the quintic index profile. The difficulty associated with the choice of materials for practical control of index profiles has prevented this structure from having a practical application. Sol-gel index dopant introduction has been reported^[41]. The third group is the textured surface AR structures. One of the most successful example is the anisotropic etching of single crystal Si (100) surface in a solution containing potassium hydroxide. However, the micro-scale surface texturing involves anisotropic etching of the Si substrate, which does not apply to amorphous or polycrystalline Si and thin film solar cells. Another successful example is the design with micro-scale SiO₂ particles on a Si substrate, which takes advantage of different etching rates to obtain Si moth-eye structure.

The planar antireflection coatings are generally grown by deposition techniques, such as

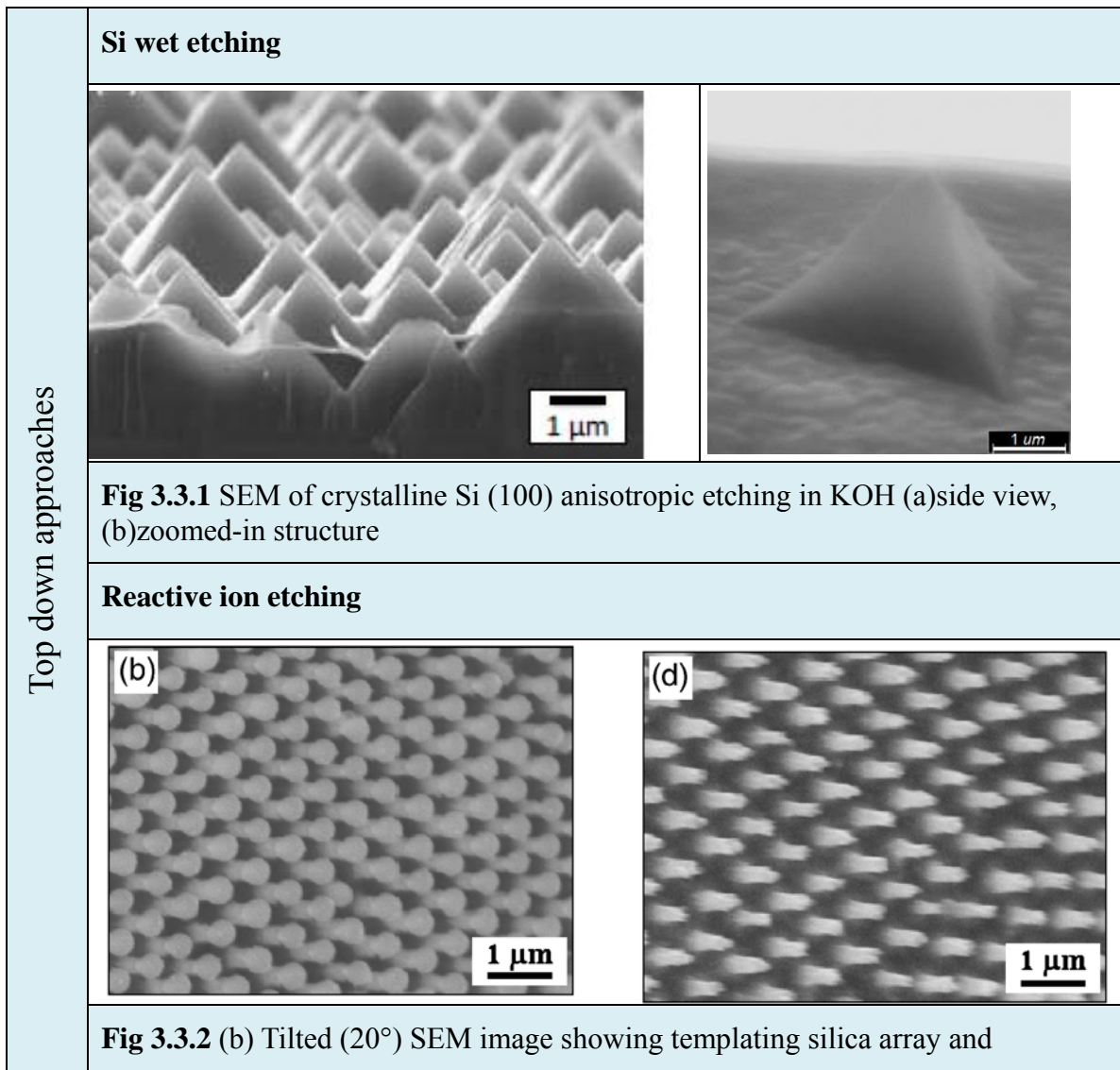
thermal deposition, sputter deposition, and plasma-enhanced chemical vapor deposition, which collect material vapor onto the substrate samples through various gasification approaches. Thermal deposition is done by gasifying the material, *i.e.* by heating materials of interest until they transfer into the gaseous state. The gas molecules will travel a certain distance until they deposit on the substrate. This process requires a vacuum environment to enlarge the mean free path of the gas molecules. These methods would be explained in detail in the Appendix.

As MgF_2 has a low refractive index (1.377 at 630 nm) and ZnS has a high refractive index (2.354 at 630 nm)^[42,43], and their high bandgap leads to transmittance in the ultraviolet region^[44], a combination of MgF_2 and ZnS is commonly used for double-layer ARC. As refractive index is dependent on the deposition method^[45], temperature^[46], porosity^[47] and stoichiometry^[48], *etc.*, optimal deposition conditions are critical in determining the required index. Radio frequency (Rf) magnetron sputtering technique can be applied to fabricate ZnS- MgF_2 composite films on GaAs substrates, obtaining an intermediate refractive index material for a middle layer in a 3-layer ARC, whose index can be obtained by experimental condition as desired between that of ZnS and MgF_2 . For example, by controlling the composition of these two materials, RF power applied to MgF_2 target was varied with a fixed RF power to the ZnS target in a co-sputtering deposition process^[49].

3.3 Experimental Approaches to Textured Surface

With a general overview about continuous grading of the refractive indices in order to reduce reflectivity, the next step is the fabrication of textured solar cells. These can be a

means to achieve continuous variation of the refractive index. Generally, the experimental methods to obtain texturing can be grouped into two categories, bottom-up or top-down. The bottom-up approach is the growth of coating or texturing starting from the substrate upwards; while the top-down approach is the fabrication of AR materials by selective removal from the original planar material, which is based on non-uniform etching rate between different materials or orientations. A few of the techniques used in the fabrication of textured ARCs are discussed below.



underneath silicon nipples etched by SF₆ RIE for 9 min. (d) Silicon nipples after 9 min HF etch. (ref [67] by C.H. Sun *et al.*)

Thermally dewetted nanotemplate

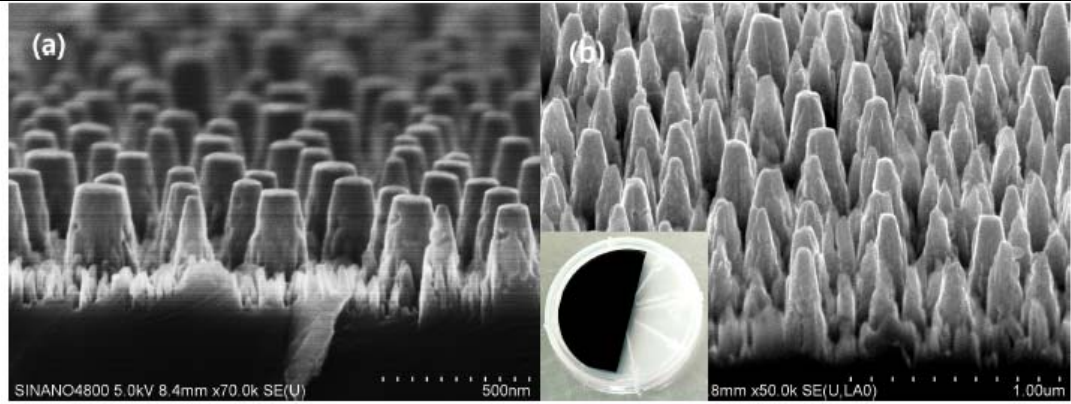


Fig 3.3.3 Al(Ga)InP sub-wavelength structure profile etched through the optimized recipe, but different time (a) $t = 3$ min; (b) $t = 5$ min. (ref [50] by R. Y. Zhang *et al.*)

Syringe like hydrothermal process

Button up approach

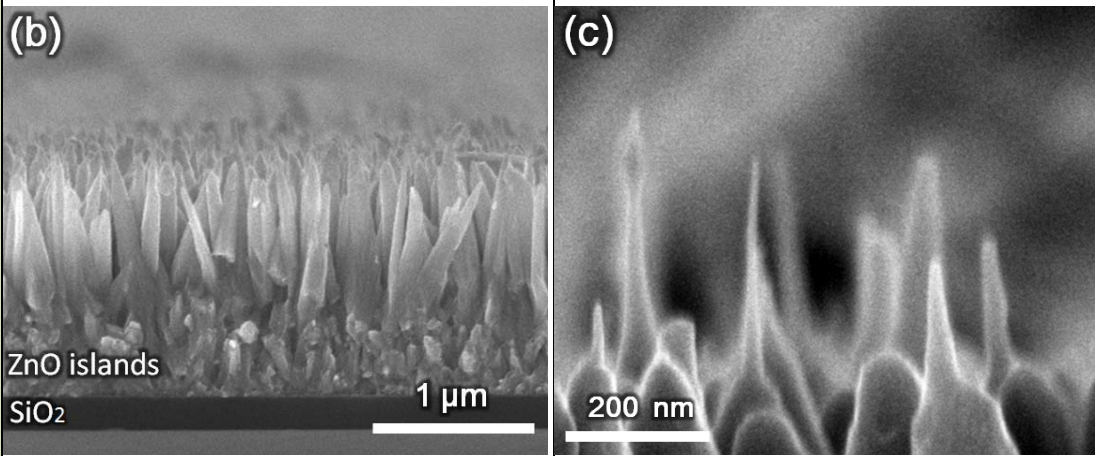


Fig 3.3.4 (b) Cross-sectional SEM images of the syringe-like ZnO NRAs. (c) The high-magnification image showing the ultras-small tips on the ZnO NRAs. (ref [51] by L.K. Yeh *et al.*)

Si anisotropic etching and reactive ion etching will be explained in detail in section 3.3.1

and 3.3.2 respectively. Thermally dewetted nanotemplate pattern, as shown in Fig 3.3.3, similarly uses masks to create textures. A 50 nm film of SiN is deposited on Al(Ga)InP to fabricate a low-surface-energy layer, so that the 10 nm Au film on SiN can agglomerate into nano-spheres during the high temperature heating process (500 °C, 100 s, in N₂ environment), which is the etching mask. In the end, Au and SiN residue masks are removed by a wet etchant. All in all, the key trick for top-down methods is using all kinds of techniques to manufacture masks by either internal intrinsic property or external materials.

Other top-down approaches have obtained nano-structures that mostly contain undesired surface defects which are unavoidable during the necessitated etching process^[52]. The induced surface defects act as recombination centers, which result in a large carrier loss in solar cells. Hence, most of the reported efficiency enhancements, achieved with the devices adopting the AR nano-structures, were fabricated through bottom-up approaches^[53,54]. Syringe-like ZnO NRAs, shown in Fig 3.3.4, were synthesized using one-step hydrothermal process. Before synthesis, a 200 nm SiO₂ passivation layer was deposited on the device by e-beam evaporation to prevent the potential shortage caused by the conductive ZnO. Subsequently, a ZnO seed layer was deposited by e-beam evaporation on SiO₂ for the subsequent growth of ZnO NRAs. The samples with ZnO seed layers were then placed downward, positioned at the bottom of the beaker, and heated to 95 °C for 3.5 hours in the aqueous solution containing zinc nitrate hexahydrate (10 mM) and ammonia. Finally, the syringe-like NRAs thus obtained were cleaned with ethanol and dried in air.

3.3.1 Si anisotropic etching

The concept of light trapping has been widely utilized in solar cell fabrication, especially for cells with a very high performance. Surfaces textured with upward and 'inverted' pyramids, and with V-shaped grooves have been used both to reduce reflection and to trap light internally within the cell. Surface texturing technique on Si has been popular since the mid-1970s^[55] and the most common way is wet chemical etching, using KOH^[56], which contributes to the formation of micro pyramids, due to the large difference in etching rate along various orientations. Taking Si as an example, the (110) plane is the fastest etching primary surface. The ideal (110) surface has a more corrugated atomic structure than the (100) and (111) primary surfaces. The (111) plane is an extremely slow etching plane that is tightly packed, has a single dangling-bond per atom, and is overall atomically flat^[57]. The strongly stepped and vicinal surfaces to the primary planes are typically fast etching surfaces. The effective parameters to impact etching rate contains solution concentration, temperature as well as etching time. Multi-crystalline silicon wafers can undergo anisotropic etching too, but random orientation of crystalline planes reduces the effectiveness of anisotropic etching. Multi-crystalline silicon is often etched in acidic solutions or through mechanical means like laser texturing or reactive ion etching (RIE)^[58].

For (100) silicon wafers with thermally grown oxide or nitride layer (around 200 - 300 nm), Mark Bachman^[59] *et al.* (Anisotropic silicon etch using KOH, INRF application note Process name: KOH01 1999) have reported a way to etch them using KOH. It is found that KOH wet-etch attacks silicon preferentially in the (100) plane, producing a characteristic anisotropic V-etch, with sidewalls that form a 54.7° angle with the surface

(35.3° from the normal). This etch process is independent of the doping concentration for As, P and SC.

The recipe for KOH wet-etch is provided in Appendix F.2.

3.3.2 RIE moth eye on Si substrate

Surfaces coated with a moth-eye structure of sub-wavelength roughness are known to show superior AR properties. Such a surface was first discovered on the cornea of night-flying moths by Bernhard in 1967^[60]. The eyes of this insect are covered with a regular array of conical protuberances (nipples) with a spacing ranging from 180 to 240 nm and height varying between 0 and 230 nm. The reflectance of their cornea was investigated in the wavelength range from 300 to 700 nm. Stavenga^[61] *et al.* investigated 19 butterfly species and showed that the nipple shape plays a rather significant role in the reduction of reflectance. They also probed that the nipple width plays a secondary role, whereas the nipple height is the crucial factor. Reflectance is reduced as the height increases. The first artificial moth-eye structure/film was produced by recording the interference patterns of low coherent laser beams on a photoresist. Currently, structures with a surface area of 0.5 m² can be produced by a complex holographic optical process or plasma treatment.

Chih-Hung Sun *et al.* reported a bioinspired templating technique for fabrication of broadband moth-eye ARCs on SC silicon substrates. The resulting sub-wavelength-structured ARCs exhibit superior broadband antireflective performance than commercial SiN_x coatings. The schematic illustration of the templating procedures for making wafer-scale silicon nipple arrays is shown in Fig 3.3.2. In summary, monolayer silica colloidal crystals with non-close-packed (ncp) structures are created by spin-coating. The ncp

silica particles can be used as the etching mask during a SF₆ reactive ion etching (RIE) process. By exposure to SF₆, arrays of nipple like structures are directly formed on silicon wafer (note, the etching selectivity between silicon and silica can be adjusted to more than 10:1). At last, remove silica nano particles on silicon substrate are removed by HF.

3.4 State-of-the-Art

The structure made by thermally de-wetted nanotemplate is shown in Fig 3.3.3. The measured reflection performance between 300-1500/2000 nm based on the optimized structure, *i.e.* the measured reflectivity at 8°, and at 45° off-normal angle, are compared with the RCWA simulation. The reflectivity of less than 5% over 200-1800 nm and a wide view up to 45° has been achieved in the optimized sub-wavelength structure (SWS).

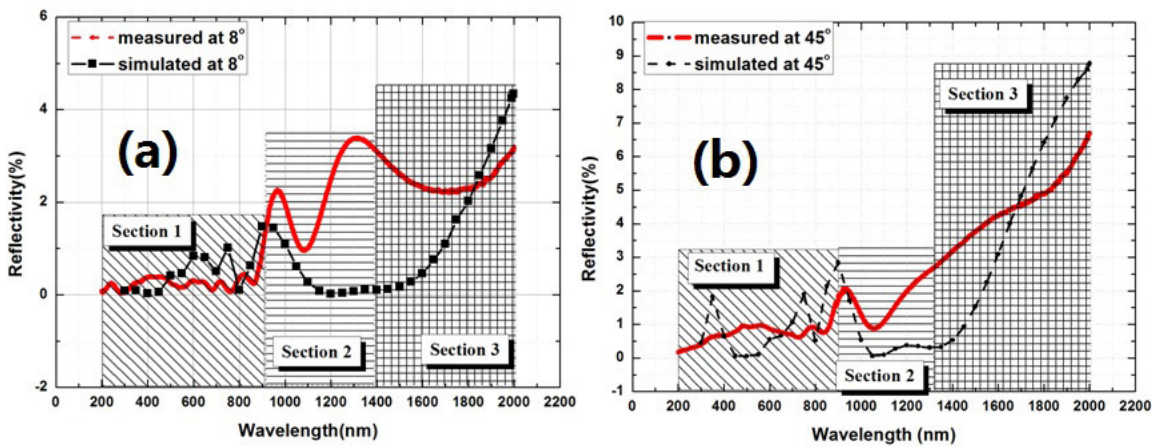


Fig 3.4.1 The measured and simulated reflection spectra comparison for Al(Ga)InP SWS as shown in Fig. 3.3.2(b); (a) incident angle is 8°, (b) incident angle is 45°.

Obviously, ARC must be carefully optimized to get the minimum photon loss regardless of the technique used. There are several simulation methods for planar films, such as the use of series Fresnel Equations, which describes interface between two media, or multi-

reflections between parallel-medium boundaries. Another technique is to use the transfer matrix method to deal with thin films, which explains how the electro-magnetic field transforms from the air to the substrate. For more complex structures with non-uniform morphologies, such as grating and texturing, the previous two methods cannot precisely predict the light behavior, which requires a more advanced approach. Rigorous coupled wave analysis (RCWA) is the rigorous way to discuss scattering and diffraction behavior between gratings, which could be used to find reflectivity. RCWA is a very advanced method, but demands a large amount of calculation. Most of the work based on RCWA is either confirming experimental results^[62] or analyzing textures^[63] with fixed parameters. Very little work is done that treats all parameters as variables and optimizes the proper texturing morphology or grating geometric parameters. Because this method to some extent is relatively hard to do self-coding, some companies have built up commercial software for RCWA, *e.g.* 'RSOFT'. But due to their high price (roughly \$10,000), it is not implementable for every laboratory. In chapter 4.3, it would be shown that the TFM could reach results similar to RCWA calculations in sub-wavelength scale simulation. The principle and equations of these three methods would be explained in detail in the next chapter.

As the efficiency of a solar cell is more dependent on the number of photons with energy above the bandgap, this work focused on the fraction of integrated reflected photons instead of on the reflectivity. The conventional dual-layer ARC, (usually MgF₂-ZnS), can have good antireflection properties for normal light, but it is not implementable for wide acceptance angle concentrators' application as shown in Fig 5.3 (iii). To this end, there

were a few options, such as SiO₂ and metallic^[64] nanoparticles plasmonic scattering, micro texturing, and sub-wavelength dielectric gratings. Sub-wavelength dielectric gratings demonstrated better suitable characters in III-V direct bandgap solar cells compared with the other two approaches, whose application is mainly in thin film solar cell devices. Their objective is to reduce the physical thickness of the photovoltaic absorber layers, and keep the optical thickness constant. Although silicon nano-tips and syringe-like Si nano-wire could get the reflectivity as low as 1% (as the structure in Fig 5.3 (i)), it is hindered for III-V multi-junction solar cells. Firstly, because the large area at the front surface would increase the recombination velocity, which would in turn increase surface recombination; secondly, due to wavelength-scale base of the structure, the scattering effect would enlarge the light path length, which leads to a challenge in optimizing the thickness of subcells; thirdly, because the micro-scale height of the texturing would increase absorption. Hence this work concentrated on the property of antireflection and angular tolerance for sub-wavelength dielectric grating on concentrated photovoltaic systems.

3.5 Classical Light Propagation in Thin Film with Finite Dimensionality

Photon has the property of wave-particle duality. Its wave property is of more interest when discussing reflectivity, because the coupling of the photon waves can contribute to constructive or destructive interference when the phase difference is even or odd times the time period for two propagating beams of light. In this section, traditional light propagation methods in thin films are discussed, including the formalization of the Fresnel Equations (Appendix C will derive electromagnetic field at the interface of two

media). The use of transfer matrix method is also described by solving light propagation inside each medium, followed by analysis of the rigorous coupled wave analysis (RCWA). The pros and cons of using the three methods are compared, and the transfer matrix method is demonstrated to be an effective method for multi-layer calculation. So this simulation is based on transfer matrix methods. In the end, it also proved that for planar AR coatings, thin film method-based transfer matrix approach presents a good match with experimental data.

Among various simulation models for reflection coefficient calculations, rigorous coupled-wave analysis (RCWA) and thin film model (TFM) are the most commonly used approaches. Transfer matrix method, which is also derived from Maxwell's Equations, handles the electric field in each layer as a 2*2 characteristic matrix, and the electric field in the deepest region can be transmitted from the incident field by the transformation of the elements in the characteristic matrix. Furthermore, RCWA and TFM are both based on Maxwell's Equations and generate almost identical results in the Si nipple array simulation [65]. Physical approximation in this work was the so-called thin film method, who considered all structures composed of a pile of homogeneous layers, with each layer possessing uniform optical properties. The approximated uniform homogeneous layers possess an effective refractive index between that of air and bulk AR material, depending on grating shape and the AR occupation ratio. There are three common ways to approximate effective index following the equation $n_{eff} = [n_1^q \cdot f_1 + n_2^q \cdot f_2]^{1/q}$, where $q = 1, 2, 2/3$. These three approximations use a linear average of refractive index ($q=1$), a linear average of permittivity [66] ($q=2$), and average of refractive index to the order of

$2/3^{[67]}(q=2/3)$. The difference in these approximations results in a coincidence in sub-wavelength height scale; neither would contribute to dissimilar optimization structures. The linear average of permittivity was chosen in this work.

As light is part of an electromagnetic wave, it always obeys Maxwell's Equations, which is the most general rule for electromagnetic waves. So with Maxwell's Equations along with specific boundary conditions, we can solve the electromagnetic field or potential in space, though analytic solutions could be difficult to achieve in many conditions, especially when the boundary has a complicated geometric shape. The analytic solution of a planar film is not a challenge, hence a good topic to start from. In this part, several traditional approaches to demonstrate light propagation are explained.

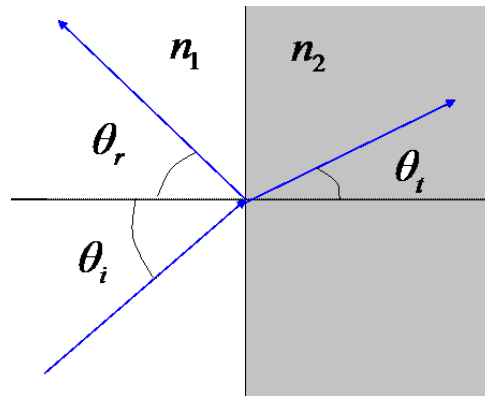


Fig 3.5.1 Notification of angles

To reduce the reflection coefficient, the first step is to know the optical characteristics and propagation properties of the material. The two important concepts with light propagation are reflection and refraction, which, when expressed as equations, are given by $\theta_i = \theta_r$ and $n_1 \sin \theta_i = n_2 \sin \theta_t$, as the symbols shown in Fig 3.5.1.(where the subscript i means incident, r means reflection, and t means transmission.)

We can get the relation of the electric field on both sides of the interface from the Maxwell Equations. Assuming the amplitude of the electric field for incident light, reflected light, and diffracted light to be A_i , A_r , and A_t respectively, the reflection

coefficient is $\left| \frac{A_r}{A_i} \right|^2$, which shows how much energy is lost per unit energy.

3.5.1 Light propagation at the boundary from Fresnel Equation

So from Maxwell's Equations, we can conclude that:

- The propagation vectors of incident light, reflected light and transmitted light are in the same plane.
- Incident angle and reflected angle are the same.
- The ratio of the sine value between incident angle and refraction angle is proportional to the ratio of refractive indices.
- The oscillation amplitude relation among incident wave, reflection wave and refraction wave obeys Fresnel's Equations (C.6) and (C.7) in appendix C.

To express the final equation using initial conditions, the reflection coefficient for both *TE* mode and *TM* mode (or say *S* polarization and *P* polarization) is in the form of the formula (3.5.1).

$$R_s = \left(\frac{n_1 \cos \theta_i - n_2 \cos \theta_t}{n_1 \cos \theta_i + n_2 \cos \theta_t} \right)^2 = \left[\frac{n_1 \cos \theta_i - n_2 \sqrt{1 - \left(\frac{n_1 \sin \theta_i}{n_2} \right)^2}}{n_1 \cos \theta_i + n_2 \sqrt{1 - \left(\frac{n_1 \sin \theta_i}{n_2} \right)^2}} \right]^2 \quad (3.5.1)$$

$$R_p = \left(\frac{n_1 \cos \theta_i - n_2 \cos \theta_t}{n_1 \cos \theta_i + n_2 \cos \theta_t} \right)^2 = \left[\frac{n_1 \sqrt{1 - \left(\frac{n_1 \sin \theta_i}{n_2} \right)^2} - n_2 \cos \theta_t}{n_1 \sqrt{1 - \left(\frac{n_1 \sin \theta_i}{n_2} \right)^2} + n_2 \cos \theta_t} \right]^2$$

Because sunlight is neither linearly polarized nor circularly polarized, half of it is *S* mode and the other half is *P* mode.

From the derivation of Fresnel's Equations from Maxwell's Equations, we can see that the Fresnel Equation are solving for the effect at the interface. However, due to multiple reflections, we can use Fresnel Equations to get the electromagnetic wave at each interface one by one, with the final electromagnetic field being the sum of the respective vector series. Consequently, even if the structure changes from single-layer to multi-layer form, the series could become tedious.

3.5.2 Light propagation in the medium expressed in matrix form

In contrast to the Fresnel Equations, whose aim was to describe the behavior of light when moving between media of differing refractive indices and the focus is only on the interface; transfer matrix is a method to treat each layer as a matrix, including both the interface and the propagation within this medium with its thickness. This method already takes the multiple reflections into account.

3.5.2.1 Light propagation in a pile of thin homogeneous films

For more complicated cases, if light propagates in a stratified media, we can treat the structure layer by layer. Consider two adjacent stratified media as an example: the first layer extending from $z = 0$ to $z = z_1$, and the second from $z = z_1$ to $z = z_2$. If $M_1(z)$ and $M_2(z)$ are the characteristic matrices of the two media individually, then

$$Q_0 = M_1(z_1)Q(z_1), \quad Q = M_2(z_2 - z_1)Q(z_2), \quad \text{So that} \quad Q_0 = M(z_2)Q(z_2), \quad \text{where} \\ M(z_2) = M_1(z_1)M_2(z_2 - z_1).$$

This result may immediately be generalized to the case of a succession of stratified media extending from $0 \leq z \leq z_1, z_1 \leq z \leq z_2, \dots, z_{mm-1} \leq z \leq z_{mm}$. If the characteristic matrices are M_1, M_2, \dots, M_{mm} , then

$$\left. \begin{aligned} Q_0 &= M(z_{mm})Q(z_{mm}), \\ \text{where,} \\ M(z_{mm}) &= M_1(z_1)M_2(z_2 - z_1) \dots M_{mm}(z_{mm} - z_{mm-1}) \end{aligned} \right\} \quad (3.5.2)$$

If there are mm media, where the first media is ambient, and the mm^{th} media is substrate, so from the second to $mm-1^{\text{th}}$ layer, denoting by h_j the thickness of each film (j varies from 2 to $mm-1$), the characteristic matrix of this pile of media (which is derived from Maxwell Equations in appendix C) is expressed as

$$M = M(\beta_2) \cdot (\beta_3) \cdot \dots \cdot (\beta_{mm-1}) = \prod_{j=2}^{mm-1} \begin{pmatrix} \cos \beta_j & -\frac{i}{p_j} \sin \beta_j \\ -ip_j \sin \beta_j & \cos \beta_j \end{pmatrix} = \begin{pmatrix} m_{11} & m_{12} \\ m_{21} & m_{22} \end{pmatrix} \quad (3.5.3)$$

$$\text{where, } \beta_j = \frac{2\pi}{\lambda_0} n_j h_j \cos \theta_j \quad (3.5.4)$$

Regard the medium as consisting of a very large number of thin films of thicknesses $\delta z_1, \delta z_2, \delta z_3, \dots, \delta z_{mm}$. If the maximum thickness is sufficiently small, it is permissible to regard ε, μ and n to be constant throughout each film.

3.5.2.2 The reflectivity and transmission coefficients from transfer matrix method

Consider a plane wave incident upon a stratified medium that extends from $z = 0$ to $z = z_l$, and that is bounded on each side by a homogeneous, semi-infinite medium. We shall derive expressions for the amplitudes and intensities of the reflected and transmitted waves.

Let A, R and T denote the amplitudes (possibly complex) of the electric vectors of the incident, reflected and transmitted waves. From appendix C (D.45) the ratios of amplitudes of magnetic (not the electric vectors) of the film are obtained:

$$r = \frac{R}{A} = \frac{(m_{11} + m_{12}p_l)p_1 - (m_{21} + m_{22}p_l)}{(m_{11} + m_{12}p_l)p_1 + (m_{21} + m_{22}p_l)} \quad (3.5.5)$$

$$t = \frac{T}{A} = \frac{2p_1}{(m_{11} + m_{12}p_l)p_1 + (m_{21} + m_{22}p_l)} \quad (3.5.6)$$

where, $p_j = \sqrt{\frac{\varepsilon_j}{\mu_j}} \cos \theta_j$, (3.5.7)

m_{ij} is the elements of the characteristic matrix of the medium, evaluated for $z = z_{mm}$.

In terms of r and t , the reflectivity and transmittivity are

$$\mathfrak{R} = |r|^2, \quad \mathfrak{T} = \frac{p_t}{p_1} |t|^2 \quad (3.5.8)$$

The corresponding formulae for a *TM* wave are immediately obtained from (3.5.5)-(3.5.6) on replacing the quantities p_j (subscript j refers to layers' order) by

$$q_j = \sqrt{\frac{\mu_j}{\epsilon_j}} \cos \theta_j, \quad (3.5.9)$$

The properties of a homogeneous dielectric film situated between two homogeneous media are of particular interest for us, and we shall, therefore, study this case more fully. We assume all the media to be nonmagnetic ($\mu = 1$).

From (3.5.3), it can be seen that this characteristic matrix is only related to the incident angle and the properties of each layer between ambient and substrate. Apparently, the reflection coefficient should relate to the materials on the two sides of the coating, and they are presented in the initial state Q_0 and final state Q as shown in (3.5.2), and it is shown in the parameter r , where the p (or q) for the two sides are included.

Furthermore, for some materials, such as anisotropic crystals of calcite or boron nitride *etc.*, one can distinguish ordinary and extraordinary waves, which are due to different refractive indices for the two polarizations. It is called birefringence, or double refraction. In this case, in the expression of p and q , the refractive index n is of a different value even in the same medium.

By the way, this method is suitable for complex refractive index, replacing n by $N = n + ik$. When changing the refractive index from a real number to a complex number, the

absorption is automatically taken into account[†].

3.5.3 Diffraction and reflection explanation from rigorous coupled-wave analysis (RCWA)

Rigorous coupled-wave analysis (RCWA), which analyses diffraction properties, was first brought out by T.K Gaylord in 1981^[68,69]. 'Rigorous' comes from the improvement in 'coupled-wave approach' for three approximations ^[70, 71], which are 1) neglecting boundary diffraction, 2) neglecting the second derivatives of the field amplitudes, and 3) retaining only one diffracted wave (beside the transmitted wave). Among rigorous methods for grating diffractions can be grouped into two categories: integral methods and differential methods ^[72], applied to continuous profiles and discrete-level profiles respectively. RCWA belongs to differential methods. Among differential methods, they can be grouped into two categories: treating the permittivity transition in the grating region explicitly or using a Fourier expansion of the permittivity. RCWA uses Fourier expansion to represent the transition in permittivity and electric field. So the expression of converting space into reciprocal space theoretically should contain an infinite number of terms for exact solution.

As this method was developed, it was found that it can also be used for calculating reflection coefficient under certain conditions, so RCWA is currently being used for calculating reflectivity.

3.5.4 Pros and cons for traditional methods

From the discussion in chapter 3.1, we can claim that with respect to the application to a

[†] If we ignored absorption, $R+T=1$, When taking absorption into account, $A+R+T=1$. Here we say when changing the refractive index from real number to complex number, the absorption is automatically taken into account, because absorption and reflection are not independent.

planar film calculation, all these three methods could lead to exactly the same solution. The transfer matrix method will be applied to antireflection coating for reflectivity as an example. Here, I will compare these methods and conclude their pros and cons when applied for reflectivity calculation.

3.5.4.1 Pros and cons of Fresnel Equation method

Fresnel Equation method is the most straightforward method to know light's action at a planar boundary, which can easily give a prediction of how much energy will be lost, by two equations in (3.5.1). We shall consider the action at interface from these two equations to be of the first order. If it is applied to a single-layer, *i.e.* a sandwich structure of three media and two interfaces, the action of light at each interface must be analyzed. Since the light will never stop propagating backward and forward in the central medium, the final reflection coefficient is a sum of a series of beams that are reflected backward. The series, coming from a collection of orders, is a geometric progression, because the first order reflectivity at these two interfaces is a fixed value. Taking the progression to be infinitely large, we can get the exact solution of reflection coefficients for a single-layer.

However, to get the exact solution for multi-layer would be tedious, due to complicated actions going forward and backward, and it is not easily apparent even for double or triple layers. Nevertheless, a rough estimation can be quickly obtained because the amplitude shrinks fast as the order increases.

3.5.4.2 Pros and cons of the transfer matrix method

The transfer matrix method is also derived from Maxwell's Equation, however it deals

with the electric field in each layer instead of at the interface, where each layer is presented as a 2*2 characteristic matrix, and the final reflection coefficient depends on the elements in a characteristic matrix. Because the composition of vectors of forward and backward electric waves constitutes the final electric field, multiple reflections in every layer are automatically taken into account. We should notice that the transfer matrix method requires the medium to be a homogeneous dielectric film, or a stratified medium that can be treated as a series of homogeneous dielectric films. So, strictly speaking, it cannot solve non-planar morphology or an anisotropic medium, unless the non-planar medium could be approximated as multi-layer structure and each layer has an effective dielectric characteristic. Nevertheless, this approximation leads to another problem that the shape and period of texture would not influence the effective permittivity, which will be discussed in detail in Chapter 4.1.

3.5.4.3 Pros and cons of the RCWA method

RCWA uses a Fourier expansion to represent the transition in permittivity and the field in each region, which leads to higher order linear equations. The limitations of RCWA include the difficulty of convergence – a large number of spatial harmonics (orders) must be retained in the analysis to obtain accurate results. The more terms to keep, the more accurate results we can obtain, but the large number of terms results in heavy calculation. At the same time, having insufficient number of terms contributes to a non-conserved energy, and hence a significant error.

For instance, there are four extreme examples that need a large number of orders and points to be evaluated; first, a conducting grating illuminated with a transverse-magnetic-

(*TM*-) polarized wave; second, a pulse-width-modulated grating^[73,74,75], whose period is usually much larger than the wavelength and each grating period is composed of grooves with sub-wavelength size features; third, crossed-grating structures, in which a few orders are retained along each direction; and fourth, the two-dimensional (2D) mesh of spatial harmonics^Y. Besides the large amount of calculation of the physical properties, there are also some factors from mathematics. To find all the eigenvalues and eigenvectors of an $n*n$ matrix, it requires the computation time roughly to the order of n^3 , and it is practically very important to reduce computation time in those applications requiring accurate computation.

So we can see that RCWA is an advanced method that can deal with anisotropic media, and it can solve both reflection and diffraction, however it requires higher orders in the analysis to get an accurate result. TMM (transfer matrix method) could solve this problem, which treats the grating region as many uniform thin films, with an effective permittivity as a single value instead of a Fourier expansion. The physical origin of the transfer matrix method is also from Maxwell's Equations, but it handles the electric field in each layer as a 2*2 characteristic matrix, and the electric field in the deepest region can be transmitted from the incident field by the transformation of the elements in the characteristic matrix. Because the composition of the vectors of forward and backward electric waves determines the final electric field, the multiple reflections in every layer

^Y As the Fourier transform of permittivity is shown among each order's equations, the 1D texture is transformed as

$$\varepsilon(x) = \sum_h^H \varepsilon_h \exp(ihKx), \text{ assume retain } H \text{ terms, then the 2D texture is transformed as}$$

$$\varepsilon(x, y) = \sum_h^H \sum_h^T \varepsilon_{ht} \exp(ihK_x x) \exp(ihK_y y) \text{ should retain } H*T \text{ terms.}$$

are automatically taken into account. Nevertheless, this approximation leads to another problem; that the shape and period of texture would not influence the effective permittivity, which will be discussed in detail in modeling section. Furthermore, RCWA and TFM are all based on Maxwell's Equations and generate almost identical results in the Si nipple array simulation^[76]. A thin film model based on the transfer matrix method would be used in later simulation and optimization subsequently.

3.6 Application of Transfer Matrix Method for Multi-layer ARC and Comparison with Experimental Data

One of the most widely used material set for a double-layer of ARC is MgF₂-ZnS. Based on the transfer matrix explained before, we can obtain how the reflections will vary with their thicknesses. We shall use the model spectrum of black body radiation ($T = 5800\text{ K}$), and take the dispersion for MgF₂-ZnS and C-Si (100) into account as shown in Fig 3.6.1 and Fig 3.6.2.

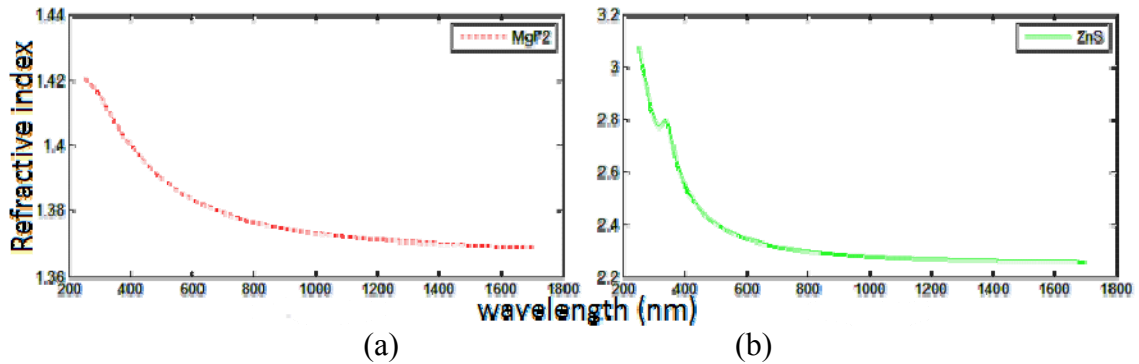


Fig 3.6.1 (a) Dispersion relation of MgF₂, (b) Dispersion relation of MgF₂ refractive index versus wavelength

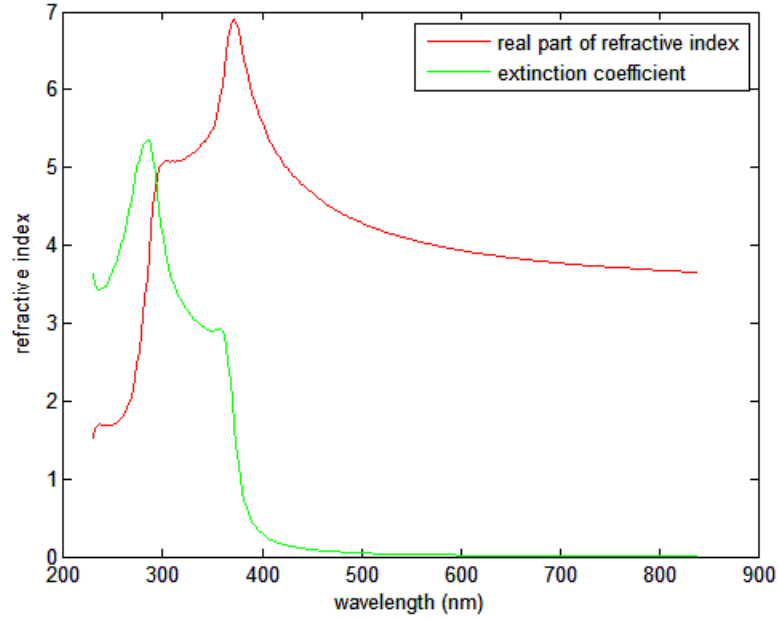


Fig 3.6.2 Dispersion relation of C-Silicon (100), refractive index (both the real part and imagine part) versus wavelength

Here, the database for C-Si (100) has been limited to 840 *nm*. From 4.5.2 we can see that as the wavelength increases after 500 *nm*, its refractive index slope is relatively gentle, hence it is not a bad assumption to consider the refractive index as a constant beyond 840 *nm*.

Using the transfer matrix method and the corresponding parameters, we can point out the reflectivity and optimize the double-layer coating. As shown in Fig 3.6.3 below, the modeling is done assuming AM 1, with wavelength from 380 *nm* to 1100 *nm*[†], the intensity of each wavelength being based on a black body spectrum at 5800 *K*, and taking

[†] Because of the band gap of all the relevant materials, $E_{g-MgF_2} = 10.8eV$ (corresponding to 115 *nm*), $E_{g-ZnS} = 3.91eV$ (corresponding to 317 *nm*), $E_{g-Si} = 1.1eV$ (corresponding to 1127 *nm*), we choose the wavelength from 380 to 1100 *nm* for modeling.

into account the dispersion of both C-Si (100) and MgF₂-ZnS layer. We can see that the reflection fluctuates immensely with the thickness of both layers when the thickness is in the region below 200 nm. And the minimum reflection 3.2746 % happens at a thickness- MgF₂ = 100 nm, thickness-ZnS = 54 nm.

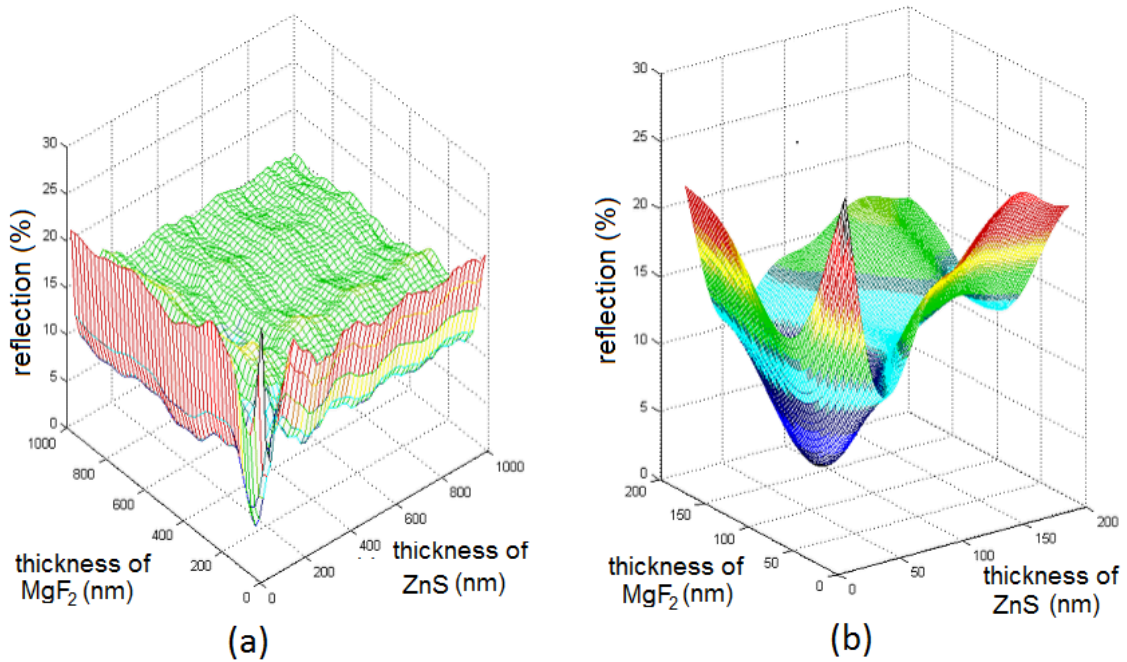


Fig 3.6.3 Normal incident light, where MgF₂-ZnS are coated on C-Si (100) substrate, using black body radiation at 5800 K. (a) at a larger thickness scale (20 nm to 1000 nm), (b) at a smaller thickness scale (20 nm to 200 nm)

Relative to the thickness which corresponds to the minimum reflection for normal light, its angular and wavelength dependence can be seen.

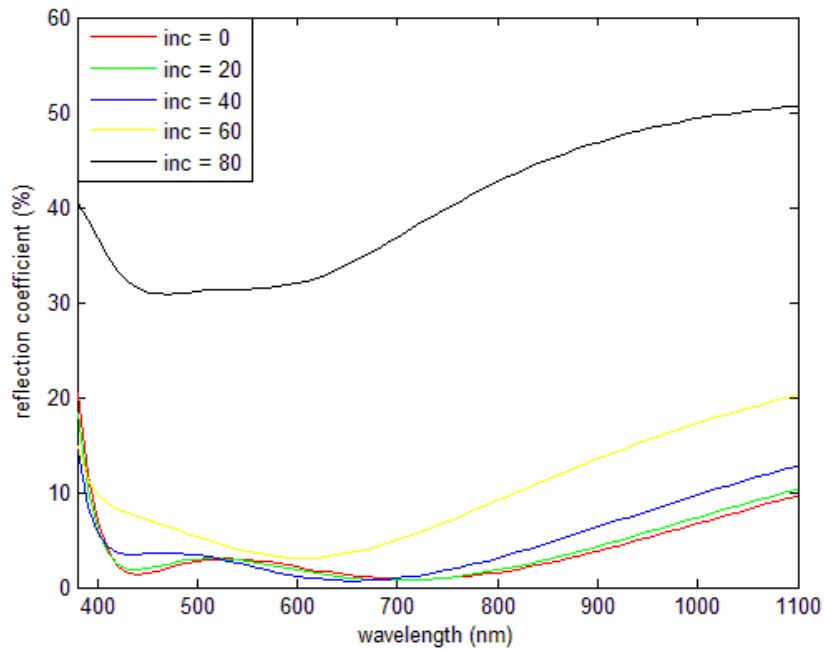


Fig 3.6.4 Angular dependence of incident angle for MgF₂-ZnS double-layer on c-Si(100) at AM 1 optimized thickness [100 nm, 54 nm]

Due to the fact that the sunlight has its maximum intensity when it comes normal to the earth (incident angle = 0°), and with the angle increasing till 90° its intensity decreases, to maximize the efficiency, we should choose the thickness of each layer optimized at AM 1. With this we can observe how the solar cell's efficiency varies in a whole day. As shown in Fig 3.6.4, it can be said that with the incident angle increasing, the reflection would increase, however, with the incident angle smaller than 60°, this increase is not obvious, and above 60°, the reflection coefficient is highly enlarged. Again, the two explicit troughs become vague as the angle increases.

For a clearer comparison between this simulation result and experimental data, Fig 3.6.5 used the same parameters as those used in literature, drawn to the same scales. Both

optimize MgF_2 -ZnS dual-layers on a GaAs substrate under AM 1.5 G spectra over 300-1500 nm region.

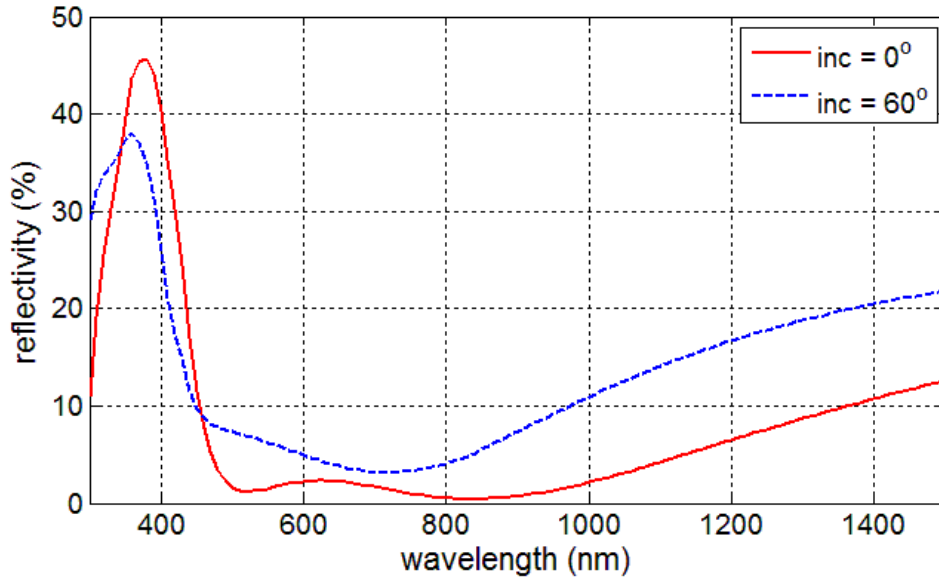


Fig 3.6.5 Calculated reflectivity of optimized MgF_2 (115 nm) ZnS (66 nm) dual AR on GaAs for spectrum 300 nm ~1500 nm for various incidence angles

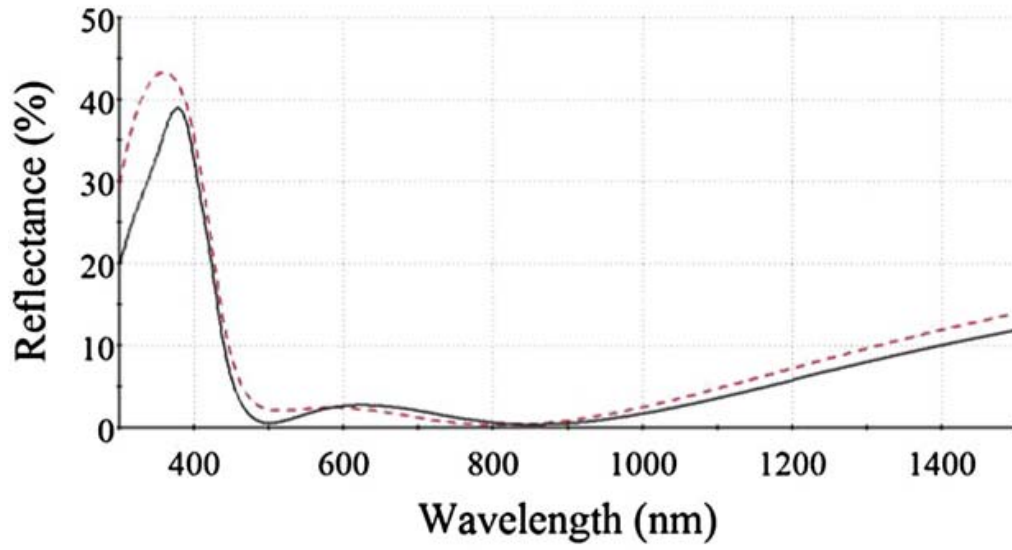


Fig 3.6.6 Measured (solid line) and simulated (dash line) reflectance spectra of GaAs substrate with MgF_2 -ZnS double-layer

Comparing this simulation work (red line in Fig 3.6.5) with the experimental result (solid line in Fig 3.6.6) in literature ^[77] under the same optimization conditions (MgF₂-ZnS double-layer, over 300-1500 nm spectrum, on GaAs substrate, under normal light,) the transfer matrix method shows a good match with experimental measurements. Fig 3.6.5 also demonstrates that off-normal incident light would degrade antireflection property for photon harvest.

In Steven Wojtczuk and coworkers' concentrator cells work ^[78], they use 130 nm MgF₂ and 66 nm ZnS on Ga_{0.65}In_{0.35}P over the spectrum 300 nm -1400 nm, which shows a confidence of transfer matrix's optimization validity.

3.7 Conclusion

Based on the derivation of light propagation by traditional methods, we can conclude that the transfer matrix method is a relatively easy way for the modeling of homogeneous dielectric film. In case of a condition that a texture can be treated as a stratified medium, neglecting its morphology, the transfer matrix method provides a fast and straightforward solution. And in the next chapter, some results from the literature will be highlighted that identify that the critical factors for texturing surface among various morphology parameters, with regard to the reflection coefficient, is the depth, and not the other geometric characteristics. Hence I shall choose transfer matrix method for further simulation.

According to the application of transfer matrix method to multi-layer ARC, one can see that the conventional dual layer ARC, (*i.e.* MgF₂-ZnS), may be designed to have a good

antireflection properties for a finite sunlight incidence angle (*i.e.* normal incident light) but it generally shows poor AR properties for wide-acceptance-angle concentrators' application as shown in Fig 3.6.5 (especially when the incident angle is larger than 40°). To overcome the limitation of planar ARC, several alternate approaches have been attempted in the literature, including the use of dielectric or metallic nanoparticles (plasmonic scattering) ^[79], micro texturing ^[80], and sub-wavelength dielectric gratings. Among these approaches, the application of sub-wavelength dielectric gratings has shown promising results ^[81]. Hence the goal in the next chapter is to obtain omnidirection (for all directions) antireflective sub-wavelength textures.

Chapter 4 Simulating Dielectric Material of Sub-wavelength Periodic Antireflection Texture

In this chapter, the property of periodic antireflection texture will be discussed. Assuming the period is larger than a quarter of the wavelength, the incident light will couple with the reflected light; so the effect of multi-reflection between periodic structures cannot be ignored. In order to apply transfer matrix to simulation, the period needs to be retrained within sub-wavelength scale, or more precisely, smaller than a quarter of incident wavelength. Furthermore, recent experiments for textured surface, which were discussed in chapter 3, are mainly applied to sub-wavelength scale. In order to apply this optical method, the applied material should be a dielectric, which will let light propagate through.

As the efficiency of solar cell is more dependent on the number of photons with energy above the bandgap, we focus on the fraction of integrated reflected photons instead of reflectivity. The conventional duo-layer ARC, (usually $\text{MgF}_2\text{-ZnS}$), can show good antireflection property for normal light, but it is not implementable for wide acceptance angle concentrators' application, as shown in Fig 4.3(iii). Although silicon nanotips^[82] and syringe-like Si nano-wires^[83] could get reflectivity as low as 1% (as the structure in Fig 4.3 (i) shows), it is hindered for III-V multi-junction solar cells. Hence, we focus on the property of antireflection and angular tolerance for sub-wavelength dielectric grating on concentrated photovoltaic systems.

Fig 4.1 shows, the green colored part is the antireflection material which is fabricated on gray colored solar cell substrate, so the textured surface makes the refractive index vary slowly from air to the dielectric antireflection material.

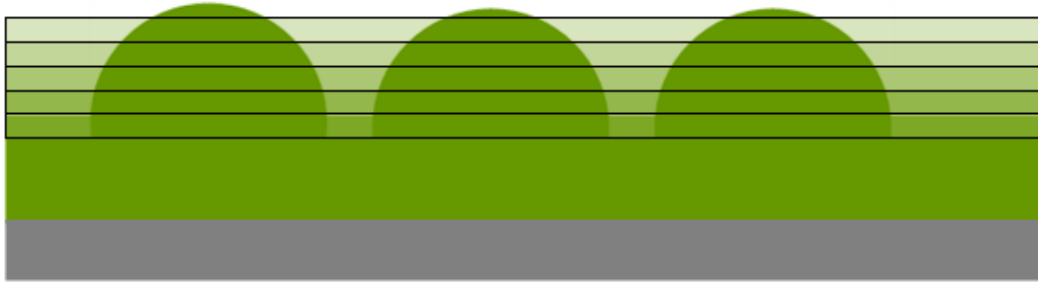


Fig 4.1 An example of textured surface that refractive index varies from air to antireflection material

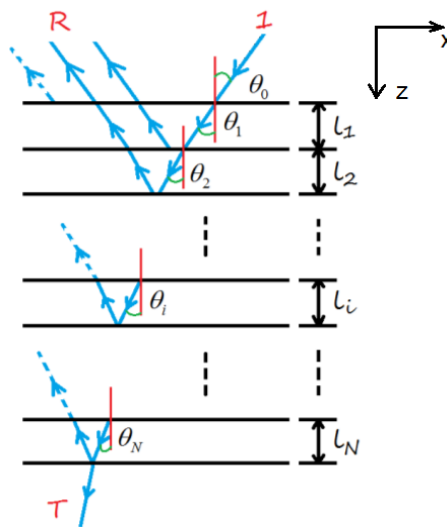


Fig 4.2 Schematic of light propagation among a stack of thin homogeneous films

In thin film approximation, several assumptions had to be made. First, the texture must be low profile so that each layer can be considered to be uniform; second, the material ought to be dielectric material. In optimization results, it will be shown that the optimized geometric parameters of the grating are really in the sub-wavelength scale. Hence, it demonstrates that our assumptions are consistent with the results. Here, we have taken into account of experimental absorption coefficient for both solar cell substrates and their AR materials. The absorption of solar cell substrate can produce electron-hole pair, but

the absorption in AR material would result in loss of energy; so the chosen AR material should have low or even zero absorption in solar cells' working spectrum.

As shown in chapter 4.2, the textured surface can be dealt as a pile of homogeneous thin films, in order to find the reflectivity as well as the photon-loss. As Fig 4.2 shows, each layer behaves as a matrix, which transfers the light by a function derived from Maxwell equations. The characteristic matrix is related to the thickness, the refractive index of the layer, and the angle of light within this layer. When the extinction coefficient is taken into account, the absorption is automatically taken into account.

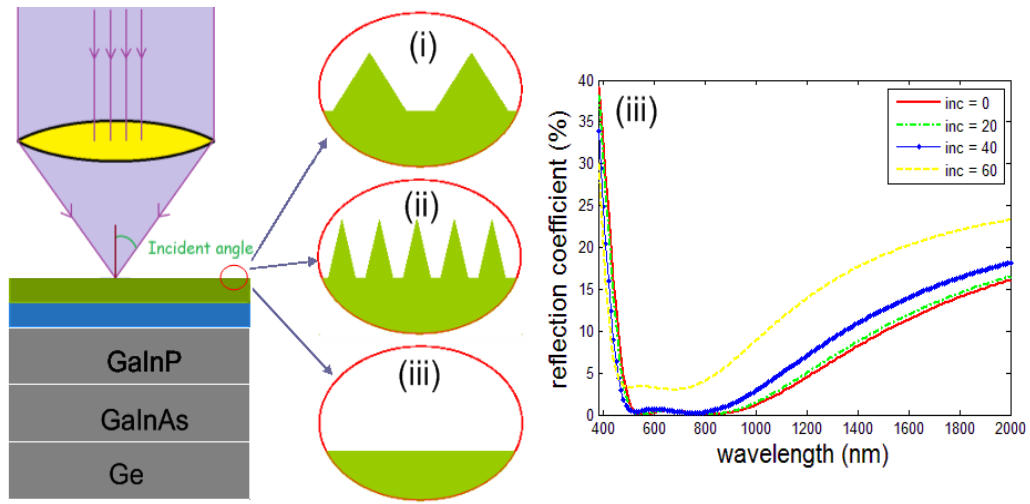


Fig 4.3 Concentrated III-V solar cell structure with ARC, and conventional ARC's angular tolerance property (i) micro scale textured surface, (ii) sub-wavelength scale dielectric gratings, (iii) reflectivity of MgF_2 -ZnS dual AR

4.1 1D Binary with Rectangular Cross Section

The simplest case of textured surface is 1D rectangular binary grating, which is shown in Fig 4.1.1. For single-layer and grating, there is only one material above the substrates. However, it plays a role of two layers, with 4 degrees of freedom to control, d_1 , d_2 , T , and

f , which refer to the thickness of groove, the thickness of flat layer, the grating period, and the ratio of ridge, respectively, as shown in Fig 4.1.1. To calculate the refractive index in grating we assume that the index is a linear average of the two mediums. The refractive index for the grating area is shown in equation (4.1.1); showing that the period of the binary grating will not affect the final result. So the binary grating model is a 3 dimensional problem.

$$n_g = n_{ambient} \cdot (1 - f) + n_{AR} \cdot f \quad (4.1.1)$$

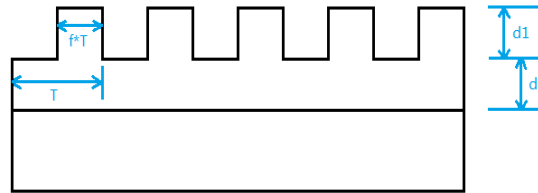


Fig 4.1.1 Binary rectangular-groove grating used for ARC with parameter notation

Choosing the grating material to be ZnS on c-Si (100), and $f = 0.5$, the minimum integrated reflectivity (reflection) occurs at *height-grating* = 80 nm, *layer-thickness* = 54nm, with the *reflection* = 5.40 %. Meanwhile, for $f = 1$, (single-layer dielectric) the minimum average of TE and TM polarization occurs at *height-grating* + *layer-thickness* = 56nm, with the *reflection* equal to 11.94 %.

Comparing $f=0.5$ and $f=1$, Fig 4.1.2 illustrates that the case of $f=0.5$ has lower minimum reflection. The refractive index is more continuous in $f=0.5$ than $f=1$. So it can be concluded that with the continuity of refractive index increasing from the ambient to the substrate, the reflection will highly reduce.

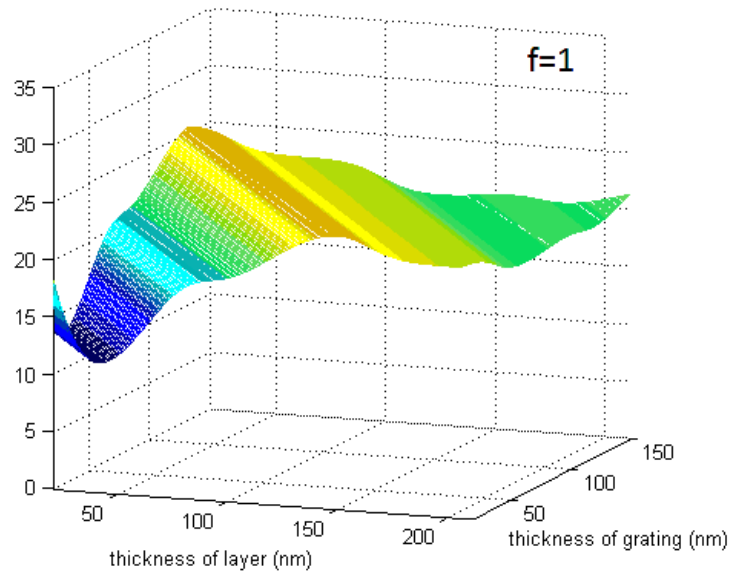
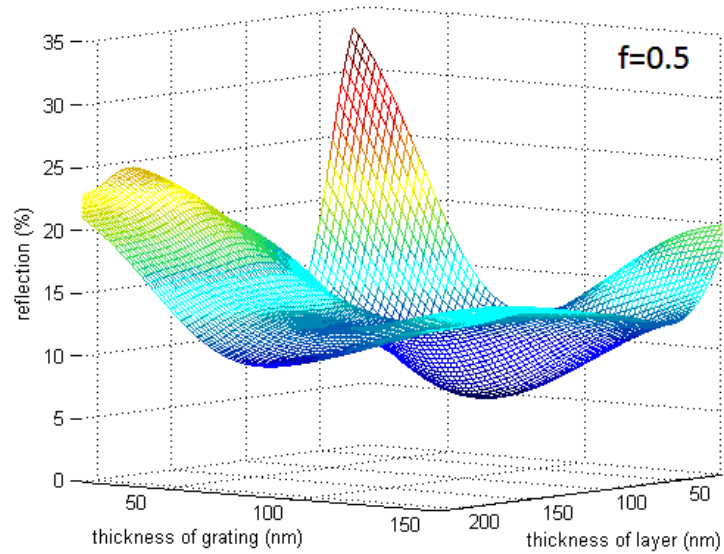


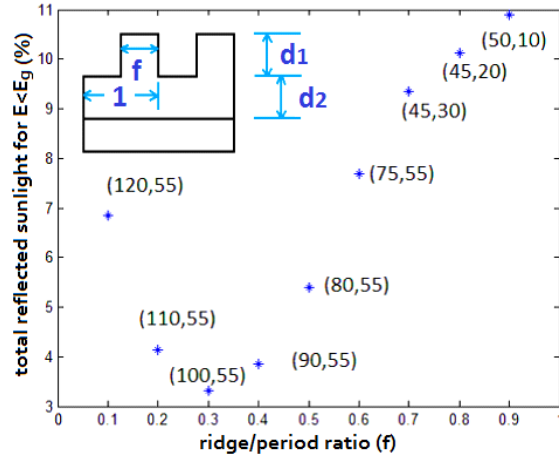
Fig 4.1.2 Reflection coefficient versus thickness comparison for double and single-layer

How will the reflection change with f ? Assume f varies from 0.1 to 0.9 and increases every 0.1, thicknesses for both grating and layer varies from 10 to 150 nm and increases every 5 nm, thus Fig 4.1.3 (a) can be obtained. Numbers in bracket near each point represent the corresponding thicknesses for grating and flat layer respectively. These

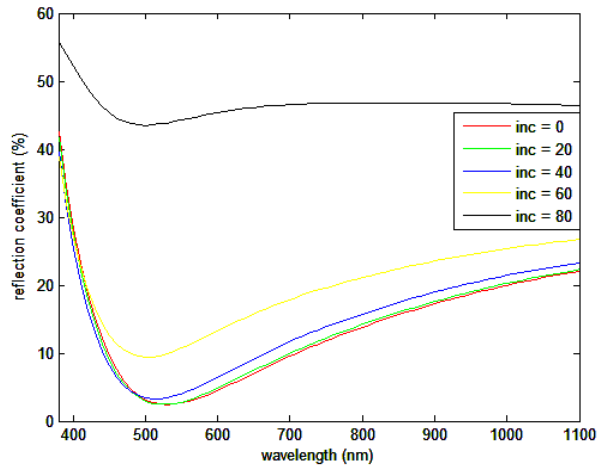
thicknesses are optimized for minimum total reflectivity, which represents the integral of reflectivity over the black body spectrum from 380 *nm* to 1100 *nm*. It also shows that with increasing *f*, the minimum reflection decreases until $f = 0.3$; and as *f* continuously increases, the minimum reflection increases.

We can see from Fig 4.1.3 (b) that there is an obvious trough on each reflectivity versus wavelength curve. Furthermore, as the incident angle increases, the reflection coefficient trough is increasing while the corresponding wavelength is decreasing.

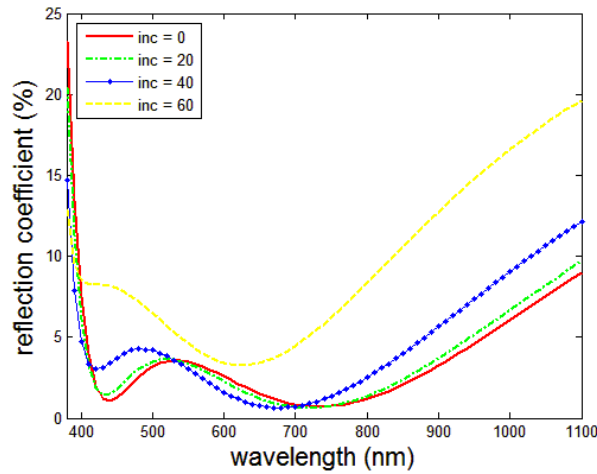
Reflectivity on c-Si(100) for binary rectangular-groove grating for ZnS is presented in Fig 4.1.3(c). As the Fig 4.1.3(c) shows, the optimal parameters are the thickness of grating equal to 100 *nm*, and the thickness of layer equal to 55 *nm*. The angular and the wavelength dependence for reflectivity at these settings are also shown in Fig 4.1.3(c). At the optimized thickness, the angular dependence for the binary grating structure is better than single-layer AR coating, with a wider window to reach low reflectivity. However, no significant improvement compared with double-layer ARC is seen, as shown in Fig 4.5.4. First, they all have a wide wavelength window for low reflectivity, from 440 *nm* to 700 *nm*. Second, the minimum reflection coefficients of the structure are nearly the same, because the effective result of the grating region is similar to that of MgF₂ in a double-layer. But the binary grating uses just one coating material, and can adjust the refractive index by ridge ratio, which can solve the problem of the availability to materials with the right indices.



(a)



(b)



(c)

Fig 4.1.3 Variation of reflectivity with various optimized parameters for ZnS binary grating structure.

(a) Minimum optimized total reflectivity vs. groove ratio for binary grating structure. Numbers in bracket near each point represent the corresponding thicknesses for grating d_1 and flat layer d_2 .

(b) Angular dependence for single-layer ZnS on c-Si (100) at optimized thickness 56 nm

(c) Angular dependence for ZnS binary grating with optimized parameters

The average reflectivity of 5% still did not satisfy our expectations, so we will continue to look for more complicated structures. From the analysis studied in binary grating, the continuity of refractive index plays a significant role in reducing reflection coefficient. Hence, dielectric textured materials with a continuous grating of refractive index should be studied.

4.2 1D Binary with Triangular Cross Section

From the analysis of binary grating, we find that if the refractive index of antireflection structure increases its continuity from ambient to substrate, the reflection coefficient would decrease. So why not make the structure even more continuous? Hence 1D grating with triangle cross section is studied, as shown in Fig 4.2.1. As the schematic shows in Fig 4.2.1 (b), if the triangle structure, whose height is H , is sliced into M layers, then the thickness for each layer is expressed as equation (4.2.1), and the distance from the center of the m^{th} layer to the top is expressed as equation (4.2.2). The refractive index for the m^{th} layer can be written as equation (4.2.3), where f_m is the ratio of dielectric material occupied within the m^{th} layer.

$$d = \frac{H}{M} \tag{4.2.1}$$

$$h_m = \left(m - \frac{1}{2}\right)d \quad (4.2.2)$$

$$n_m = n_{ambient} \cdot (1 - f_m) + n_s \cdot f_m \quad (4.2.3)$$

$$f_m = \frac{h_m}{H} \cdot \frac{a}{T} = \frac{a}{MT} \left(m - \frac{1}{2}\right) \quad (4.2.4)$$

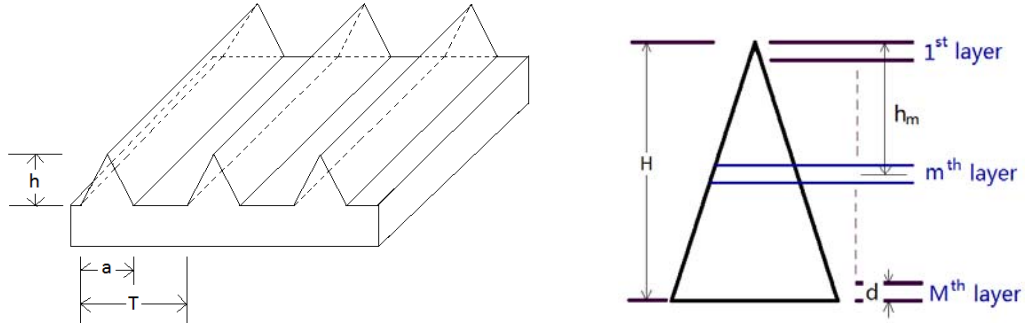


Fig 4.2.1 Schematic of 1D grating with triangular cross section

To minimize the refractive index variance, one can make the AR material to be made out of the substrate itself; and set the texturing to continuously grade till the planar part. 1D grating with triangular cross section (Fig 4.2.1) may act close to an ideal ARC; since the effective refractive index smoothly varies from the air to the substrate; which helps in minimization of reflection³. The next process is to figure out how the height would influence the integrated reflectivity. Take a Si solar cell as an example; when the occupation ratio a/T equals to 1, the refractive index can reach the most continuous condition. As Fig 4.2.2 shows, as the height increases, the smaller the reflectivity gets, because larger height increases the continuity of refractive index.

³ Here it is necessary to emphasize that transfer matrix method is only suitable for dielectric material. For instance for metal produced with Fig 4.2.1's structure, the average refractive index could vary continuously from air to bulk metal; but metal cannot transmit light, hence can't be used as a AR material.

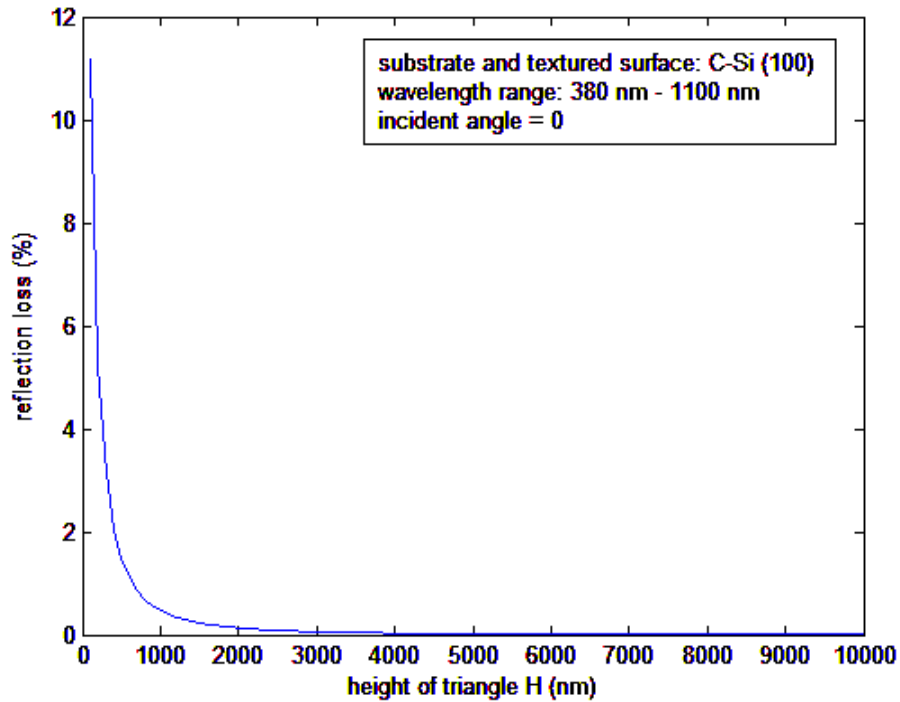


Fig 4.2.2 Reflectivity of 1D grating with triangle cross section versus the height of ridge

This 1D grating with triangle cross section is nearly ideal AR texture. It can make the reflectivity shrink to much lower than 1%, even for a whole spectrum from 380 *nm* to 1100 *nm*; when the height of triangle is above 800 *nm*, which indicates that over a large range of height, we can always get a low reflectivity. Next, the angular tolerance property of this structure is looked into. Setting the height to be 6 μm and analyzing the angular dependence of this 1D triangle grating, we can define the wavelength dependence and angular dependence for both TE and TM mode in Fig 4.2.3.

Three main indications can be concluded from Fig 4.2.3. First, as incident angle increases, the reflection coefficient increases sharply; however, even at incident angle of 80°, the reflectivity is still below 20%. For binary grating or double-layer structure, its average over all wavelengths, as shown is Fig 4.1.3 and Fig 3.6.4, reflection is around 40%.

Second, the TM polarization, at any incident angle (despite normal light) and at any wavelength, produces lower reflectivity than TE polarization. Third, as the incident angle increases, the reflectivity for TE polarization keeps on increasing, but TM polarization is not. Comparing $\text{inc} = 20^\circ$ with $\text{inc} = 30^\circ$ and $\text{inc} = 40^\circ$, we find at $\text{inc} = 20^\circ$ TM polarization has a larger reflectivity than the other two cases.

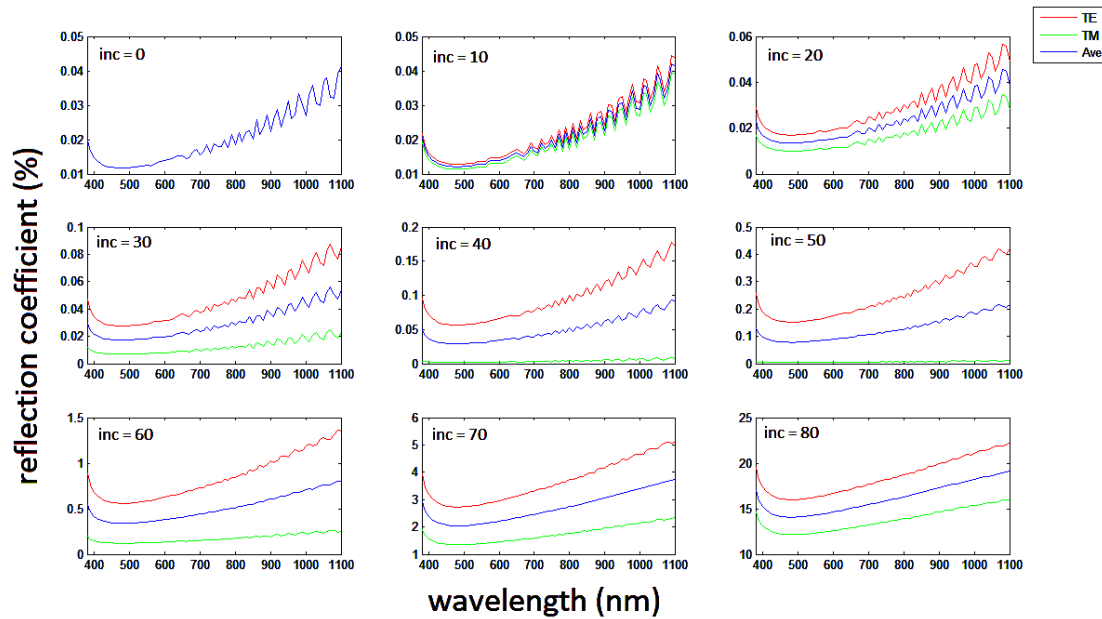


Fig 4.2.3 Angular and wavelength dependence for reflectivity at $H = 6000 \text{ nm}$

For a specific case with the height of the grating $h=6\mu\text{m}$, we could find the integrated energy loss dependence on incident angle in Fig 4.2.4. The energy loss is below 0.5% even at 60° incident angle. However, this application is not implementable for III-V solar cell. Firstly, the large area at the front surface increases the recombination velocity. Secondly, due to wavelength scale base for the structure, the scattering effect varies the light path length, leading to a challenge in optimizing the thicknesses of subcells. Thirdly, the micro-scale height of the texturing increases absorption.

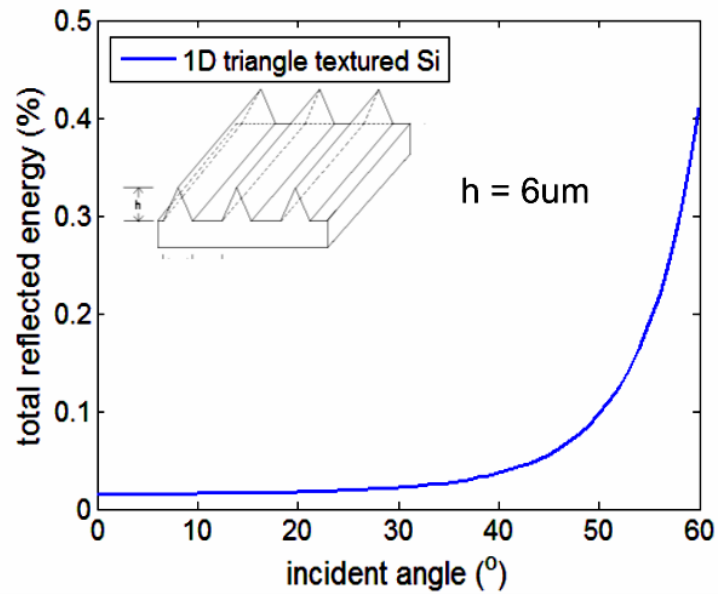


Fig 4.2.4 Reflection of 1D grating with triangle cross section

From the Fig 4.2.3, it can be seen that as the height of the triangle increases, (resulting in a smaller gradient in the refractive index), the integrated reflectivity decreases. Compared with 2D pyramid or needle like texture, the gradient is larger if they are of the same height as 1D triangle grating. Consequently, to get the same antireflection result, the height of the 2D structure ought to be larger. This approach consequently is more applicable for Si solar cell, with low absorption coefficient, instead of III-V solar cells.

In the literature, it is shown that silicon nanotips^[84] and syringe-like Si nano-wire^[85] experimentally could get the reflectivity as low as 1%; but when the height of structure is in micro scale, which matches with this simulation prediction. The optimized parameter exceeds low profile limit, not fitting in the thin film method modeling requirements. So the thin film method cannot give a precise evaluation, only a rough estimate. The micro scale direct texturing is hindered in III-V multi-junction solar cells. All these facts

demand antireflection dielectric structure on III-V solar cells. Later, we will discuss its application to specific solar materials; with focus on wavelength and angular dependence.

4.3 2D Hemisphere Grating

As the Fig 4.3.1 shows, the hemisphere with radius R is sliced into M layers. If the number of layers is large enough, so that the m^{th} layer in the middle can be approximated as a cylinder, whose radius is given by equation (4.3.1), and thickness is given by equation (4.3.2), then the distance from the center of cylinder to the bottom is shown as equation (4.3.3). The ratio occupied by the dielectric material with each period can be written as equation (4.3.4). The refractive index for the grating area is shown as equation (4.3.5), indicating that the period of the binary grating will not affect the final result.

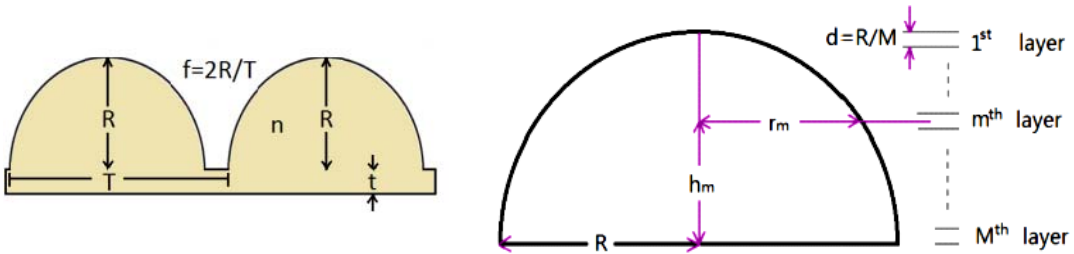


Fig 4.3.1 Structure and parameter notation for 2D hemisphere grating

$$r_m = \sqrt{R^2 - h_m^2} \quad (4.3.1)$$

$$d = R/M \quad (4.3.2)$$

$$h_m = \left(M - m + \frac{1}{2}\right)d \quad (4.3.3)$$

$$f = \frac{\pi r_m^2}{\pi R^2} = \left(\frac{r_m}{R}\right)^2 \quad (4.3.4)$$

$$n_g = \left(n_{\text{ambient}}^2 \cdot (1-f) + n_{AR}^2 \cdot f\right)^{1/2} \quad (4.3.5)$$

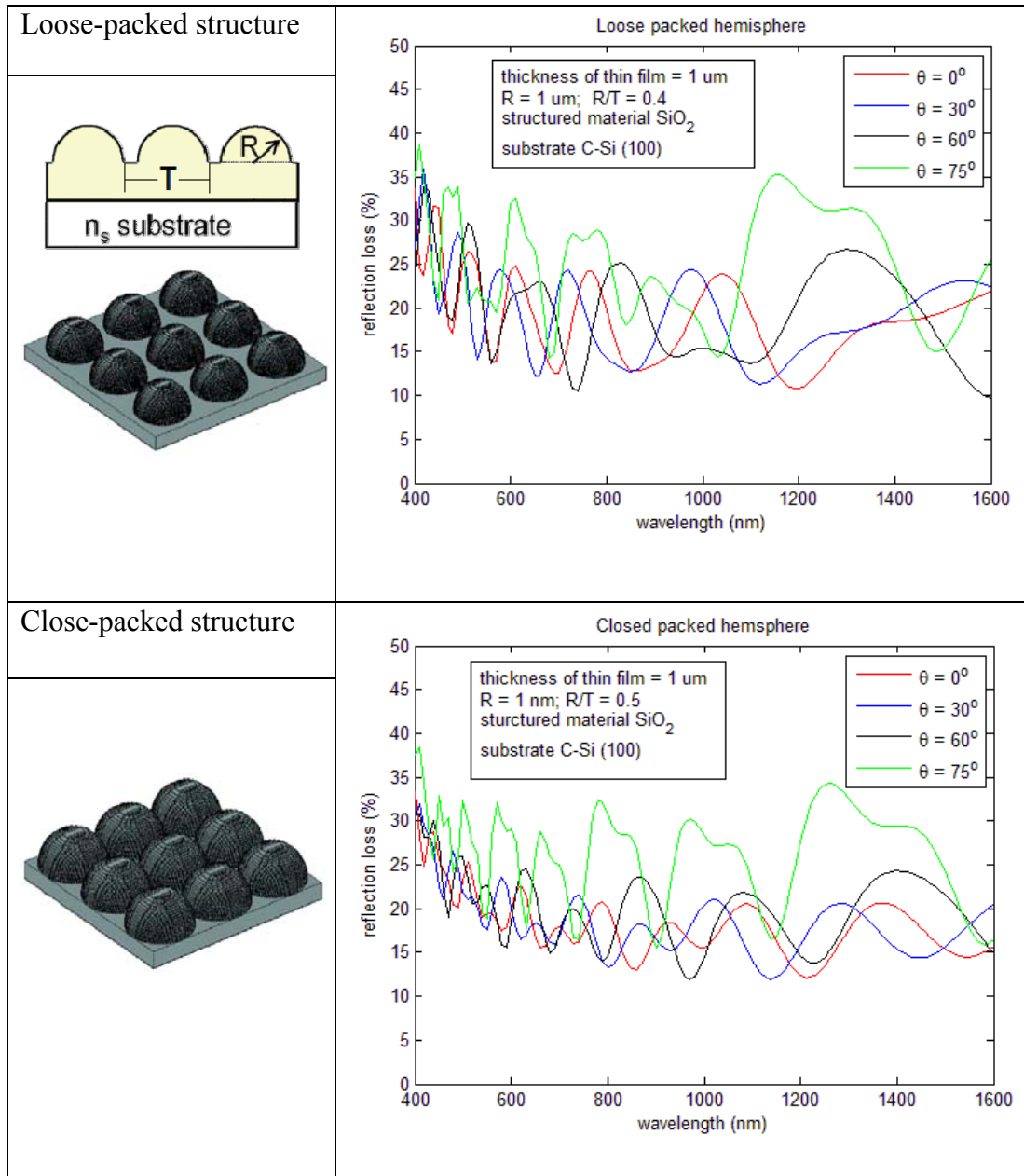


Table 4.3.1 2D hemisphere textured surface reflectivity versus wavelength

To compare with the result from RCWA, all the parameters are set to be the same as in the literature where the textured surface SiO_2 is fabricated on c-Si(100). Where, the radius of the hemisphere is $1\mu\text{m}$, the thickness of thin film under hemisphere is $1\mu\text{m}$. Loose packed ratio, referring to the rate between the diameter of hemisphere and

structure period, is 0.4. For close packed structure, the only difference is the *ratio* to be 0.5. By modeling, we can get the following images in Table 4.3.1.

Comparing the transfer matrix result with RCWA simulation^[86], beside the periodic property and divergence between incident angle as discussed in pyramid texturing, we found there is another discrepancy. We can see from RCWA's result, the reflectivity with incident angle = 30° is even smaller than that of incident angle = 0°, which is not quite convincing. Again, transfer matrix still can get a good approximation at micro scale for hemisphere structure, which gives us confidence in transfer matrix to optimize 2D AR textures.

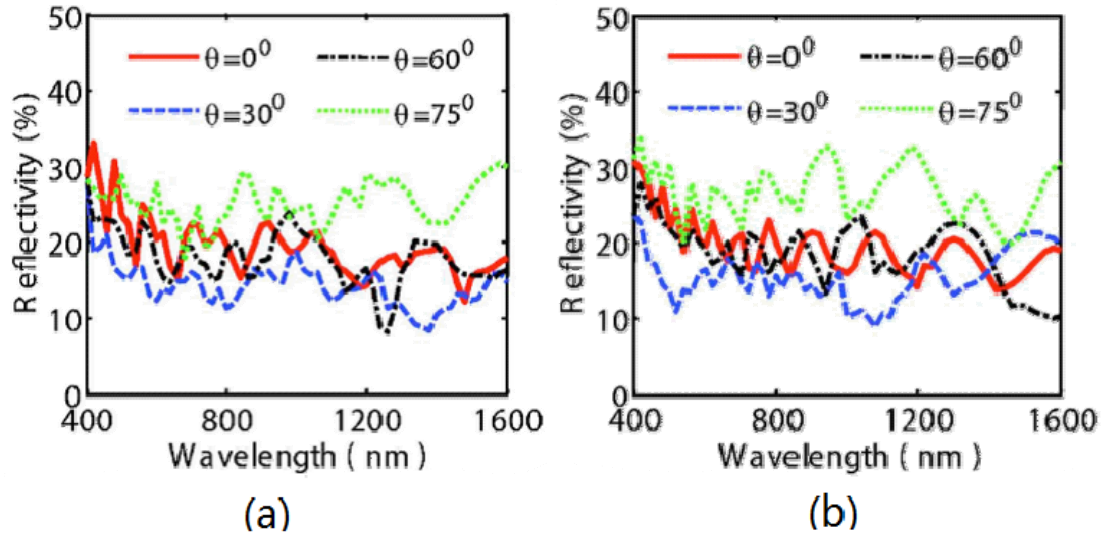


Fig 4.3.2 Reflectivity simulation of hemisphere grating from the literature: (a) loose-packed structure, (b) close-packed structure [ref. 86]

In a typical triple junction solar cell, GaInP, GaAs and Ge are used for each junction from top to bottom. Generally, 15-20 nm Al-rich AlInGaP or Al-rich AlGaAs are used as low surface recombination velocity window layers. Because the refractive indices for AlGaInP and AlGaAs are close to each other; here Al_{0.8}Ga_{0.2}As is considered as the top

semiconductor layer beneath the antireflective structure. The variables for hemisphere structure include the radius R , ratio of ridge f , and the coating material's refractive index n_{AR} . By optimizing the texturing, we found that when the ideal refractive index of antireflection material is 2.4, the ideal ratio of groove f is 0.6. The minimum fraction of the reflected photons from 380 nm to 2000 nm would occur, in materials like TiO₂ and ZnS.

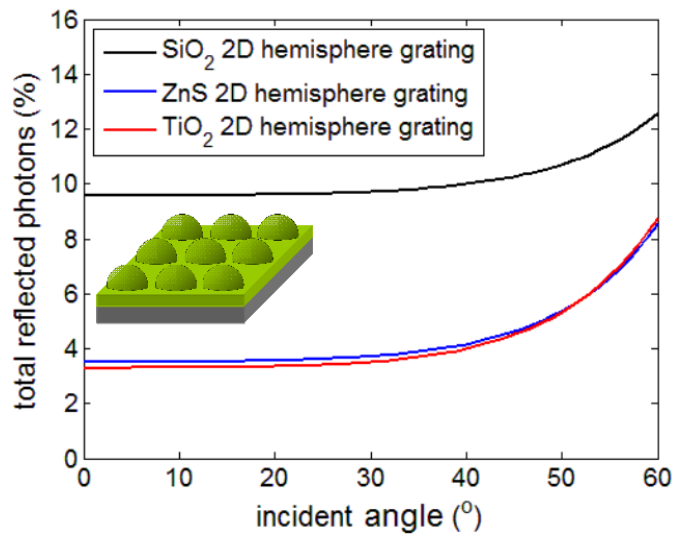


Fig 4.3.3 Angular dependent photon losses for 2D hemisphere grating made with various materials for an AM1.5G incident spectrum over the 0.38-2 micron range

Further analysis of the parameters allowed us to optimize each material for normal light. Although refractive index of ZnS and TiO₂ are not quite the same^[87], they can lead to similar angular and wavelength dependence as shown in Fig 4.3.3. The reflectivity is tolerant of incident angle, around 3.3% when it is less than 30°. As the angle increases to 60°, the reflectivity reaches up to 8.8%. Since SiO₂ is widely used as ARC (and plasmonic) material, it has been also included in our simulations; yet as shown here, SiO₂ performs poorly in comparison with materials having higher indices of refraction.

4.4 2D Pyramid Grating

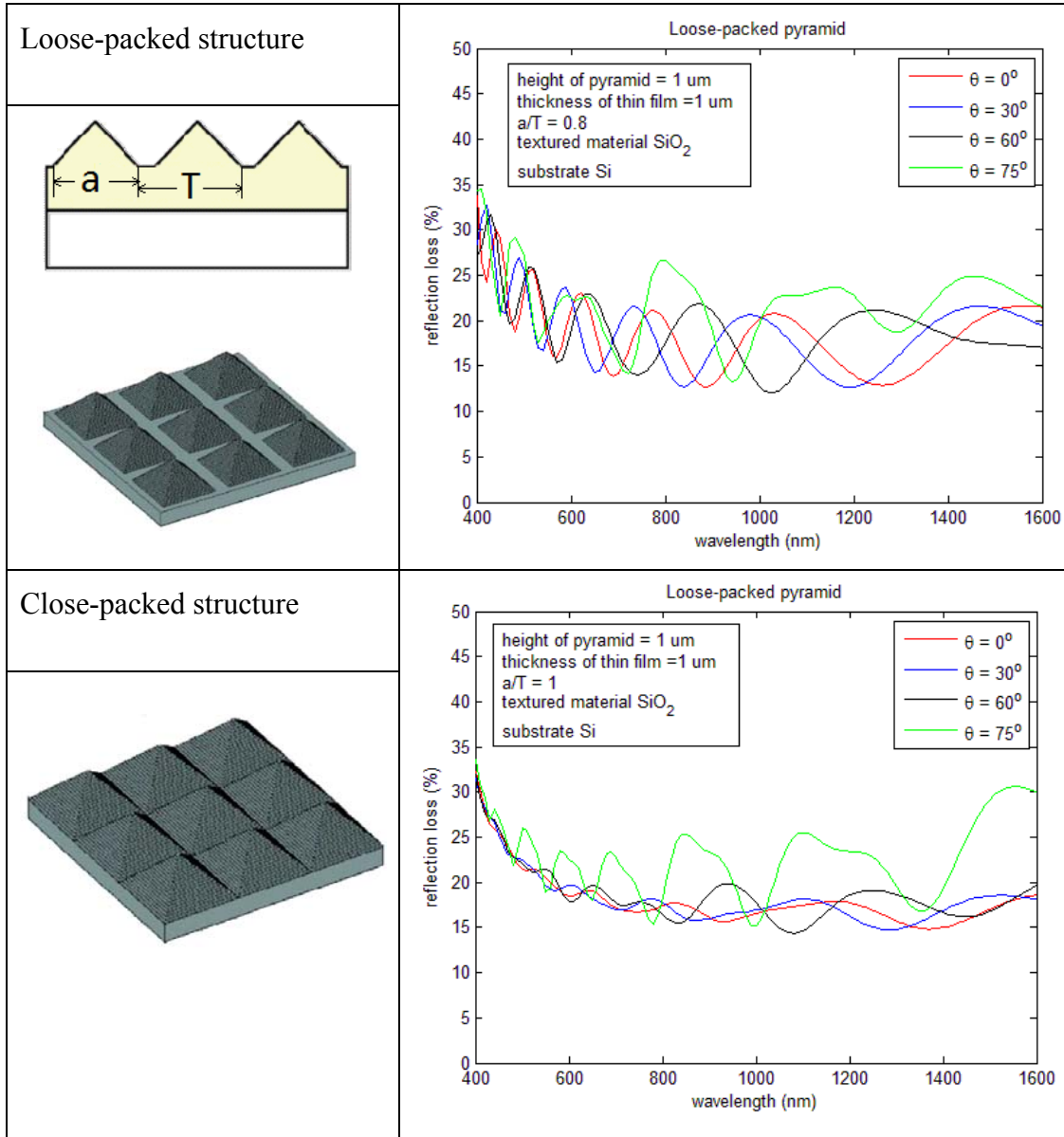


Table 4.4.1 2D pyramid textured surface reflectivity versus wavelength with angular dependence

Similar to the analysis in 1D grating with triangular cross section, the ratio for 2D pyramid is just the square of the right side of equation (4.5). To compare with simulation in literature, all the parameters are set to be the same, (and for better comparison, the

linear average of electric permittivity^[88] is taken; as the model of RCWA suggests, instead of the linear average of refractive index), results are shown in Table 4.4.1.

Comparing with the result from RCWA in the literature^[89], above results are roughly in the same reflectivity region, oscillating among identical values. It also obeys the general law that as incident angle increases, reflectivity increases. However, this result from the transfer matrix has more explicit periodic property; and the difference from different incident angle is not as obvious as that from RCWA, as shown in Fig 4.4.1.

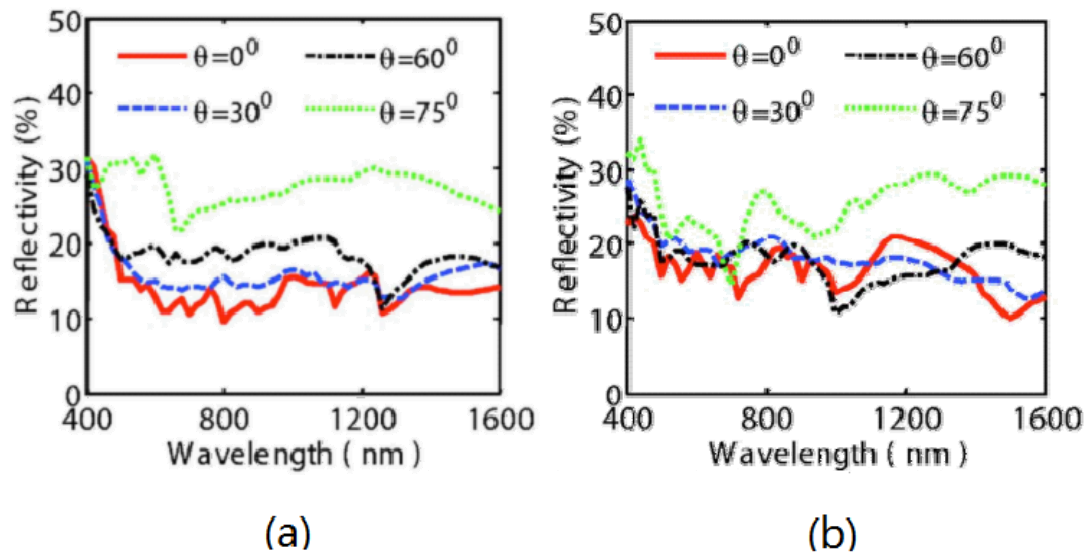


Fig 4.4.1 Reflectivity simulation of pyramid grating from the literature: (a) loose-packed structure, (b) close-packed structure [ref. 86]

The main reason could be the limitation of the transfer matrix that is dealing each layer as independent and uniform dielectric material, which requires periodic textured surface to be in order of sub-wavelength range. However, the parameters used in literature are at micro scale, which is out of the transfer matrix's application. However, RCWA is based on Fourier transform; which takes into account multi-reflections between periodic textures. Despite ignoring multi-reflections between periodic textured surfaces, transfer

matrix can still create a good approximation even for micro scale pyramid structure. This is due to the fact that effect of multi-reflections is relatively small.

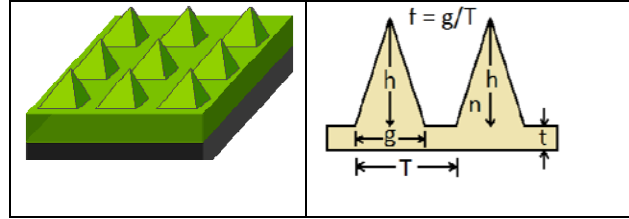
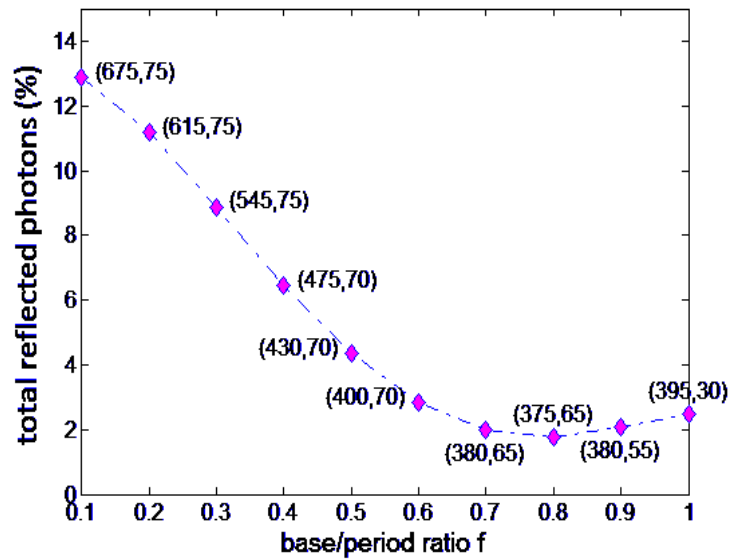


Fig 4.4.2 Structure of 2D pyramid grating with parameter notation

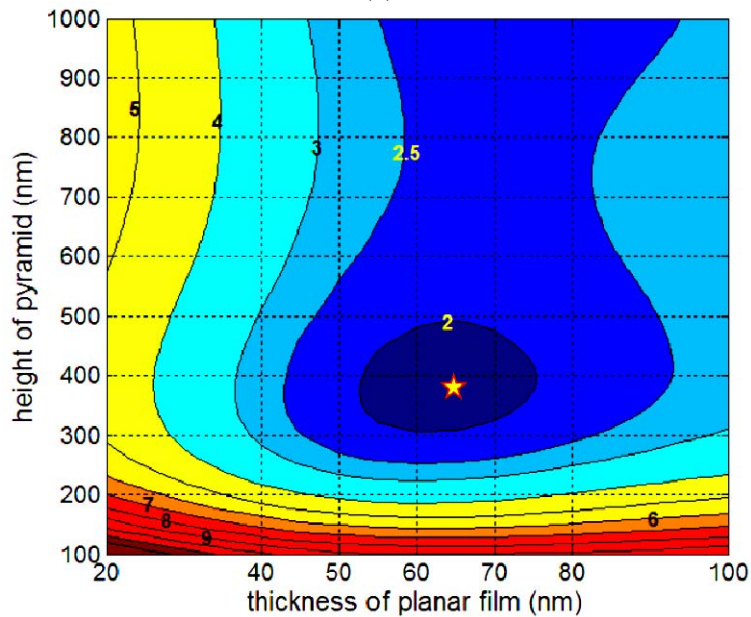
Similar to the optimization in the hemispherical array structure, the minimum photon-loss occurs when the ridge ratio is equal to 0.8, and the AR's refractive index is equal to 2.6. The closest materials to this index are SiC and ZnS. A more optimal matching of h , t and f can be made with ZnS dispersion data. We find that for efficiently coupling the light in a wide spectral range (380-2000 nm), the optimal pyramid AR structure for normal light, with an integrated photon loss of 1.83%, occurs when its pyramid height is 375 nm , the thickness of planar film is 65 nm , and the ratio of ridge is 0.8. Effect on reflectivity with variation of the base/period ratio, the pyramid height and the thickness of planar film is shown in Fig 4.4.3. It is shown that the pyramid grating has fabrication tolerance, which is around 100 nm in height and 15 nm in thickness. The f ratio of the pyramid base versus the pitch is set at 0.8.

From this geometric property, we can get the angular dependence of the ZnS pyramid antireflection texture; as shown in Fig 4.4.4. Hence, we can see that the optimized pyramid texture performs better, both over the spectrum range and over wider incidence angles. When the incident angle is less than 30° , the photon loss is nearly independent of

incident angle, ($\sim 1.8\%$), however, as the angle increases beyond 40° , the photon loss increases sharply. As the angle increase to 60° , the photon loss reaches nearly 5%. When compared with conventional double-layer ARC, and 2D hemisphere grating, 2D pyramid grating exhibits better antireflection and angular tolerance properties.



(a)



(b)

Fig 4.4.3 Optimization of ZnS 2D pyramid grating from 380 nm to 2000 nm (incident AM1.5G)

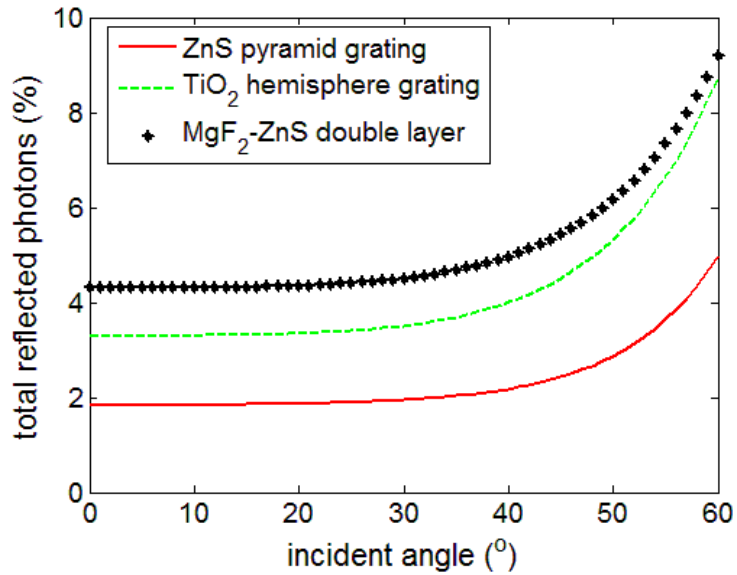


Fig 4.4.4 Photon loss comparison for proposed structures with conventional double-layer ARC

4.5 2D Pyramid Texture for Multi-junction Cells

Until now, all the optimizations have been presented by minimizing the total photon-loss from 380 *nm* to 2000 *nm*, and it has been found that 2D pyramid texture has the best AR property. Now we will take into account the integrated photon loss in each subcell, which will be a crucial factor for maintaining current matching for the multi-junction solar cell.

As shown in Fig 4.5.1, under normal sunlight incidence, for a GaInP/ GaAs/ Ge multi-junction solar cell, the main current loss caused by AR grating is associated to the GaInP subcell (these devices being inherently current rich for Ge subcell). In this case the minimum current loss happens when the base/period ratio is 0.8, the height of pyramid is 330 *nm*, and the thickness of planar film is 65 *nm*. Similar optimization can be done for operation under concentration, by integrating photon loss over the entire incidence cone. Hence, the geometric parameters for the gratings can be different from those under

normal light. Gratings need to be specifically designed for various concentrators and solar cell devices. The current loss in each subcell resulting from AR structure is shown in equation (4.5.1).

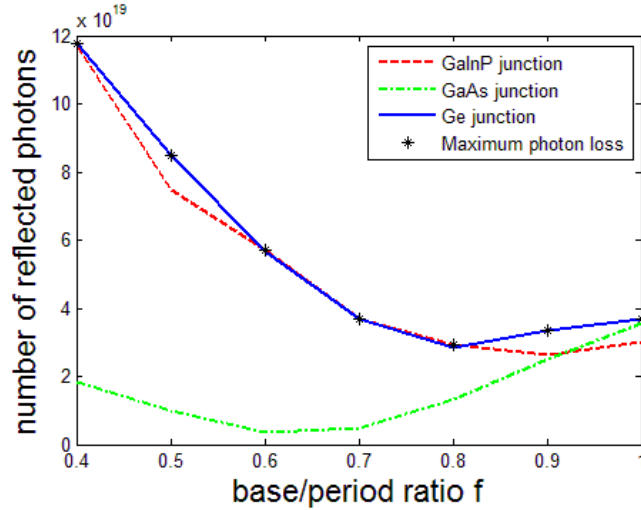


Fig 4.5.1 AR grating causing photon loss in each junction for a GaInP/GaAs/Ge multi-junction solar cell under AM1.5G illumination

Fig 4.5.2 shows the schematic of a concentrator with the acceptance angle of α , and the notations used in eqn. (4.5.1). As shown in eqn. (4.5.1), the concentration factor has no effect on the total current loss.

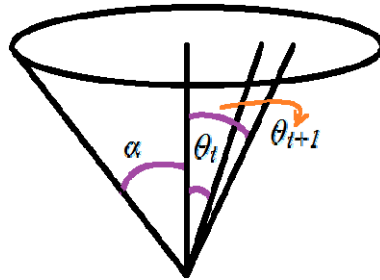


Fig 4.5.2 Notations of concentrator's light cone

$$I_u = q \frac{\sum_{i=1}^{m-1} \pi (\tan^2 \theta_{i+1} - \tan^2 \theta_i) (N_{u,i} + N_{u,i+1}) / 2}{\pi \tan^2 \alpha} \quad (4.5.1)$$

where, u is the index or subcell (varying from 1 to the number of junction in multi-junction devices),

q is the electron charge,

i is the order of annulus from the center to the outer edge of concentrator.

Assume the concentrator was divided into m annuluses, $\theta_m = \alpha$ is concentrator's acceptance angle. $N_{u,i}$ is the integrated photon loss at i^{th} annulus over the u^{th} subcell's working spectrum.

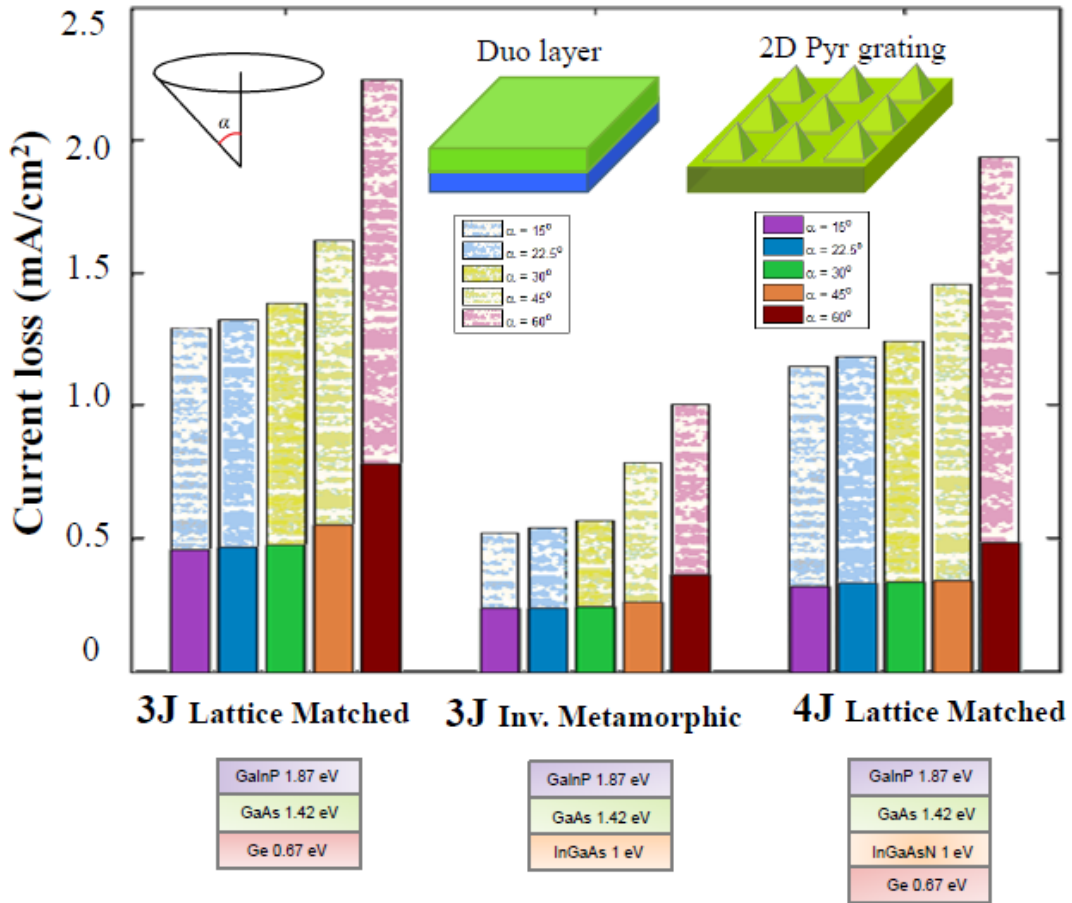


Fig 4.5.3 Comparison of current loss (between duo layer (crayon) and 2D pyramid grating (solid color) on multi-junction devices), as a function of angle of focusing cone, for various multi-junction devices

Compared with parameters like the base planar thickness and the occupation ratio; it demonstrated that the height of pyramid is more sensitive to the light cone's acceptance angle. Fig 4.5.3 illustrates the results for 2 common triple-junction (3J) devices and a 4-junction device. When operating in conjunction with imaging concentrators (*i.e.* Fresnel or parabolic), at high acceptance angle ($\sim 60^\circ$), for an optimal dielectric sub-wavelength texturing, enables current losses for these devices (optimized for minimum photon loss conditions), to be less than 2.2%, 3J-LM GaInP(1.87 eV) / GaAs(1.42 eV) / Ge(0.67 eV), 2.7% for MM GaInP / GaAs / InGaAs(1.0 eV), and 3.8% for 4J hypothetical GaInP/ GaAs / InGaAs / Ge solar cell.

Conclusion

Here we show that for single and multi-junction III-V devices, operating under high concentration, the implementation of a carefully designed 2D sub-wavelength grating significantly reduces the photon losses and current matching issues, over those commonly encountered for planar double-layer ARCs. As the thin film method is based on dividing the complex structure into multi-layers, and treating each layer to be uniform. Number of layers to be sliced is the crucial factor. As we expect, the more layers to be sliced, the more precise the result should be. When the thickness of the layer is equal to one tenth of the minimum wavelength is the critical point.

Chapter 5 Results and Conclusion

From the properties of light propagation, it was found that the presence of consecutive refractive indices from ambient to substrates can highly reduce reflectivity, and even at large off-normal incidence angles, reflectivity stayed at a low value. A modeling example in this work of textured Si solar cells with triangle cross section grating showed that in the case of micro-scale height grating, the reflection loss was dramatically reduced to less than 0.1%, and even at 60° off-normal direction, the reflection loss was kept below 1.5% for a silicon solar cell. Micro-texturing is not implementable for III-V semiconductor solar cells, mainly because of their large absorption coefficient and short diffusion length ($3 \mu\text{m}$). Hence, the generated e-h pairs would recombine before traveling to the electrodes. The remaining option is a sub-wavelength dielectric AR texturing coated on semiconductor surfaces. In this study, dielectric materials with transparent properties in the working spectrum, such as ZnS and TiO_2 , were chosen as AR-textured materials, instead of direct texture on III-V solar cells. Sacrificing the consecutive refractive indices from dielectric materials to substrates, the textured AR could, at the most, eliminate the refractive indices discontinuity from the ambient to AR materials. The plausible expectation, that a full occupation of the surface by the grating contributes to the best results (because of discontinuous refractive index from air to AR materials), is seen to be false; in fact 0.7-0.8 occupation rate might demonstrate better AR property relating to geometric shape. Since the ideal refractive index for each layer is centrosymmetric about the central layer (and not the central thickness), and the discontinuity between AR material and solar cell is unavoidable, partial occupation can help the refractive indices

create a near-centrosymmetric structure. High index materials were preferred to reduce the discontinuity between solar cells substrate and AR materials.

In this work, modeling of AR properties for single and multi-junction III-V semiconductor solar cells was undertaken for various grating structures and materials. The physical approximation used in this model was the so-called thin film method, which considers all structures as composed of a pile of homogeneous layers, with each layer possessing uniform optical properties. The multi-reflections at the interface between every set of two layers were also taken into account, but not the multi-reflections between grating surface planes. The approximated uniform homogeneous layers possess an effective refractive index between that of air and bulk AR material, depending on the grating shape and AR occupation ratio. This was shown with a simple scenario, where the AR grating was fabricated on multi-junction devices with the working mechanism of a single-junction, absorbing photons above the lowest bandgap.

The first step of the modeling work assumed that the refractive index of the AR material is independent of wavelength. Under this assumption, the refractive index and geometric parameters can be varied using several loops. Among all combinations, the optimized point for minimum integrated photon-loss can be figured out, indicating which materials would be better candidates. The second step of the simulation was to take the optical properties of a specific material into account, whose dispersion character was close to the optimized refractive index. Optimization of its geometric parameters was further done. In accordance with existing experimental technologies, this process was implemented for 1D rectangle groove grating, 1D triangle groove grating, 1D hemisphere grating, 2D

hemisphere grating, and 2D pyramid grating, analyzed for Si or GaAs solar cells.

According to the calculation, 2D pyramid grating demonstrated outstanding antireflection and angular tolerant properties over 380 *nm*-2000 *nm* AM 1.5G spectrum for Al_{0.8}Ga_{0.2}As window layer solar cells; and 2D hemisphere grating showed the second best properties. Up to this point, the calculation was performed over the multi-junction's working spectrum but treating the multi-junction as having a single junction's mechanism; which is minimizing the integrated reflectivity over the whole spectrum. A more precise model was required to deal with multi-junction cases.

For the optimization of the reflection, the integrated reflectivity over black body radiation spectrum was substituted for integrated photon-loss over AM 1.5G spectrum. At the same time, due to current matching issue, where the smallest current among all junctions is the final current of the solar cell device, current-lacking subcells are preferred to have the minimum current loss / photon-loss in their working spectrum, and current-rich subcells can endure high photon-loss. Moreover, the solar cell design was not combined with light-coupling issue, so the solar cell devices were assumed to be well designed and each subcell could generate the same amount of current. The new objective was to minimize the maximum photon loss among all the subcells. For commercial usage, multi-junction solar cells are widely applied under concentrators to obtain higher efficiency. The optimization for solar cells operated under concentrators is an integral over all the angles. So the geometric parameters are different from those under normal light, and gratings need to be specifically designed for various concentrators and solar cell devices. This is the concept for optimizing multi-junction solar cells under concentrators. 2D pyramid

ZnS AR grating, which presented the best properties for single junction devices, was optimized for 3J GaInP/ GaAs/ Ge, GaInP/ GaAs/ InGaAs, and 4J GaInP/ GaAs/ InGaAs/ Ge solar cells under 30°- 120° wide angle concentrators. The maximum current loss among all their subcells was shown as well.

Furthermore this study showed that the transfer matrix method based on thin film model is a more effective approach to simulate sub-wavelength scale dielectric textures compared to advanced rigorous coupled wave analysis (RCWA), although there are some shortcomings. The first issue is ignoring the scattering effect, which is significant when the circumference of the structure is in the wavelength and sub-wavelength scale, because the morphology was dealt as a pile of homogeneous planar layers. Secondly, the base parameter was eliminated in modeling, as the average approximation works, although the base parameter of grating was a variable. Third, this model only deals with light-coupling and -trapping, not considering that large incident angles amplifying the light paths in solar cells will result in solar cells design issue. The fourth shortcoming is that more complex structures can be made experimentally, and they were not analyzed in this work. These shortcomings are not significantly serious in this modeling work. The scattering effect will not bring about a serious difference because it is negligible compared to reflection phenomena, and scattered photons are still transmitted. Using a uniform refractive index for each layer can work for this model because the final optimized structures agree with the sub-wavelength assumption. The light path issue can be solved when combining drift-diffusion model with light coupling analysis, as the light paths can be described in the drift-diffusion model. Lastly, complicated structures are not obstacles

for simulation work, since any morphology function can be taken in the modeling ^[90].

Future work: nano-imprinting technique ^[91,92] utilizes the mixing of polymers with nanoparticles, and printing the structure by molds. From this technique, high index nanoparticles can cooperate with low index polymers and turn out medium index materials that could meet the optimization index needed. Some high-index but high-
evaporation-temperature materials, such as SiC, would no longer be a barrier for grating techniques.

Appendix A: Equations in Drift Diffusion Model

$$J_{0p} = -\left(\frac{qD_n}{L_n}\right)n_0 \left[\frac{\left(\frac{S_n L_n}{D_n}\right) \cosh\left(\frac{x_s}{L_n}\right) + \sinh\left(\frac{x_s}{L_n}\right)}{\left(\frac{S_n L_n}{D_n}\right) \sinh\left(\frac{x_s}{L_n}\right) + \cosh\left(\frac{x_s}{L_n}\right)} \right] \quad (\text{A.1})$$

$$J_{0n} = -\left(\frac{qD_p}{L_p}\right)p_0 \left[\frac{\left(\frac{S_p L_p}{D_p}\right) \cosh\left(\frac{x_1}{L_p}\right) + \sinh\left(\frac{x_1}{L_p}\right)}{\left(\frac{S_p L_p}{D_p}\right) \sinh\left(\frac{x_1}{L_p}\right) + \cosh\left(\frac{x_1}{L_p}\right)} \right] \quad (\text{A.2})$$

$$J_{1p} = -\left(\frac{q\phi e^{-\alpha(x_1+x_2)}}{1-\alpha^{-2}L_n^{-2}}\right) \left\{ 1 - \alpha^{-1}L_n^{-1} \frac{\left(\frac{S_n L_n}{D_n}\right) \left[\cosh\left(\frac{x_s}{L_n}\right) - e^{-\alpha x_s} \right] + \sinh\left(\frac{x_s}{L_n}\right) + \alpha L_n e^{-\alpha x_s}}{\left(\frac{S_n L_n}{D_n}\right) \sinh\left(\frac{x_s}{L_n}\right) + \cosh\left(\frac{x_s}{L_n}\right)} \right\} \quad (\text{A.3})$$

$$J_{1n} = -\left(\frac{q\phi}{1-\alpha^{-2}L_n^{-2}}\right) \left\{ -e^{-\alpha x_1} + \frac{-e^{-\alpha x_1} \sinh\left(\frac{x_1}{L_p}\right) + \alpha D_p + S_p - e^{-\alpha x_1} \cosh\left(\frac{x_1}{L_p}\right) S_p}{\alpha \cosh\left(\frac{x_1}{L_p}\right) D_p + \alpha \sinh\left(\frac{x_1}{L_p}\right) L_p S_p} \right\} \quad (\text{A.4})$$

$$J_{dep} = -q\phi e^{-\alpha x_1} (1 - e^{-\alpha x_2}) \quad (\text{A.5})$$

$$J_r = -\frac{qn_i x_2 \pi}{2\sqrt{t_n t_p}} \left[\frac{2 \sinh\left(\frac{qV}{2kT}\right)}{\frac{q(V_{bi} - L_p)}{kT}} \right] \quad (\text{A.6})$$

where x_3 , D_n , S_n , L_n are thickness, diffusion coefficient, surface recombination

velocity, and minority carrier diffusion length in n type materials respectively. Similarly x_1 , D_p , S_p , and L_p are thickness, diffusion coefficient, surface recombination velocity, and minority carrier diffusion length in p type materials respectively. (Minority carrier's diffusion length is indirectly related to doping concentration. Highly doped materials results in shorter diffusion length.) The surface recombination velocity is reduced by the use of passivation layer. α is absorption coefficient of the material and it depends on incident photon energy. ϕ is the solar flux which is arriving on the cell, x_2 is the depletion width, V_{bi} is the built in voltage, and V is the external voltage applied, t_p and t_n are recombination lifetimes for Shockley-Read-Hall effect in depletion region. These equations are valid for p on n device configuration. For an n on p device, the same equations can be applied by switching p and n terms. We can see that the drift diffusion model is quite a realistic model, which can optimize thickness of each domain and predict close to experimental result's efficiency^[93]. The defects, doping concentration, and external potentials are all directly or indirectly expressed in the data of diffusion length and life time.

Appendix B: Solar Cell Techniques to Appease Lattice Mismatch

B.1 Buffer layer between subcells

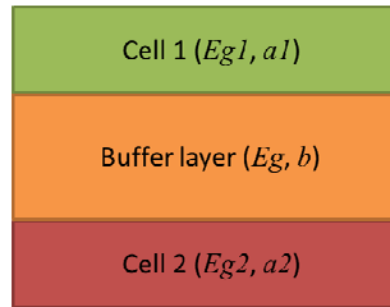


Fig B.1 Buffer layer

InGaP/ GaAs/ Ge, the only combination that could meet the lattice matching requirement, is generally grown on either highly doped conductive Ge or GaAs substrate, although their bandgap is not well adjusted to that of optimized ideal three junction cells. For more optional materials and better bandgap selection, metamorphic solar cells were designed, with buffer layer releasing the band strain.

From detailed balance limit, triple-junction solar cells with optimized bandgap could be either GaInP /GaAs /GaInAs or GaInP /GaInAs /Ge. GaInAs' bandgap can be controlled by the In composition. The main challenge for the bandgap flexibility given by metamorphic materials is that lattice mismatched growth typically causes crystal dislocations. Dislocations would result in energy levels in the middle of the bandgap, which lead to SRH recombination. A composition graded buffer is used to accommodate misfit and threading dislocations to the greatest extent. The active metamorphic (meaning changed form) device layers can then be grown relaxed with low dislocation density at the new lattice constant. The buffer layer should be the

material whose lattice constant can gradually vary from that of the first subcell to the second subcell, which would not absorb any active photons as well. Assuming two subcells have different lattice constants, as shown in Fig B.1. $E_{g1} > E_{g2}$, with lattice constant $a_1 \neq a_2$, the buffer layer's lattice constant b varies from a_1 to a_2 , top to bottom. In order to avoid absorbing photons that can be utilized by cell 2 which uses the photons with energy $E_{g1} \sim E_{g2}$, the bandgap of the buffer layer E_g needs to be larger than E_{g1} .

B.2 Inverted metamorphic multi-junction (IMM)

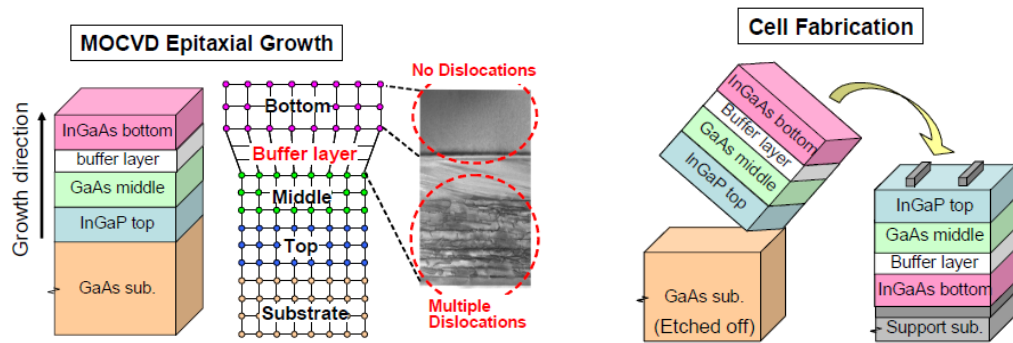


Fig B.2 Cell fabrication by inverted layers transfer process^[16]

As the name states, IMM is a metamorphic multi-junction solar cell grown top cell under the bottom cell. The GaInP top cell and GaAs substrate/middle cell are lattice matched, so the only mismatch is the interface between GaAs middle cell and InGaAs bottom cell. After the growth, the whole cell is etched off from the GaAs substrate and mounted on a support substrate. This technique could effectively avoid the lattice mismatch issue between the bottom cell and substrate. The highest efficiency reported among IMM cells is 35.8%, which indeed improves upon the efficiency of MM and LM.

Appendix C: Fresnel Equation Derivation

To get the ratio between amplitudes of reflected wave and incident wave, Maxwell's Equations can be used. The equations (C.1) (a), implementing the absence of free charges and free currents, (and using the fact that for most non - magnetic materials, $\mu_0 = 1$), can be reduced to equations (C.1)(b).

$$\begin{aligned}
 \nabla \cdot \vec{D} &= \rho & \nabla \cdot \vec{D} &= 0 \\
 \nabla \cdot \vec{B} &= 0 & \nabla \cdot \vec{B} &= 0 \\
 \nabla \times \vec{E} &= -\frac{\partial \vec{B}}{\partial t} & \nabla \times \vec{E} &= -\frac{\partial \vec{B}}{\partial t} & \text{(a)} & \text{(b)} & \text{(C.1)} \\
 \nabla \times \vec{H} &= \vec{J} + \frac{\partial \vec{D}}{\partial t} & \nabla \times \vec{H} &= \frac{\partial \vec{D}}{\partial t}
 \end{aligned}$$

Hence, at the interface between medium 1 and medium 2, we have equation (C.1) (c)

$$\begin{aligned}
 \vec{n} \times (\vec{E}_2 - \vec{E}_1) &= 0 \\
 \vec{n} \times (\vec{H}_2 - \vec{H}_1) &= 0 \\
 \vec{n} \cdot (\vec{D}_2 - \vec{D}_1) &= 0 \\
 \vec{n} \cdot (\vec{B}_2 - \vec{B}_1) &= 0
 \end{aligned} \tag{c} \tag{C.1}$$

The interface between the two media is assumed to be infinitely large, and the beam of plane wave from medium 1 that enters the interface is in the form of equation (C.2).

$$\vec{E}(\vec{r}, t) = \vec{E}_0 e^{i(\vec{k} \cdot \vec{r} - \omega t)} \tag{C.2}$$

where, ω is the frequency of light,

\vec{k} is wave vector,

\vec{r} is the point of interest in coordinate space.

And this wave results in two new plane waves at the interface, where we call the one propagating in medium 1 the reflected wave, and the one propagating in medium 2 the transmitted wave. Compared with (C.2), the reflected wave and transmitted wave are of the same form as (C.3).

$$\vec{E}_r(\vec{r}, t) = \vec{A}_r e^{i(\vec{k}_r \cdot \vec{r} - \omega' t)} \quad (\text{a}) \quad (\text{C.3})$$

$$\vec{E}_t(\vec{r}, t) = \vec{A}_t e^{i(\vec{k}'' \cdot \vec{r} - \omega'' t)} \quad (\text{b})$$

Here, the subscript r refers to reflected wave, and t refers to transmitted wave.

Any points at the interface $z = 0$; $(x, y, 0)$ satisfy equation (C.4), independent of time.

$$\vec{n} \times (\vec{E}_0 + \vec{E}_r) = \vec{n} \times \vec{E}_t \quad (\text{C.4})$$

Transferring equations (C.2) and (C.3) into (C.4), we get

$$\vec{n} \times (\vec{E}_0 e^{i(\vec{k} \cdot \vec{r} - \omega t)} + \vec{E}_r e^{i(\vec{k}' \cdot \vec{r} - \omega' t)}) = \vec{n} \times \vec{E}_t e^{i(\vec{k}'' \cdot \vec{r} - \omega'' t)} \quad (\text{C.5})$$

To simplify the use of subscripts for further axis components, primes for reflected waves, and double primes for transmitted waves are used. Because frequency is an intrinsic property of wave, it should not change as light propagates: $\omega = \omega' = \omega''$, which also indicates $k_x = k_x' = k_x''$, $k_y = k_y' = k_y''$.

Without loss of generality, the components of the wave vector in x - z plane are set equal to each other, hence $k \sin \theta = k' \sin \theta' = k'' \sin \theta''$.

$$k = k' = \frac{\omega}{v_1}, k'' = \frac{\omega}{v_2}.$$

It is therefore concluded that $\theta = \theta'$, $\frac{\sin \theta}{\sin \theta''} = \frac{v_1}{v_2} = \frac{\sqrt{\mu_2 \epsilon_2}}{\sqrt{\mu_1 \epsilon_1}} = \frac{n_2}{n_1}$, and these two equations are just the laws of reflection and refraction. Generally, $\mu \approx \mu_0$ unless we are dealing with a ferromagnetic material, hence $\frac{n_2}{n_1} = \frac{\sqrt{\epsilon_2}}{\sqrt{\epsilon_1}}$.

The polarization of a plane wave has two modes, *S* polarization and *P* polarization (they are also called *S* mode and *P* mode or *TE* polarization and *TM* polarization). *S* polarization means electric field *E* is perpendicular to incident plane, and its component parallel to the plane is zero. *P* polarization means the vector *E* is parallel to incident plane, and its component perpendicular to the plan is zero. Their geometric configurations are shown in Fig C.1. Furthermore, if the incident wave is in *S* mode, so are the reflected and transmitted waves. Similarly, if the incident wave is in *P* mode, so are the reflected and transmitted waves.

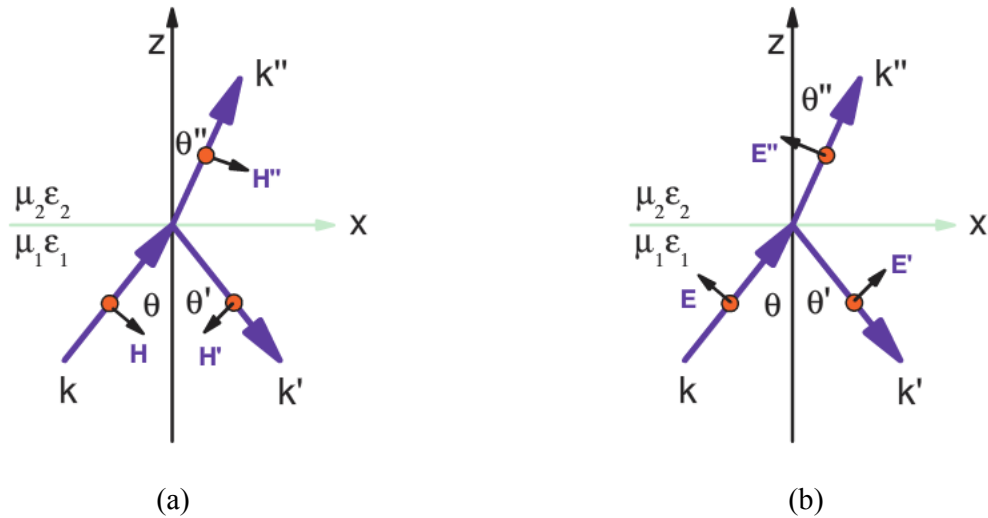


Fig C.1 Explanation of S mode and P mode (a) S mode, (b) P mode

C.1 S mode

As electric field E is parallel to $x = 0$ plan in S mode, $\vec{n} \times (\vec{E}_2 - \vec{E}_1) = 0, \vec{n} \times (\vec{H}_2 - \vec{H}_1) = 0$ in

(C.1) (c) can be rewritten as : $E + E' = E'', H \cos \theta - H' \cos \theta' = H'' \cos \theta''$.

From $H = \sqrt{\frac{\varepsilon}{\mu}} E$, and $\mu = \mu_0$, we can get $\sqrt{\varepsilon_1}(E - E') \cos \theta = \sqrt{\varepsilon_1} E'' \cos \theta''$.

Again, inserting $\frac{\sin \theta}{\sin \theta'} = \sqrt{\frac{\varepsilon_2}{\varepsilon_1}}$ into $\sqrt{\varepsilon_1}(E - E') \cos \theta = \sqrt{\varepsilon_1} E'' \cos \theta''$ and $E + E' = E''$, we

get, in conclusion:

$$\frac{E'}{E} = \frac{\sqrt{\varepsilon_1} \cos \theta - \sqrt{\varepsilon_2} \cos \theta''}{\sqrt{\varepsilon_1} \cos \theta + \sqrt{\varepsilon_2} \cos \theta''} = -\frac{\sin(\theta - \theta'')}{\sin(\theta + \theta'')} \quad (\text{C.6})$$

$$\frac{E''}{E} = \frac{2\sqrt{\varepsilon_1} \cos \theta}{\sqrt{\varepsilon_1} \cos \theta + \sqrt{\varepsilon_2} \cos \theta''} = \frac{2 \cos \theta \sin \theta''}{\sin(\theta + \theta'')}$$

C.2 P mode

As the electric field E is perpendicular to $x = 0$ plan in P mode,

$\vec{n} \times (\vec{E}_2 - \vec{E}_1) = 0, \vec{n} \times (\vec{H}_2 - \vec{H}_1) = 0$ in (C.1) (c) can be rewritten as:

$H + H' = H'', E \cos \theta - E' \cos \theta' = E'' \cos \theta''$.

From $H = \sqrt{\frac{\varepsilon}{\mu}} E$, and $\mu = \mu_0$, we can get $\sqrt{\varepsilon_1}(E + E') = \sqrt{\varepsilon_1} E''$.

Again, take $\frac{\sin \theta}{\sin \theta'} = \sqrt{\frac{\varepsilon_2}{\varepsilon_1}}$ into $\sqrt{\varepsilon_1}(E + E') = \sqrt{\varepsilon_1}E''$ and $\sqrt{\varepsilon_1}(E + E') = \sqrt{\varepsilon_1}E''$, in

conclusion:

$$\frac{E'}{E} = \frac{\tan(\theta - \theta'')}{\tan(\theta + \theta'')} \quad (\text{C.7})$$

$$\frac{E''}{E} = \frac{2 \cos \theta \sin \theta''}{\sin(\theta + \theta'') \cos(\theta - \theta'')}$$

Appendix D: Transfer Matrix Method Derivation

Similar to the derivation of Fresnel Equations in Appendix B, the transfer matrix method is also derived from Maxwell's Equations^[94]. Assume the plane of incidence to be the y - z plane, z being the direction of stratification. Let's take TE polarization as an example, where the electric fields in the y and z directions are all zero, and the magnetic field in the x direction is zero. So the Maxwell's vector equations reduce to six scalar equations, shown as follows:

$$\begin{aligned} \frac{\partial H_z}{\partial y} - \frac{\partial H_y}{\partial z} + \frac{i\varepsilon\omega}{c} E_x &= 0 \\ \frac{\partial H_x}{\partial z} - \frac{\partial H_z}{\partial x} &= 0 \\ \frac{\partial H_y}{\partial x} - \frac{\partial H_x}{\partial y} &= 0 \end{aligned} \quad (D.1)$$

$$\begin{aligned} \frac{i\omega\mu}{c} H_x &= 0 \\ \frac{\partial E_x}{\partial z} - \frac{i\omega\mu}{c} H_y &= 0 \\ \frac{\partial E_x}{\partial y} + \frac{i\omega\mu}{c} H_z &= 0 \end{aligned} \quad (D.2)$$

These equations show that H_y , H_z and E_x are only depend on y and z . Eliminating H_y , H_z by taking the x -component of the wave equation, it follows that

$$\frac{\partial^2 E_x}{\partial y^2} + \frac{\partial^2 E_x}{\partial z^2} + n^2 k_0^2 E_x = \frac{d(\ln \mu)}{dz} \frac{\partial E_x}{\partial z} \quad (D.3)$$

where,

$$n^2 = \varepsilon\mu, k_0 = \frac{\omega}{c} = \frac{2\pi}{\lambda_0} \quad (D.4)$$

To solve equation (D.3), a trial solution can be taken, which is a product of two functions, one involving y only and the other involving z only:

$$E_x(y, z) = Y(y)U(z). \quad (D.5)$$

Eq. (D.3) comes to be

$$\frac{1}{Y} \frac{d^2 Y}{dy^2} = -\frac{1}{U} \frac{d^2 U}{dz^2} - n^2 k_0^2 + \frac{d(\ln \mu)}{dz} \frac{1}{U} \frac{dU}{dz} \quad (\text{D.6})$$

Now the terms on the left only depend on y , whilst the terms on the right only depend on z . Hence (D.6) cannot hold unless both sides are equal to a constant (denoted as $-K^2$):

$$\frac{1}{Y} \frac{d^2 Y}{dy^2} = -K^2 \quad (\text{D.7})$$

$$\frac{d^2 U}{dz^2} + n^2 k_0^2 U - \frac{d(\ln \mu)}{dz} \frac{dU}{dz} = K^2 U \quad (\text{D.8})$$

For the sake of convenience, set

$$K^2 = k_0^2 \alpha^2 \quad (\text{D.9})$$

Then (D.7) contributes to $Y = [\text{const}] e^{ik_0 \alpha y}$, and consequently E_x is in the form of

$$E_x = U(z) e^{i(k_0 \alpha y - \omega t)} \quad (\text{D.10})$$

where, $U(z)$ is a (possibly complex) function of z . Equation (D.2) analogously indicates that H_y , and H_z are given by expressions of the same form:

$$H_y = V(z) e^{i(k_0 \alpha y - \omega t)} \quad (\text{D.11})$$

$$H_z = W(z) e^{i(k_0 \alpha y - \omega t)} \quad (\text{D.12})$$

According to equations (D.1) and (D.2), the amplitude functions, U , V and W are related to each other by the following three relations:

$$\begin{aligned}
V' &= ik_0(\alpha W + \varepsilon U) \\
U' &= ik_0\mu V \\
\alpha U + \mu W &= 0
\end{aligned} \tag{D.13}$$

The superscript prime symbol denotes differentiation with respect to z . Substituting W from $\alpha U + \mu W = 0$ into $V' = ik_0(\alpha W + \varepsilon U)$, and together with $U' = ik_0\mu V$, two simultaneous first-order differential equations for U and V can be found:

$$\left. \begin{aligned}
U' &= ik_0\mu V \\
V' &= ik_0\left(\varepsilon - \frac{\alpha^2}{\mu}\right)U
\end{aligned} \right\} \tag{D.14}$$

Taking derivation to z so as to reach two equations involving U and V separately, finally (D.4) gives the following second-order linear differential equations:

$$\frac{d^2U}{dz^2} - \frac{d(\ln \mu)}{dz} \frac{dU}{dz} + k_0^2(n^2 - \alpha^2)U = 0 \tag{D.15}$$

$$\frac{d^2V}{dz^2} - \frac{d\left[\ln\left(\varepsilon - \frac{\alpha^2}{\mu}\right)\right]}{dz} \frac{dV}{dz} + k_0^2(n^2 - \alpha^2)V = 0 \tag{D.16}$$

On account of the substitution rule, which is a consequence of the symmetry of Maxwell's Equations, it immediately follows that for the TM wave ($H_y = H_z = 0$), the non-vanishing components of the field vectors are of the form:

$$H_x = U(z)e^{i(k_0\alpha y - \omega t)} \tag{D.17}$$

$$E_y = -V(z)e^{i(k_0\alpha y - \omega t)} \tag{D.18}$$

$$E_z = -W(z)e^{i(k_0\alpha y - \omega t)} \tag{D.19}$$

where,

$$\left. \begin{aligned} U' &= ik_0 \mu W \\ V' &= ik_0 \left(\varepsilon - \frac{\alpha^2}{\mu} \right) U \end{aligned} \right\} \quad (\text{D.20})$$

and W is related to U by means of the equation

$$\alpha U + \mu W = 0 \quad (\text{D.21})$$

U and V now satisfy the second-order linear differential equations:

$$\frac{d^2 U}{dz^2} - \frac{d(\ln \varepsilon)}{dz} \frac{dU}{dz} + k_0^2 (n^2 - \alpha^2) U = 0 \quad (\text{D.22})$$

$$\frac{d^2 V}{dz^2} - \frac{d \left[\ln \left(\mu - \frac{\alpha^2}{\varepsilon} \right) \right]}{dz} \frac{dV}{dz} + k_0^2 (n^2 - \alpha^2) V = 0 \quad (\text{D.23})$$

Since the function $U(z)$ and $V(z)$ each satisfy a second-order linear differential equations (D.15) and (D.16), U and V can each be expressed as a linear combination of two particular solutions, say U_1, U_2 and V_1, V_2 . These particular solutions cannot be arbitrary; they may be coupled by the first-order differential equation.

$$\left. \begin{aligned} U_1' &= ik_0 \mu V_1 \\ V_1' &= ik_0 \left(\varepsilon - \frac{\alpha^2}{\mu} \right) U_1 \end{aligned} \right\} \quad (\text{D.24})$$

$$\left. \begin{aligned} U_2' &= ik_0 \mu V_2 \\ V_2' &= ik_0 \left(\varepsilon - \frac{\alpha^2}{\mu} \right) U_2 \end{aligned} \right\} \quad (\text{D.25})$$

From these relations it obeys that

$$V_1 U_2' - U_1' V_2 = 0, \quad U_1 V_2' - V_1' U_2 = 0$$

Hence,

$$\frac{d}{dz} (V_1 U_2 - U_1 V_2) = 0$$

which implies that determinant D is a constant, associated with any two arbitrary solution of (D.14), i.e. D is invariable of this system of equations.

$$D = \begin{vmatrix} U_1 & V_1 \\ U_2 & V_2 \end{vmatrix} \quad (\text{D.26})$$

For our purpose, the most convenient choice of the particular solution is

$$\left. \begin{aligned} U_1 &= f(z), & U_2 &= F(z) \\ V_1 &= g(z), & V_2 &= G(z) \end{aligned} \right\} \quad (\text{D.27})$$

Such that

$$f(0) = G(0) = 0 \quad \text{and} \quad g(0) = F(0) = 1 \quad (\text{D.28})$$

Then the solution with

$$U(0) = U_0, \quad V(0) = V_0 \quad (\text{D.29})$$

may be expressed in the form of $\left. \begin{aligned} U &= FU_0 + fV_0 \\ V &= GU_0 + gV_0 \end{aligned} \right\}$, or in matrix notation,

$$Q = NQ_0 \quad (\text{D.30})$$

$$\text{where, } Q = \begin{pmatrix} U(z) \\ V(z) \end{pmatrix}, Q_0 = \begin{pmatrix} U_0 \\ V_0 \end{pmatrix}, N = \begin{pmatrix} F(z) & f(z) \\ G(z) & g(z) \end{pmatrix} \quad (\text{D.31})$$

On account of the relation $D = \text{constant}$, the determinant of the square matrix N is a constant. The value of this constant may immediately be found by taking $z=0$, giving $|N| = Fg - fG = 1$.

It is usually more convenient to express U_0 and V_0 as functions of $U(z)$ and $V(z)$. Solving for U_0 and V_0 , we obtain,

$$Q_0 = MQ \quad (\text{D.32})$$

where,

$$M = \begin{pmatrix} g(z) & -f(z) \\ -G(z) & F(z) \end{pmatrix} \quad (\text{D.33})$$

$$\text{This matrix is also uni-modular, } |M| = 1 \quad (\text{D.34})$$

The significance of M is clear: it relates the x - and y -components of the electric (or magnetic) vectors in the plane $z=0$ to the components in an arbitrary plane $z = \text{constant}$. Now we saw that knowledge of U and V is sufficient for the complete specification of the field. Hence for the purposes of determining the propagation of a plane monochromatic wave through a stratified medium, the medium only need be specified by an appropriate two by two uni-modular matrix M . For this reason we shall call M the characteristic matrix of the stratified medium. The constancy of the determinant M may be shown to imply the conservation of energy.

We shall now consider the form of the characteristic matrix for cases of particular interest.

D.1 Light propagation in a homogeneous dielectric film

In this case ϵ, μ and $n = \sqrt{\epsilon\mu}$ are constants. If θ denotes the angle normal to the wave makes with the z -axis, we have by (D.24) $\alpha = n \sin \theta$.

For a TE wave, we have according to (D.15) and (D.16),

$$\left. \begin{aligned} \frac{d^2U}{dz^2} + (k_0^2 n^2 \cos^2 \theta)U &= 0 \\ \frac{d^2V}{dz^2} + (k_0^2 n^2 \cos^2 \theta)V &= 0 \end{aligned} \right\} \quad (\text{D.35})$$

The solutions of these equations, subject to the relations (D.14), are easily seen to be

$$\left. \begin{aligned} U(z) &= A \cos(k_0 n z \cos \theta) + B \sin(k_0 n z \cos \theta), \\ V(z) &= \frac{1}{i} \sqrt{\frac{\varepsilon}{\mu}} \cos[B \cos(k_0 n z \cos \theta) - A \sin(k_0 n z \cos \theta)]. \end{aligned} \right\} \quad (\text{D.36})$$

Hence the particular solutions (D.27) which satisfy the boundary conditions (D.28) are

$$\left. \begin{aligned} U_1 = f(z) &= \frac{i}{\cos \theta} \sqrt{\frac{\mu}{\varepsilon}} \sin(k_0 n z \cos \theta), \\ V_1 = g(z) &= \cos(k_0 n z \cos \theta), \\ U_2 = F(z) &= \cos(k_0 n z \cos \theta), \\ V_2 = G(z) &= \frac{i}{\cos \theta} \sqrt{\frac{\varepsilon}{\mu}} \cos \theta \sin(k_0 n z \cos \theta). \end{aligned} \right\} \quad (\text{D.37})$$

If we set

$$p = \sqrt{\frac{\varepsilon}{\mu}} \cos \theta \quad (\text{D.38})$$

The characteristic matrix can be simplified as

$$M = \begin{pmatrix} \cos(k_0 n z \cos \theta) & -\frac{i}{p} \sin(k_0 n z \cos \theta) \\ -ip \sin(k_0 n z \cos \theta) & \cos(k_0 n z \cos \theta) \end{pmatrix} \quad (\text{D.39})$$

For a *TM* wave, the same equations hold, with p replaced by

$$q = \sqrt{\frac{\mu}{\varepsilon}} \cos \theta \quad (\text{D.40})$$

D.2 The reflectivity and transmission coefficients from transfer matrix method

Let A , R , and T denote, as before, the amplitudes (possibly complex) of the electric vectors of the incident, reflected, and transmitted waves. Further, let ε_1, μ_1 and ε_l, μ_l be the dielectric constant and the magnetic permeability of the first and the last medium, and

let θ_i and θ_t be off-normal (direction of stratification) angles of the incident and transmitted waves.

The characteristic matrix for a pile of homogeneous films is expressed

$$M(z_N) = M_1(z_1)M_2(z_2 - z_1)\dots M_N(z_N - z_{N-1}) = \begin{pmatrix} m_{11} & m_{12} \\ m_{21} & m_{22} \end{pmatrix} \quad (\text{D.41})$$

The boundary conditions demand that the tangential components of E and H shall be continuous across each of the two boundaries of the stratified medium. This gives, if the

relation $\vec{H} = \sqrt{\frac{\epsilon}{\mu}} \vec{s} \times \vec{E}$ is also used, the following relations for a TE wave

$$\left. \begin{aligned} U_0 &= A + R, & U(z_1) &= T \\ V_0 &= p_1(A - R), & V(z_1) &= p_1 T \end{aligned} \right\} \quad (\text{D.42})$$

$$\text{where, } p_j = \sqrt{\frac{\epsilon_j}{\mu_j}} \cos \theta_j, \quad (\text{D.43})$$

The four quantities U_0 , V_0 , U , and V given by (D.42) are connected by the basic relation (D.32); hence

$$\left. \begin{aligned} A + R &= (m_{11} + m_{12} p_l) T, \\ p_1(A - R) &= (m_{21} + m_{22} p_l) T, \end{aligned} \right\} \quad (\text{D.44})$$

m_{ij} being the elements of the characteristic matrix of the medium, evaluated for $z = z_l$.

From (D.44) we obtain the reflection and transmission coefficients of the film:

$$r = \frac{R}{A} = \frac{(m_{11} + m_{12} p_l) p_l - (m_{21} + m_{22} p_l)}{(m_{11} + m_{12} p_l) p_l + (m_{21} + m_{22} p_l)} \quad (\text{D.45})$$

$$t = \frac{T}{A} = \frac{2p_1}{(m_{11} + m_{12}p_l)p_1 + (m_{21} + m_{22}p_l)} \quad (\text{D.46})$$

where, r and t are then the ratios of the amplitudes of the magnetic and not the electric vectors.

Appendix E: An Example of RCWA Application Structure

I am starting my analysis from the original RCWA formulation, explaining how it is related to reflectivity calculation.

We define the space in three regions, region 1 ($z < 0$), region 2 ($0 < z < d$), region 3 ($z > d$), with average relative permittivity $\epsilon_1, \epsilon_2, \epsilon_3$ respectively. It is assumed that each of the three regions has the permeability of free space. The diffraction of an obliquely incident plane wave is on a loss-less (relative permittivity is a real number) sinusoidal grating, with the incident wave polarized perpendicular to the plane of incidence (s mode). Hence the electric field has only y component. Divided region and angle notation are shown in Fig E.1.

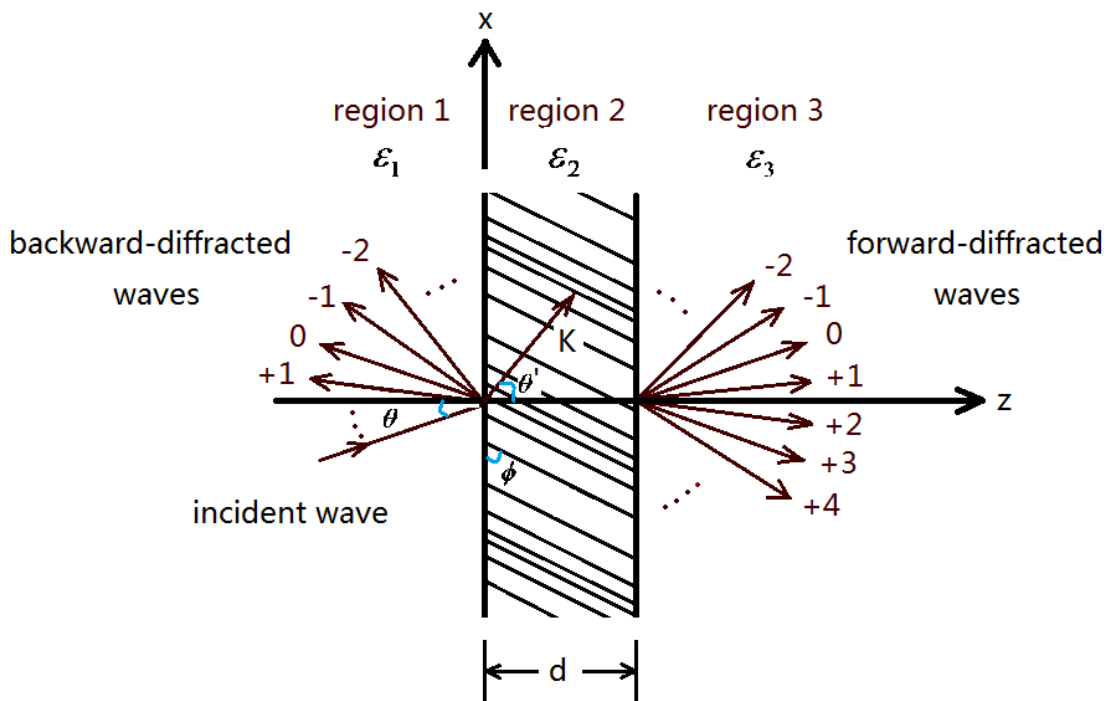


Fig E.1 Geometry for planar-grating diffraction

The relative permittivity in modulated region 2 ($0 < z < d$) is

$$\varepsilon(x, z) = \varepsilon_2 + \Delta\varepsilon \cos[K(x \sin \phi + z \cos \phi)] \quad (\text{E.1})$$

where, ε_2 is the average dielectric constant in region 2;

$\Delta\varepsilon$ is the amplitude of the sinusoidal relative permittivity;

$$K = \frac{2\pi}{\Lambda}, \quad \Lambda \text{ is the grating period;}$$

ϕ is the grating slant angle;

θ is the angle of incidence in region 1;

d is the thickness of region 2 along z axis.

The general approach for finding electromagnetic solution is figure out wave equation in each region and then matching electric and magnetic fields as well as their tangent at boundary ($z=0$, and $z=d$). The electric field in three regions (all oscillating in y direction) may be expressed as

$$E_1 = \exp[-i(\beta_0 x + \xi_{10} z)] + \sum_h R_h \exp[-i(\beta_h x - \xi_{1h} z)] \quad (\text{E.2})$$

$$E_2 = \sum_h S_h(z) \exp[-i(\beta_h x + \xi_{2h} z)] \quad (\text{E.3})$$

$$E_3 = \sum_h T_h \exp\{-i[\beta_h x + \xi_{3h}(z-d)]\} \quad (\text{E.4})$$

where, $\beta_h = k_1 \sin \theta - hK \sin \phi$ for any integer h (the wave index);

$$\xi_{lh}^2 = k_l^2 - \beta_h^2 \text{ for } l = 1, 3 \text{ (the region index);}$$

$$k_l = 2\pi\sqrt{\varepsilon}\lambda \text{ for } l = 1, 2, 3; \quad \lambda \text{ is the free space wavelength;}$$

$$i = \sqrt{-1};$$

R_h is the normalized amplitude of the h^{th} reflected wave;

T_h is the normalized amplitude of the h^{th} transmitted wave;

R_h and T_h are to be determined from the matching of the electric and magnetic fields.

Substituting (E.1) and (E.4) into the Helmholtz equation in the grating region,

$\nabla^2 E_2 + k_2 E_2 = 0$, results in an infinite set of coupled wave equations:

$$\frac{\Delta \varepsilon}{8 \varepsilon_2} \frac{d^2 S_h(u)}{du^2} = (\cos \theta' - hu \cos \phi) \frac{dS_h(u)}{du} - \rho h(h - B) S_h(u) + S_{h+1}(u) + S_{h-1}(u) \quad (\text{E.5})$$

where, $S_h(u) = S_h(z)$;

$$u = i \kappa z; \quad \kappa = \frac{\pi \Delta \varepsilon}{2 \lambda \sqrt{\varepsilon_2}};$$

$$\rho = \frac{2 \mu^2 \varepsilon_2}{\Delta \varepsilon};$$

$$B = \frac{2 \cos(\phi - \theta')}{\mu};$$

$$\mu = \frac{\lambda}{\Lambda \sqrt{\varepsilon_2}}.$$

If S and S' are defined as state variables, (E.5) can be written in matrix form[#] as

$$\begin{bmatrix} S'' \\ S''' \end{bmatrix} = [b_{rs}] \begin{bmatrix} S \\ S' \end{bmatrix} \quad (\text{E.6})$$

where, S , S' , and S'' are the column vectors of S_h , dS_h/du , and $d^2 S_h/du^2$ respectively. $[b]$

is the coefficient matrix determined from (E.5), whose dimension is fourth the size of S ,

because both column and row are twice the size of S .

Up to this point, this system of coupled-wave equations is derived without assumptions and approximations. If n waves are retained in the analysis for example, the boundary condition provides $4n$ linear equations, due to the continuity for electric field, the

[#] As is shown in the Appendix A: the state equation

continuity for magnetic field, the continuity for tangential electric field, and the continuity for tangential magnetic field.

Judging from linear algebra algorithms, the solution of (E.6) can be expressed in terms of the eigenvalues and eigenvectors of the coefficient matrix [b]. Assuming q_m is the m^{th} eigenvalue and w_{hm} is the m^{th} element of row, corresponding to the i^{th} eigenvalue, in matrix [w] composed of the eigenvectors, we have the relation:

$$S_h(u) = \sum_m^{2n} C_m w_{im} \exp(q_m u) \quad (E.7)$$

Matrix [b] in (E.6) is $2n \times 2n$ matrix, with $2n$ eigenvalues. Consequently, the specific solution is a linear combination of $2n$ general solutions, with $2n$ unknown coefficients C_m . Furthermore, R_h and T_h are other $2n$ unknown values to be determined. Therefore, the number of equations available, $4n$, is exactly equal to the number of unknowns, so that each R_h and T_h can be calculated.

The criteria for the number of orders to retain is determined by two requirements,

1) Energy conservation:

$$\sum_h (DE_{1h} + DE_{3h}) = 1, \quad DE_{1h} = \text{Re} \left(\frac{\xi_{1h}}{\xi_{10}} \right) R_h R_h^*, \quad DE_{3h} = \text{Re} \left(\frac{\xi_{3h}}{\xi_{10}} \right) T_h T_h^*,$$

2) convergence to the proper solution with an increasing number of field harmonics for all the grating and the incident-wave parameters.

DE_{1h} and DE_{3h} are the diffraction efficiencies in region 1 and 3 individually. The

quantity $\text{Re}\left(\frac{\xi_{lh}}{\xi_{l0}}\right) = \frac{\cos\theta_{lh}}{\cos\theta_{l0}}$, where θ_{lh} is the diffraction angle for the h^{th} order wave in l^{th} medium.

As ϕ approaches but does not equal zero^{*}, all the reflected wave vectors in region 1 approach an identical direction and $\theta_{lh} \rightarrow \theta_{l0}$, so the resulting reflected intensity of the composite wave is $\sum_h |R_h|^2$. Likewise, all the transmitted wave vectors in region 3 approach a single direction; and the resulting transmitted intensity of this composite waves is $\sum_h |T_h|^2$. So RCWA is later applied for calculating the reflection coefficient. In the case where $\phi \rightarrow 0$, and the amplitude of the sinusoidal relative permittivity $\Delta\varepsilon = 0$, it is reduced to single-layer problem.

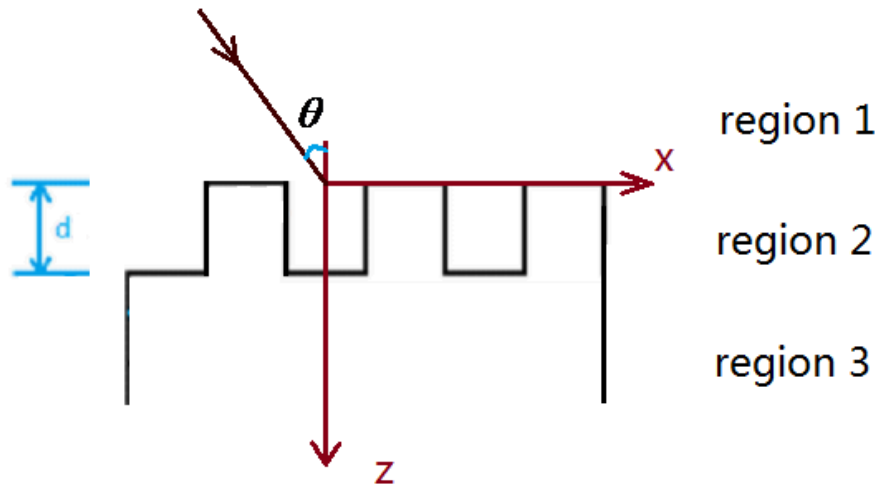


Fig E.2 Geometry for binary rectangular-groove grating

^{*} this is because the above analysis is derived from Floquet theorem, which is valid for infinite periodic structures. However when the slant angle is exactly zero (pure reflection grating), the modulation is no longer periodic since it has a finite number of cycles.

For further analysis, we can discover that $K = \frac{2\pi}{\Lambda}$ is the period in k -space, so the electric field as shown in (E.2)-(E.4) is expressed in Fourier series. From this idea, RCWA is applied to textured interface as in Fig E.2.

From discrete Fourier transform the relative permittivity can be expanded in the form of

$$\varepsilon(x) = \sum_p \varepsilon_p \exp\left(i \frac{2\pi p x}{\Lambda}\right) = \sum_p \varepsilon_p \exp(ipKx) \quad (\text{E.8})$$

Following the previous analysis about TE mode where incident light is in x - z plane with incident angle θ , the incident normalized electric field that is normal to the plane of incidence is given by

$$E_{inc,y} = \exp[-ik_0 n_1 (x \cdot \sin \theta + z \cdot \cos \theta)] \quad (\text{E.9})$$

$$E_{1,y} = E_{inc,y} + \sum_h R_h \exp[-i(k_{xh}x - k_{1,zh}z)] \quad (\text{E.10})$$

$$E_{3,y} = \sum_h T_h \exp\{-i[k_{xh}x + k_{3,zh}(z-d)]\} \quad (\text{E.11})$$

where, k_{xh} is determined from the Floquet condition, $k_{xh} = k_1 \sin \theta - hK$.

$$k_{l,zh} = \begin{cases} +k_0 \left[n_l^2 - (k_{xh}/k_0)^2 \right]^{1/2} & k_0 n_l > k_{xh} \\ -ik_0 \left[(k_{xh}/k_0)^2 - n_l^2 \right]^{1/2} & k_{xh} > k_0 n_l \end{cases} \quad l=1,3$$

In region 2, the electric field in y component and the magnetic field in x component may be expressed as a Fourier expansion in terms of space-harmonic fields,

$$E_{2,y} = \sum_h S_{yh}(z) \exp(-ik_{xh}x) \quad (\text{E.12})$$

$$H_{2,x} = -i \left(\frac{\varepsilon_0}{\mu_0} \right)^{1/2} \sum_h U_{xh}(z) \exp(-ik_{xh}x) \quad (\text{E.13})$$

Inserting (E.12) into Maxwell's Equation $\nabla \times E_2 = -i\omega\mu_0 H_2$, and (E.13) into Maxwell's Equation $\nabla \times H_2 = i\omega\varepsilon_0 \varepsilon(x) E_2$, we could obtain two differential equations,

$$\frac{\partial E_{2y}}{\partial z} = i\omega\mu_0 H_{2x} \quad (\text{E.14})$$

$$\frac{\partial H_{2x}}{\partial z} = i\omega\varepsilon_0 \varepsilon(x) E_{2y} + \frac{\partial H_{2z}}{\partial x} \quad (\text{E.15})$$

Substituting (E.12), (E.13), and (E.8) into (E.14) and (E.15), and eliminating H_{2z} , we could obtain the coupled-wave equations in each order h , expressed in terms of permittivity Fourier expansion.

$$\begin{aligned} \frac{\partial S_{yh}}{\partial z} &= k_0 H_{xh} \\ \frac{\partial U_{xh}}{\partial z} &= \left(\frac{k_{xh}^2}{k_0} \right) S_{yh} - k_0 \sum_p \varepsilon_{(h-p)} S_{yp} \end{aligned} \quad (\text{E.16})$$

Similar to the analysis for a planar grating, the solution process comes down to a $4n$ linear equations' problem. However, in this case, the relative permittivity in the form of Fourier transform is also in every order. So various textures, including shape, period, depth, resulting in various Fourier transforms on permittivity, will contribute to different solutions.

Note that if we take the second order derivative equation instead of two first order derivative equation, the matrix reduces from $2n*2n$ to $n*n$, which takes 1/8 of the previous overall computational time of eigenvalue problem.

Appendix F: Recipe of Textured Surface

F.1 Sputter deposition

Sputter deposition is a physical vapor deposition (PVD) which is deposits thin films on substrates by sputtering source materials. The process schematic is shown in Fig F.1 ejecting source material is ejected from sputtering target, and only a small fraction of ionized atoms is deposited on substrates, because little amount among the wide energy distributing ions could release from the target ballistically in straight lines and attach on the substrates energetically. The sputtering gas is usually an inert gas, like argon. Closer weight of sputtering gas to target atomic weight could increase momentum transfer efficiency; hence light target materials prefer neon or argon gas, and heavy target materials prefer krypton or xenon gas. There are a few parameters to control the film compound, like target doping levels, substrate temperatures, background gas pressure, *etc.* Al doped ZnO can be fabricated on Si thin film solar cell to improve light trapping and short circuit current density^[95,96], which behaves as both ARC and transparent conducting oxide (TCO).

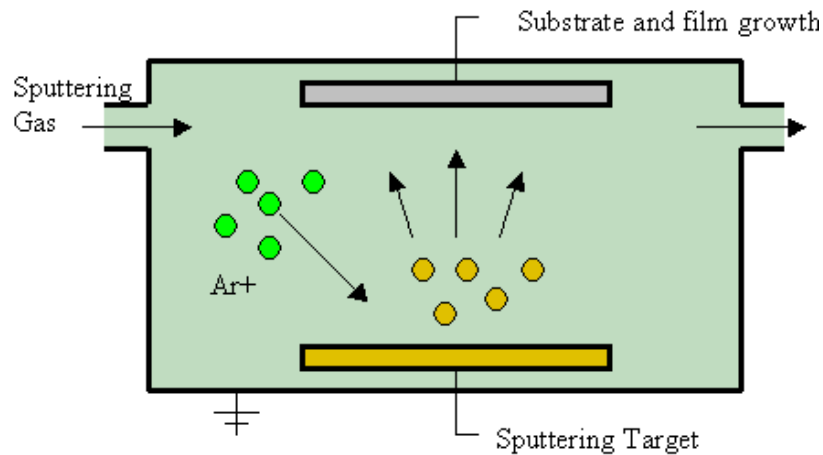


Fig F.1 Schematic of sputtering deposition technique

F.2 Si KOH wet etching

- To prepare a fresh 200ml KOH solution, weigh 70g KOH pellets into a plastic beaker, and add 190ml DI water. Mix on warm surface until KOH has dissolved. Add 40ml of isopropyl alcohol to the solution.
- Start with silicon (100) polished wafers. Clean wafers and pattern with photoresist. Use reactive ion etching (RIE) system to etch the exposed oxide or nitride surface. For oxides, the recommended chemistry is CHF₃, and O₂ (or CF₄ and O₂). Etch until the silicon is exposed (shiny); typically 5 minutes per 100 nm film. Rinse the wafer with acetone to remove the remaining photoresist, rinse with DI water, and blow dry air on the sample.
- Put KOH solution in glass container and warm to 80 °C on a hot plate. Place patterned wafer (with patterned hard mask) in the KOH solution. The KOH will bubble at the exposed silicon sites while etching occurs. The etch rate for 30% KOH at 80 °C should be about 1 micron/min.

Appendix G: Solar Cell Patterning

G.1 Back etching

Due to samples loaded in MBE chamber are not always perfectly round, indium is used as temperature uniform glue to mount the irregular shape samples like half or quarter wafer. And for those whole wafers, pin stages are used to hold samples. So there are two different ways to deal with samples depending on how they were mounted. During the growth of thin film solar cell, the samples are surrounded by gun materials although in high vacuum environment, so the back side could also be deposited on the non-indium mounted samples (the indium mounted samples' back sides are protected by indium).

Indium mounted samples

Use razor blade scrape of the large In chunks as much as possible (usually till the part below In turns to be rough and black)

Dip into concentrated HCl (38%, 12.4 mol/L) until no bubbles come out (in fact it will take a long time to get rid of any bubbles, so generally, when the speed and amount of bubbles is so little to realize, this step is done).

Non indium mounted samples

Evenly spread resin on a glass slide sitting on a 110-130 °C hot plate, and place the sample face down in the resin. To get good contact with resin without big gaps nor bubbles, let the sample touch the resin on one side first, then let it fall down on the other side. And to avoid etchant eating the front side, make sure the edge is fully surround by resin. Dip the cooled glass holding sample into cold $\text{H}_3\text{PO}_4:\text{H}_2\text{O}_2:\text{H}_2\text{O}$ (volume rate

3:2:20) solution for 2 minute to remove deposited materials on the back, where the H_3PO_4 and H_2O_2 are of concentration 85% and 30% individually. Rinse the sample with DI water and blow dry with nitrogen gas to prevent further etching.

It should be noticed that the temperature of hot plate should not extend 200 °C, or the front side might show foggy and un-uniform, because of destroyed lattice structure. Etchant acts on n type GaAs substrate also, but due to 500 *um* thickness, substrate can survive.

G.2 Degreasing

For the samples attached on a glass slide by resin, first place them into boiling tetrachlorethylene to detach samples, large amount of organic remains left on surfaces. Further degreasing process should follow the steps of boiling tetrachlorethylene, cold acetone and boiling methanol 2 min respectively, which should be done three runs, so 9 beakers are needed, and finally rinse DI water for 3 min and blow nitrogen gas, where we should pay attention that both acetone and DI water are cold, so it is better to wobble the sample for full clean. Meanwhile, it is better to shrink the pouring levels of the nine beakers along the processing order, as shown in Fig G.1, so that the impurity on the sample holder can be minimized to again appear in the further degreasing solution. (Due to harmful solutions, make sure the fume hood is pulled down to the safety position.)

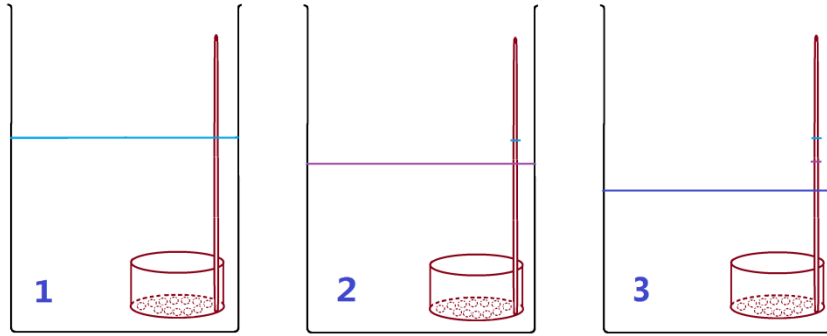


Fig G.1 Pouring level for beakers in degreasing process

Front contact patterning by photolithography

After cleanness, the next step is fabricate the front contact patterning, which could effectively collect either electron or holes flow transferred to the front surface, but won't contribute to much shadow loss. The semiconductors' resistivity is much larger than that of Au electrode, so transmission distance within semiconductors need to be as short as possible. It requires the Au electrode to be patterned instead of a point contact on the semiconductor surface, which could gather the current flowing on the semiconductor surface to the electrode. However, only the bare semiconductor can generate e-h pairs from the incoming light, so the bare area also should be as large as possible, to reduce shadow loss.

There are two kinds of photoresist, positive and negative, which will be removed and remained respectively for the area exposed under UV light after developing. Because the main ingredient in positive photoresist is long chain organic chemical, and will turn into short chain after UV exposure, which can be easily removed by developer. However, negative photoresist is the opposite, which is originally short chain organic chemical, and will build into long chain after UV exposure, so the area not exposed under UV light can

be easily removed during developing.

To form a mask of Au deposition, first cover a uniform negative photoresist (NR2-3000P) by a spinner. The most significant point for good uniformity is to avoid bubbles before spinning (If unfortunately there were, use dropper to suck them out). Set the program 3000rpm for 20 sec and 5000rpm for 25 sec. Compared with the cover created by 6000rpm for 40 sec, the fringes resulting from equal thickness interference are much closer to the edge. And the edge is always of bad quality consider not uniform. With uniform photoresist, the second step is pre-bake (or called soft bake) on hot plate at 110 °C for 60 sec. The third step following soft bake is 90 sec UV exposure by Mask Aligner (MJB3) who supplies three degrees of freedom to manipulate -- left/right, forward/backward, clockwise/anticlockwise. Before letting the sample touch the mask, adjust sample's location to make the number of solar cell as many as possible. Again there are two ways to ensure the mask is just touching the sample but not over pressed -- first, from microscope, the pattern on mask and its shadow closing up and finally registration, second, on the corner of substrate, fringe just showing up. If any one of the condition achieved, whoever comes first, adjustment is done. After UV exposure, the fourth step is post-bake (or so called hard bake) in oven 110 °C for 60 sec. The fifth step is developing samples in developer (RD6) for 25 sec to remove unexposed part, and rinsing DI water, blow-drying by nitrogen gas. Till now, the processing is nearly done except 1 min bake on 110°C hot plate before gold deposition.

There are several note should be paid attention during processing.

- The spinner is accelerating little by little, so for the first a few seconds, the speed can

not reach 3000rpm. At the same time, speeding up by several step can intensely increase uniformity.

- Because the oven opening will cool down the inside atmosphere around 5-10°C, temperature not precisely controlled, hot plate is a better option for bake.
- The photoresist is very sticky, and easy to cling to the mask. In case the sample fall into the gap of Mask Aligner, first control the left/right controller to enlarge the gap to the maximum, and then carefully pick up the sample with tweezer. Do not use torch to illuminate, since it is another exposure.
- For aging photoresist whose water has evaporated, the developing time should be abated, or the photoresist would be over eaten resulting in too much undercut. After developing, the sample can be exposed to usual light.

Gold Evaporation

Because of good conductivity and matching fermi level, gold deposition is used to fabricate the front and back contact as electrodes. When the samples are exposed to ambient, they are easily formed a oxide layer, with high resistivity and play a significant role in series resistance. Consequently, it is necessary to remove those oxide layer before gold deposition.

Dip samples into concentrated HCl solution around 15 sec to remove oxide layer with bad conductivity (photoresist will not react with HCl). The water should no longer 'wet' the surface.

Gold evaporation process is based on thermal evaporation, requiring vacuum environment, 10^{-7} mbar, to elongate the Au atoms' diffusion length. The pumping order is let the mechanical pump run first (all valves closed), and then open the rough valve to let it pump the chamber. Close the rough valve between mechanical pump and chamber, and let the diffusion pump run, which needs the mechanical pump to take out the exhauster. So the high vacuum valve between chamber and pump is closed, and pumps are working for the air within themselves. Slowly open the high vacuum valve to let diffusion pump work for the chamber.

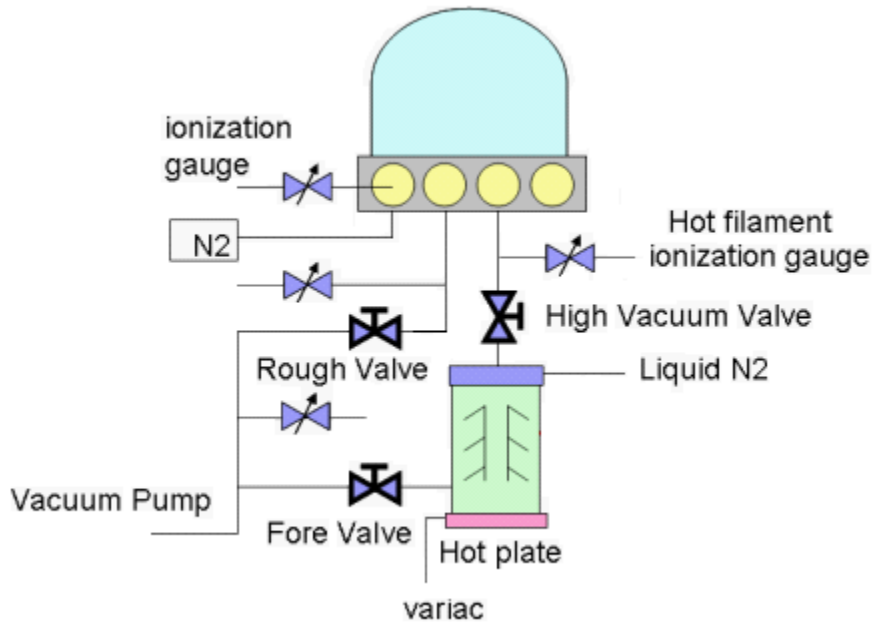


Fig G.2 Schematic diagram of evaporation system

Wait till the pressure in the chamber reduce to stable low value 10^{-7} mbar, heat up the Au in vacuum environment with shutter closed the Au boat, until any impurity evaporate and pumped out. With pure and stable Au vapor, shutter can be open, and Au will deposit on samples. Front contact and back contact are based on the same physics. But back contact do not need to be patterned, just planar gold film for fully contact.

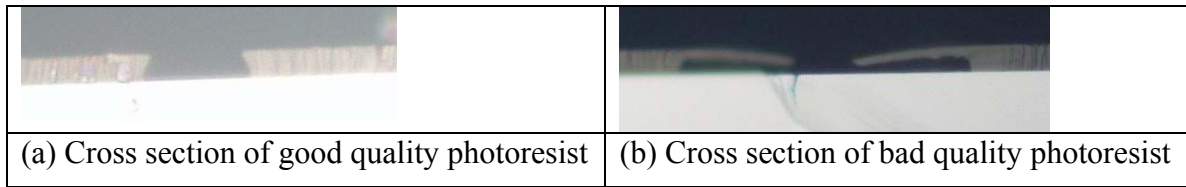


Fig G.3 Cross section of photoresist after patterning

Front contact. As the gold deposits layer by layer, it will stay on both bare substrate and photoresist covering region. But the gold will be not deposited as thick as photoresist; the two regions are not collaborating, so the Au on photoresist can be easily removed with photoresist during lift off process. Where it requires the cross section of photoresist in the shape shown in Fig G.3. The angle of undercut is determined by the baking time, temperature, as well as developing time, and the good structure for easy lift off is between 45°-60°. During the evaporation, stage for samples will turn hot, as high as 100°C, and this temperature cannot be controlled in our system. Photoresist is sensitive to high temperature, and would degrade above 180 °C, resulting in hard lift off and contamination to chamber. Hence, it is better to do the lift off after front contact deposition and follow by back contact.

There are several note need attention:

➤ NEVER have the roughing valve and the fore valve open at the same time. This can cause diffusion pump oil to be sucked into the mechanical pump. Also do not have the roughing valve and the high vacuum valve open at the same time this can cause mechanical pump oil to be drawn up into the chamber and diffusion pump. The stand by mode for the evaporator when not being used is with the fore valve open and all other valves closed. Also the diffusion pump, the mechanical pump, and the gauge controller is

on, but everything else is off.

➤ The chamber should always in vacuum condition even when it is not in use, to prevent impurity or oxygen harming the system. So before loading or taking out samples, nitrogen gas should be filled first, controlled by a vent valve. (We use nitrogen gas instead of air, because air would also bring dense amount of water vapor, hard to get rid when stay in chamber.) When opening the vent valve, make sure that high vacuum valve and roughing pump are closed, and that the fore valve is open. So nitrogen will not flow into the diffusion and mechanical pumps, but just fill the chamber. (The ion gauge detecting the pressure of chamber should be turned off, or the pressure would exceed the measure range.) At this point it is OK to open the main vent valve, and do not let the the inline gauge over zero or the bell jar would pump up.

➤ For deposition opening, the liquid nitrogen trap should be filled at least half an hour before open the chamber to air, because the diffusion pump needs to be cooled thoroughly form the LN2 trap before opening any valves to prevent oil from back stream into the system.

➤ In both case of before loading samples and after taking out samples, the chamber and its belt need to be cleaned carefully by acetone dipped clean room wipe, or the chamber would show up opaque.

➤ The net Au boat, Au, and boat with Au after deposition need to be weighted for knowing how much gold has been used for this thickness, good reference for next run.

Gold Electroplating

Thicken the gold contact could reduce resistance, as the larger thickness contribute to large flux area. So it is more significant when the solar cell is placed under concentrator, with large current flow inside the contact. As explained in Au deposition part, the amount of gold can be placed in Au boat is very limited, so for thick contact, several times deposition is required. And every time, we need to open the chamber, add some gold, let the mechanical pump and diffusion pump pump the system from the atmosphere to vacuum, do Au degas to confirm stable uniform Au vapor, and deposit. This process required too much time, power and labor. To speed up this process, electroplating can be used as a short cut. With thin and good contact deposition Au, playing a role as good electrode for further electroplating. Because larger area of Au will be preferred as electrode, and back contact's area is 9 times of front contact, the electroplating process should be done after front contact, before back contact deposition. And for good conductivity inside the semiconductor, the window layer should be opened after electroplating instead of before it.

The theory of electroplating, as shown in Fig G.4 is that solar cells supply electrons (negative electrode) and let positive Au ions experience oxidation reduction reaction, the Au atoms staying on the previous Au patterning.

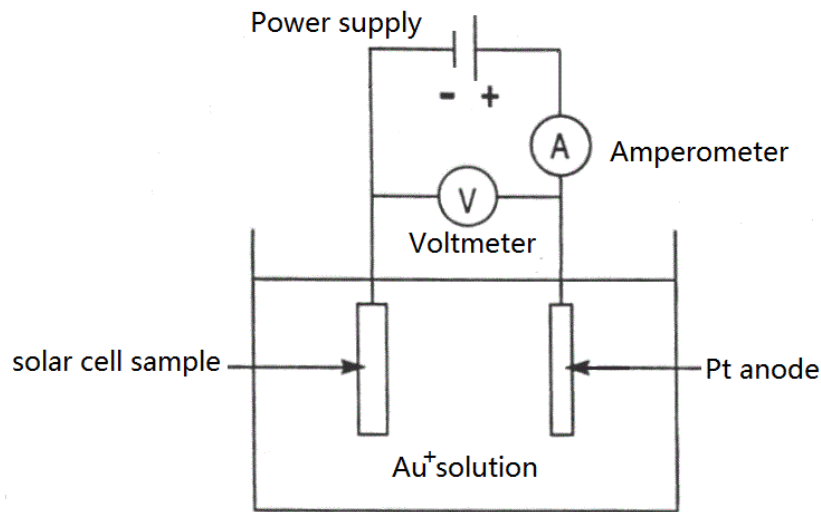


Fig G.4 The theory of electroplating

G.3 Contact layer etching

This process is also called as window layer opening. Because Au can not contact well with $\text{Al}_{0.8}\text{Ga}_{0.2}\text{As}$ window layer, easy to peel off, around 300 nm GaAs film is deposited above window layer to achieve good contact. But this GaAs layer would degrade current extracting, so it should only stay under Au electrode and play a role as part of electrode. Consequently, selective etching solution, citric acid: H_2O_2 =4:1 (volume ratio) is used to remove GaAs layer beyond Au contact area. Due to etchant do not act on $\text{Al}_{0.8}\text{Ga}_{0.2}\text{As}$ window layer, the etching time is not precisely controlled, generally 1 and half minute (GaAs etching rate is close to 200 nm per minute).

G.4 Mesa Etching

Mesa etching can be avoided, if all the solar cells are of good uniform quality and the deposited Au on the edges is cut, so in this case, the whole sample with several cells' pattern is performing as a big single cell. However, that ideal case won't always happen.

Although the Au deposited on the edges can be cut to avoid short circuit, the non-uniform growth, partial Au lift off on the front contact, and mistakes taken during measurement will all influence the sample. So if one cell died, it will affect the whole sample's analysis. For more cells can be tested, the cells need to be separated, either cutting cells one by one, or using etching the space between cells. Because the size of working area before etching is $5 \times 3 \text{ mm}$, there is a high risk of damage to the samples during cutting, thus mesa etching is preferred. Mesa etching uses the same etchant as back etching to remove the materials between cells. Cold $\text{H}_3\text{PO}_4:\text{H}_2\text{O}_2:\text{H}_2\text{O}$ (volume ratio 3:2:20) can etch GaAs, so it could isolate the substrate into single cells, $3 \times 2 \text{ mm}$.

Quite similar to front contact patterning, an etching mask is required to protect further working area. So another shape of mask is needed for photolithography, so that after liftoff, photoresist can protect individual solar cells. The final devices would be separated as shown in Fig G. 5. During alignment, the critical point is to let the cross between cells on the mask align with the Au cross at exactly the same position.

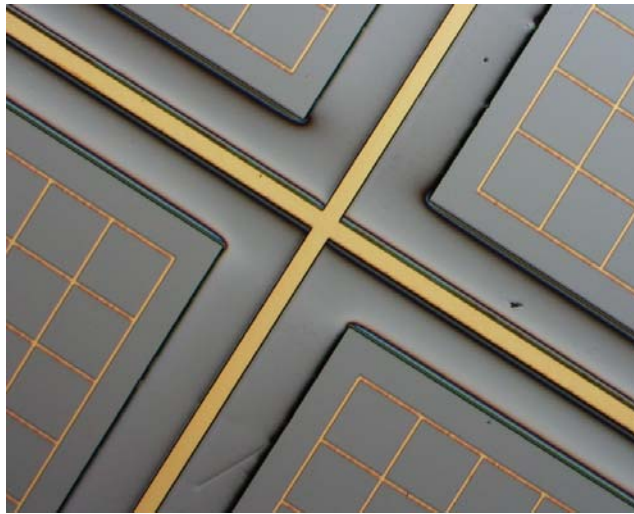


Fig G.5 The view of samples after mesa etching

Reference

- [1] R.Y.Zhang, B. Shao, J. R. Dong, K. Huang, Y. M. Zhao, S. z. Yu, and H. Yang, 'Broadband quasi-omnidirectional antireflection AlGaInP window for III-V multi-junction solar cell through thermal dewetted au nano template', *Opt. Mat. Exp*, Vol. 2(2), pp.173-182, (2012).
- [2] Li-Ko Yeh, Kun-Yu Lai, Guan-Jhong Lin, Po-Han Fu, Hung-Chih Chang, Chin-An lin, Jr-Hau He, 'Giant efficiency enhancement of GaAs solar cells with graded antireflection layers based on syringe-like ZnO nanorod arrays', *Advanced Energy Materials* Vol.1(4), pp.506-510, (2011).
- [3] William Shockley and Hans J. Queisser, 'Detailed Balance Limit of Efficiency of p-n function Solar Cells', *Journal of Applied Physics*, Vol. 32(3), pp.510-519, (1961).
- [4] Charles E. Backus, 'Solar Cells', Institute of Electrical & Electronics Engineers (IEEE), ISBN13: 978-0879420697, 512p, (1976).
- [5] J. E. Parrott, 'Choice of an equivalent black body solar temperature', *Solar Energy*, Vol.51 (3), pp.195 – 195, (1993).
- [6] Rybicki, G.B. and Lightman, A.P., 'Radiative Processes in Astrophysics', John Wiley & Sons, pp. 22, ISBN10: 0-471-82759-2, 382p., (1979).
- [7] <http://pveducation.org/pvcdrom/appendicies/standard-solar-spectra>
- [8] http://en.wikipedia.org/wiki/Black-body_radiation#cite_ref-12
- [9] T. Trupke, M. A. Green and P. Würfel, *J. Appl. Phys.*, Vol.92(7), pp.4117-4122, (2002).
- [10] P. Würfel, 'The chemical potential of radiation', *J. Phys. C, Solid State Phys.*, Vol.15, pp.3967-3986, (1982).
- [11] Martin A. Green, Keith Emery, Yoshihiro Hishikawa, Wilhelm Warta and Ewan D. Dunlop, 'Solar cell efficiency tables (version 40)', *prog. Photovolt: Res. Appl.* Vol.20, pp.606-614, (2012).
- [12] E. Rosencher, 'Optoelectronics', equation (7.25), (2002).
- [13] Jaques I. Pankove, 'Optical Processes in Semiconductors', Courier Dover Publications, 422p., (1971).
- [14] Alan L. Fahrenbruch and Richard H. Bube, 'Fundamentals of Solar Cells', Academic Press, 559p., (1983).
- [15] A. Mehrotra, A. Freundlich, and A. Alemu, "Optimized device design for radiation resistant and high dislocation solar cells for space", *Photovoltaic Specialist Conference (PVSC)*, 35th IEEE, pp. 2574-2577, (2010).
- [16] E. F. Schubert, 'Light-Emitting Diodes', Cambridge Univ. Press, (2006).

-
- [17] R. R. King, D. C. Law, K. M. Edmondson, C. M. Fetzer, G. S. Kinsey, H. Yoon, R. A. Sherif, and N. H. Karam, '40% efficient metamorphic GaInP/GaInAs/Ge multi-junction solar cells', *Applied Physics Letter*, Vol.90(18), pp.183516-183516-3, (2007).
- [18] Tatsuya Takamoto, Takaaki Agui *et al.*, 'World's highest efficiency triple-junction solar cells fabricated by inverted layers transfer process', *Potovoltaic Specialists Conference (PVSC)*, 35th IEEE, pp.412-417, (2010).
- [19] Steven Wojtczuk, Philip Chiu, Xuebing Zhang, Daniel Derkacs, Chris Harris, Daryl Pulver, and Mike Timmons, 'InGaP/GaAs/InGaAs 41% Concentrator Cells Using Bi-facial Epigrowth', *Potovoltaic Specialists Conference (PVSC)*, 35th IEEE, pp.1259-1264, (2010).
- [20] D. Bouhafs *et al.* 'Design and simulation of antireflection coating systems for optoelectronic devices: Application to silicon solar cells', *Solar Energy Mater. Solar Cells*, Vol.52(1-2), pp.79-93, (1998).
- [21] H. C. Barshilia *et al.* 'TiAlN/TiAlON/Si₃N₄ tandem absorber for high temperature solar selective applications', *Appl. Phys. Lett.*, Vol.89(19), pp.191909-191911, (2006).
- [22] H. C. Lee *et al.* 'Discussion on electrical characteristics of i-In_{0.13}Ga_{0.87}N p-i-n photovoltaics by using a single/multi-antireflection layer', *Solar Energy Mater. Solar Cells*, Vol.94(7), pp.1259-1262, (2010).
- [23] B. Sopori. 'Dielectric films for si solar cell applications', *J. Electron Mater.* Vol.34(5), pp.564-570, (2005).
- [24] H. Taguchi, T. Soga and T. Jimbo. 'Fabrication of GaAs/Si tandem solar cell by epitaxial lift-off technique', *Japanese Journal of Applied Physics Part 2-Letters* Vol.42(12A), pp. L1419-L1421, (2003).
- [25] T. Yamada *et al.* '5 x 5 cm² GaAs and GaInAs solar cells with high conversion efficiency', *Japanese Journal of Applied Physics Part 2-Letters & Express Letters*, Vol.44(28-32), pp. L985-L987, (2005).
- [26] A. Alemu *et al.* 'Low temperature deposited boron nitride thin films for a robust antireflection coating of solar cells', *Solar Energy Mater. Solar Cells*, Vol.94, pp.921-923, (2010).
- [27] A. W. Bett *et al.* 'Advanced III-V solar cell structures grown by MOVPE', *Solar Energy Mater. Solar Cells*, Vol.66(1-4), pp.541-550, (2001).
- [28] D. J. Aiken. 'Antireflection coating design for series interconnected multi-junction solar cells', *Progress in Photovoltaics* Vol.8(6), pp.563-570, (2000).
- [29] J. Krepelka, 'Maximally flat antireflection coatings', *Jemna Mechanika A Optika*, pp.53-56, (1992).

-
- [30] Christopher E. Valdivia, Eric Desfonds, Denis Masson, Simon Fafard, Andrew Carlson, John Cook, Trevor J. Hall, Karin Hinzer, 'Optimization of antireflection coating design for multi-junction solar cells and concentrator systems', Photonics North 2008, Proc. of SPIE, Vol.7099, pp.709915, (2008).
- [31] <http://www.almazoptics.com/MgF2.htm>
- [32] Streetman, Ben G.; Sanjay Banerjee, 'Solid State Electronic Devices (5th ed.)', Prentice Hall, ISBN:0-13-025538-6, 524 p., (2000).
- [33] Junguang Tao, Tim Luttrell and Matthias Batzill, 'A two-dimensional phase of TiO₂ with a reduced bandgap', Nature Chemistry, Vol.3, pp.293-300 (2011)
- [34] Taurian, O.E., Springborg, M., Christensen, N.E. 'Self-consistent electronic structures of MgO and SrO', Solid State Communications, Vol.55(4), pp.351-355, (1985).
- [35] M. Houssa, 'High-k Dielectrics', ISBN 0750309067, Appendix (p. 597).
- [36] J. Sikula, J. Pavelka, V. Sedlakova and J. Hlavka, 'Tantalum Capacitor as a Metal-Insulator-Semiconductor Structure'
http://www.kyocera.co.jp/prdct/electro/pdf/technical/cap_mis00.pdf
- [37] J. Ozdanova, H. Ticha, L. Tichy, 'Optical band gap and Raman spectra in some (Bi₂O₃)_x(WO₃)_y(TeO₂)_{100-x-y} and (PbO)_x(WO₃)_y(TeO₂)_{100-x-y}', Journal of Nan-Crystalline Solids, Vol.355(45-47), pp.2318-2322, (2009).
- [38] S. Debnath, M. R. Islam and M. S. R. Khan, 'Optical properties of CeO₂ thin films', Bull. Mater. Sci., Vol.30(4), pp.315-319, (2007).
- [39] M. F. Schubert *et al.* 'Design of multilayer antireflection coatings made from cosputtered and low-refractive-index materials by genetic algorithm', Optics Express, Vol.16(8), pp. 5290-5298, (2008).
- [40] D. J. Aiken, 'High performance antireflection coatings for broadband multi-junction solar cells', Solar Energy Mater. Solar Cells, Vol.64(4), pp. 393-404, (2000).
- [41] R. B. Pettit, C. J. Brinker and C. S. Ashley, 'Sol-gel double-layer antireflection coatings for silicon solar cells', Solar Cells, Vol.15, pp.267-278, (1985).
- [42] Edward D. Palik, 'Handbook of Optical Constants of Solids', Academic, San Diego, 995p., (1998).
- [43] E.D. Palik, 'Handbook of Optical Constants of Solids II', Academic, San Diego, 1069p.,(1998).
- [44] Toshiya Yoshida, Keiji Nishimoto, Keiichi Sekine, and Kazuyuki Etoh, 'Fluorid antireflection coatings for deep ultraviolet optics deposited by ion-beam sputtering', Appl. Opt., Vol.45(7), pp.1375-1379, (2006).
- [45] T.D. Radjabov, I.E. Djamaletdinova, A.V. Sharudo, H. Hamidova, 'Ion-beam-assisted deposition as a method for production of effective optical coatings', Surf. Coat. Technol, Vol.72(1-2), pp.99-102, (1995).

-
- [46] Hua Yu, Hongji Qi, Yun Cui, Yanming Shen, JianDa. Shao, ZhengXiu Fan, 'Influence of substrate temperature on properties of MgF₂ coatings', *Appl. Surf. Sci.* Vol.253(14), pp.6113-6117 ,(2007).
- [47] S. Strehlke, S. Bastide, J. Guillet, C. Levy-Clement, 'Design of porous silicon antireflection coatings for silicon solar cells', *Mater. Sci. Eng. B*, Vol.69, pp.81-86, (2000).
- [48] Y.P. Venkata Subbaiah, P. Prathap, K.T. Ramakrishna Reddy, 'Structural, electrical and optical properties of ZnS films deposited by close-spaced evaporation', *Appl. Surf. Sci.* 253 pp.2409-2415, (2006)
- [49] Sung-Mok Jung, Yong-Hwan Kim, Seong-Il Kim, Sang-Im Yoo, 'Design and fabrication of multi-layer antireflection coating for III-V solar cell', *Current Applied Physics* Vol.11, pp.538-541, (2011).
- [50] R.Y.Zhang, B. Shao, J. R. Dong, K. Huang, Y. M. Zhao, S. z. Yu, and H. Yang, 'Broadband quasi-omnidirectional antireflection AlGaInP window for III-V multi-junction solar cell through thermal dewetted au nano template', *Opt. Mat. Exp*, Vol. 2(2), pp 173-182, (2012).
- [51] Li-Ko Yeh, Kun-Yu Lai, Guan-Jhong Lin, Po-Han Fu, Hung-Chih Chang, Chin-An lin, Jr-Hau He, 'Giant efficiency enhancement of GaAs solar cells with graded antireflection layers based on syringe-like ZnO nanorod arrays', *Advanced Energy Materials*, Vol.1(4), pp.506-510, (2011).
- [52] Kui-Qing Peng, Shuit-Tong Lee, 'Silicon nanowires for photovoltaic solar energy conversion', *Adv. Mater.* , Vol.23(2), pp.198-215, (2010).
- [53] Sung Jin An, Jee Hae Chae, Gyu-Chui Yi, and Gil H. Park, 'Enhanced light output of GaN-based light-emitting diodes with ZnO nanorod arrays', *Appl. Phys. Lett.* Vol.92, pp.121108-121110, (2008).
- [54] J. K. Kim, S. Chhajed, M. F. Schubert, E. F. Schubert, A. J. Fischer, M. H. Crawford, J.Cho, H. Kim, C. Sone, 'Light-extraction enhancement of GaInN light-emitting diodes by graded-refractive-index indium tin oxide anti-reflection contact', *Adv. Mater.*, Vol.20(4), pp.801-804, (2008).
- [55] X. Zhu, L. Wang and D. Yang, 'Investigations of random pyramid texture on the surface of single-crystalline silicon for solar cells', *Proceedings of ISES Solar World Congress*, pp.1126-1130, (2007).
- [56] Ting-Gang Chen, Bo-Yu Huang, Yang-Yue Huang, En-Chen Chen, Peichen Yu, and Hsin-Fei Meng, 'Fabrication and device modeling of micro-textured conductive polymer / silicon heterojunction solar cells', *Photovoltaic Specialists Conference (PVSC)*, 38th IEEE, pp.3143-3145 (2012).
- [57] J. M. Gee, R. Gordon and H. F. Laing, 'Optimization of textured-dielectric coatings for crystalline-silicon solar cells', *Photovoltaic Specialists Conference*, 25th IEEE, pp.733-736, (1996).

-
- [58] E. S. Marstein *et al.* ‘Acidic texturing of multicrystalline silicon wafers’, Photovoltaic Specialists Conference (PVSC), 31st IEEE, pp.1309-1312, (2005).
- [59] <http://coefs.uncc.edu/jahudak/files/2011/08/AnisotropicSiEtch.pdf>
- [60] Bernhard C. G. ‘Structural and functional adaptation in a visual system’, *Endeavour* Vol.26, pp.79-84, (1967).
- [61] D. G. Stavenga, S. Foletti, G. Palasantzas, and K. Arikawa, ‘Light on the moth-eye corneal nipple array of butterflies’, *Proc. R. Soc. B*, Vol.273, pp.661-667, (2006).
- [62] C.H. Chiu, Peichen Yu, H. C. Kuo, C. C. Chen, T. C. Lu, S. C. Wang, S. H. Hsu, Y. J. Cheng, and Y. C. Chang, ‘Broadband and omnidirectional antireflection employing disordered BaN nanopillars’, *Optics Express*, Vol.16(12), pp.8748-8754, (2008).
- [63] Arvinder M Chadha, Weidong Zhou, Eric D Cline, ‘Design criteria for nanostructured omni-directional antireflection coatings’, Photovoltaic Specialist Conference (PVSC), 38th IEEE, paper NO.738, (2012).
- [64] Wang Yanshuo, Chen Nuofu, Zhang Xingwang, Yang Xiaoli, Bai Yiming, Cui Min, Wang Yu, Chen Xiaofeng, and Huang Tianmao, 'Ag surface plasmon enhanced double-layer antireflection coatings for GaAs solar cells', *Journals of Semiconductors*, Vol.30 (7), pp.072005-5(2009).
- [65] Chih-Hung Sun, Peng jiang, Bin Jiang, ‘Broadband moth-eye antireflection coatings on silicon’, *Appl. Phys. Lett.*, Vol.92, pp.061112-061114, (2008).
- [66] T. K. Gaylord, M.G. Moharam, Eric B. Grann, and Drew A. Pommet, ‘Formulation for stable and efficient implementation of the rigorous coupled-wave analysis of binary gratings’, *J. Opt. Soc. Am. A* Vol.12(5), pp.1068-1076, (1995).
- [67] D. G Stavenga, S Foletti, G Palasantzas, K Arikawa ‘Light on the moth-eye corneal nipple array of butterflies’, *Proc. R. Soc. B*, Vol.273, pp.661-667, (2006).
- [68] M.G. Moharam and T.K.Gaylord, ‘Coupled-wave analysis of reflection gratings’, *Applied Optics*, Vol. 20(2), pp.240-244, (1981).
- [69] M.G. Moharam and T.K.Gaylord, ‘Rigorous coupled-wave analysis of planar-grating diffraction’, *J.Opt. Soc. Am*, Vol. 71(7), pp.811-818, (1981).
- [70] H. Kogelnik, ‘Coupled wave theory for thick hologram gratings’, *Bell Sys. Tech. J.*, Vol.48(9), pp.2909-2947, (1969).
- [71] R. Agmusson and T.K. Gaylord, ‘Analysis of multiwave diffraction of thick gratings’, *J. Opt. Soc. Am*, Vol.67(9), pp.1165-1170, (1977).
- [72] R. Petit, ‘Electromagnetic Theory of Gratings’. Springer-Verlag, (1980).
- [73] H. Haidner, P.Kipfer, W. Stork, and N. Streibl, 'Zero-order gratings used as an artificial distributed index medium', *Optik*, Vol.89, pp.107-112, (1992).
- [74] M. W. Farn, 'Binary gratings with increased efficiency,' *Appl.Opt.*, Vol.21, pp.4453-4458, (1992).

-
- [75]] E. Nojonen, A. Vasara, J. Turunen, J. M. Miller, and M. R. Taghizadeh, 'Synthetic diffractive optics in the resonance domain,' *J. Opt. Soc. Am. A*, Vol.9, pp.1206-1213, (1992).
- [76] Chih-Hung Sun, Peng Jiang, Bin Jiang, 'Broadband moth-eye antireflection coatings on silicon', *Appl. Phys. Lett.*, Vol.92, pp.061112-061114, (2008).
- [77] Sung-Mok Jung, Young-Hwan Kim, Sang-Im Yoo, 'Design and fabrication of multi-layer antireflection coating for III-V solar cell', *Current Applied Physics II*, pp.538-541, (2011).
- [78] Steven Wojtczuk, Philip Chiu, Xuebing Zhang, Daniel Derkacs, Chris Harris, Daryl Pulver, and Mike Timmons, 'InGaP/GaAs/InGaAs 41% Concentrator cells using bifacial epigrowth', *Photovoltaic Specialist Conference (PVSC), 35th IEEE*, pp.1259-1264, (2010).
- [79] Wang Yanshuo, Chen Nuofu, Zhang Xingwang, Yang Xiaoli, Bai Yiming, Cui Min, Wang Yu, Chen Xiaofeng, and Huang Tianmao, 'Ag surface plasmon enhanced double-layer antireflection coatings for GaAs solar cells', *Journals of Semiconductors*, Vol.30 (7), pp17-21, (2009).
- [80] Chia-Hua Chang, Peichen Yu, Min-Hsiang Hsu, *et al.*, 'Combined micro- and nano-scale surface textures for enhanced near-infrared light harvesting in silicon photovoltaics', *Nanotechnology*, Vol.22, pp.095201-095204, (2011).
- [81] Silke L. Diedenhofen, Gabriele Vecchi, Rienk E. Algra, Alex Hartsuiker, *et al.*, 'Broad-band and Omnidirectional Antireflection Coatings Based on Semiconductor', *Adv. Mater.*, Vol.21, pp.973-978, (2009).
- [82] Yi-Fan Huang, *et al.*, 'Improved broadband and quasi-omnidirectional antireflection properties with biomimetic silicon nanostructures', *Nature Nanotechnology*, Vol.2(12), pp.770-774, (2007).
- [83] Yung-Jr Hung, San-Liang Lee, Kai-Chung Wu, Yian Tai, and Yen-Ting Pan, 'Antireflective silicon surface with vertical-aligned silicon nanowires realized by simple wet chemical etching processes', *Opt. Express*, Vol.19(18), pp.15792-15802 (2011).
- [84] Yi-Fan Huang, Surojit Chattopadhyay, Yi-jun Jen, Cheng-Yu Peng, Tze-An Liu, Yu-Kuei Hsu, Ci-Ling Pan, Hung-Chun Lo, Chih-Hsun Hsy, Yuan-Huei Chang, Chih-Shan Lee, Kuei-Hsien Chen, Li-Chyong Chen, 'Improved broadband and quasi-omnidirectional anti-reflection properties with biomimetic silicon nanostructures', *Nature Nanotechnology*, Vol.2(12), pp.770-774, (2007).
- [85] Yung-Jr Hung, San-Liang Lee, Kai-Chung Wu, Yian Tai, and Yen-Ting Pan, 'Antireflective silicon surface with vertical-aligned silicon nanowires realized by simple wet chemical etching processes', *Opt. Express*, Vol.19(18), pp.15792-15802 (2011).

-
- [86] Weidong Zhou, Meng Tao, Li Chen, and Hongjun Yang, 'Microstructured surface design for omnidirectional antireflection coatings on solar cells', *Journal of Applied Physics*, Vol.102(10), pp.103105-103113, (2007).
- [87] <http://refractiveindex.info/> , last access date 03/02/2012
- [88] M.G.Moharam, Eric B.Gtann, Drew A.Pommet, 'Formulation for stable and efficient implementation of the rigorous coupled-wave analysis of binary gratings', *J.Opt.Soc.Am*, Vol.12(5), pp.1068-1076, (1995).
- [89] Weidong Zhou, Meng Tao, Li Chen, Hongjun Yang, 'Microstructured surface design for omnidirectional antireflection coatings on solar cells', *Journal of Applied Physics*, Vol.102(10), pp.103105-103105-9, (2007).
- [90] W.Wang, A. Mehrotra, A. Alemu, A. Freundlich, 'Minimizing solar cell reflection loss through surface texturing and implementation of 1D and 2D subwavelength dielectric gratings', *Proc. of SPIE*, paper NO.8256, (2012).
- [91] Dustin A. Richmond, Qifeng Zhang, Guozhong Cao, Dirk N. Weiss, 'Pressureless nanoimprinting of anatase TiO₂ porous films', *J. Vac. Sci. Technol. B*, Vol.29(2), pp.21603-21603-5, (2011).
- [92] Jérémy Barbé, Andrew Francis Thomson, Er-Chien Wang, Keith McIntosh, Kylie Catchpole, 'Nanoimprinted TiO₂ sol-gel passivation diffraction gratings for solar cell applications', *Prog. Photovolt: Res.* Vol.20, pp.143-148, (2012).
- [93] Akhil Mehrotra, Alex Freundlich, 'Superior radiation and dislocation tolerance of IMM space solar cells', *Proc. Photovoltaics Specialist Conference*, 38th IEEE, pp.3150-3154, (2012).
- [94] Max Born, Emil Wolf, 'Principles of Optics', Cambridge University Press, ISBN 0-521-642221, 952p., (1999).
- [95] Michael Berginski, Jürgen Hupkes, Jürgen Hupkes, Melanie Schulte, Gunnar Schöpe, Helmut Stiebig, Bernd Rech, Matthias Wuttig, 'The effect of front ZnO:Al surface texture and optical transparency on efficient light trapping in silicon thin-film solar cells', *J of Appl. Phys*, Vol.101(7), pp.074903-074913, (2007).
- [96] Kannan ramanathan, Miguel A. Contreras, Craig L. Perkins, Sally Asher, Falah S. Hasoon, James Keane, David Young, Manuel Romero, Wyatt Metzger, Rommel Noufi, James Ward, Anna Duda, 'Properties of 19.2% efficiency ZnO/CdS/CuInGaSe₂ thin-film solar cell', *Progress in Photovoltaics: Research and Applications* Vol.11(4), pp.225-230, (2003).